Inorganic metal halide perovskite nanocrystals and thin films

Document status and date:
Published: 23/05/2023

Document Version:
Publisher's PDF, also known as Version of Record (includes final page, issue and volume numbers)

Please check the document version of this publication:

• A submitted manuscript is the version of the article upon submission and before peer-review. There can be important differences between the submitted version and the official published version of record. People interested in the research are advised to contact the author for the final version of the publication, or visit the DOI to the publisher's website.
• The final author version and the galley proof are versions of the publication after peer review.
• The final published version features the final layout of the paper including the volume, issue and page numbers.

[Link to publication](#)

Inorganic metal halide perovskite nanocrystals
and thin films:

photophysics, photovoltaics, and environmental impact

PROEFSCHRIFT

ter verkrijging van de graad van doctor aan de Technische Universiteit
Eindhoven, op gezag van de rector magnificus prof.dr. S. Lenaerts, voor
een commissie aangewezen door het College voor Promoties, in het
openbaar te verdedigen op dinsdag 23 mei 2023 om 11:00 uur

door

Olivera Vuković

geboren te Aranđelovac, Servië

Dit proefschrift is goedgekeurd door de promotoren en de samenstelling van de promotiecommissie is als volgt:

voorzitter: prof.dr.ir. E.J.M. Hensen

1e promotor: prof.dr.ir. R.A.J. Janssen

2e promotor: prof.dr. L. Billon (Université de Pau et des Pays de l'Adour)

leden: prof.dr. F.C. Grozema (Technische Universiteit Delft)

prof.dr. G.H. Gelinck

dr. S.C.J. Meskers

adviseur: dr. Y. Galagan (NXP Semiconductors)

dr. A. Petrozza (Istituto Italiano di Tecnologia)

Het onderzoek dat in dit proefschrift wordt beschreven is uitgevoerd in overeenstemming met de TU/e Gedragscode Wetenschapsbeoefening.

Inorganic metal halide perovskite nanocrystals and thin films:
photophysics, photovoltaics, and environmental impact

Table of contents

1

Introduction

"Electric power is everywhere present in unlimited quantities and can drive the world's machinery without the need of coal, oil, gas, or any other of the common fuels."

Nikola Tesla

1.1. Renewable energy

With the growth of the world population our energy demand is increasing. In addition, not only are non-renewable energy resources such as coal, oil, natural gas, and nuclear energy depleting but also these conventional energy technologies pose a threat to the environment. Therefore, switching to renewable energy sources such as solar, wind, geothermal, hydro, tidal, and biomass energy in the near future is necessary. The International Energy Agency reported that in 2021 the renewable power capacity addition broke a record by adding 295 GW of power produced by renewable sources compared to the previous year. Although the impact of renewable energy sources becomes more pronounced every year, almost 60% of the global energy production still originates from coal and gas (**Figure 1.1.**). The global energy crisis in 2022 also underlines the benefits of domestically generated renewable energy, fastening the renewable capacity expansion in the upcoming years.

The Sun is the primary source of energy for almost all ecosystems on Earth. People have been using solar energy for thousands of years but have only been able to convert it into electricity during the past 70 years. The potential of converting solar energy into useful energy seems limitless, because the energy that reaches the Earth's surface from the Sun is roughly 10^4 times higher than the global energy demand. However, the contribution of solar energy to global energy production is moderate, exceeding the 1% level in 2015 and reaching a share of 3.68% in 2021 (**Figure 1.1.a**). The worldwide share in the accumulative solar energy generation in 2021 is presented in **Figure 1.1.b**. The USA, China, and Japan are taking the lead with more than 25 TWh of annual change in solar energy generation, followed by Australia, Spain, India, and Brazil, which changes between 10 and 25 TWh annually.

A solar cell, or photovoltaic (PV) device, converts solar light into electricity *via* the photovoltaic effect. Because it does not require additional fuel, PV technology can have an exceptionally low environmental impact compared to conventional energy sources. The potential of PV technology is extremely alluring, but there are limitations to be overcome on the way to using solar energy as the main source of energy production. The trickiest are the technical ability to convert it into usable energy in an efficient and cost-effective way with minimal environmental impact, and the fact that sunlight strongly varies strongly with daytime, weather conditions, and seasons, creating the need to be able to temporarily store the converted solar energy for later use.

The main figure of merit for converting sunlight into electricity is the power conversion efficiency (PCE), or simply efficiency. In the detailed balance limit, the maximum PCE of a solar cell with a single *p–n* diode junction in terrestrial sunlight is 33.7% for an absorber with a bandgap of 1.4 eV[1]. For wider bandgaps, the PCE reduces because less photons can be absorbed, while for narrower

bandgaps increasingly more photon energy is lost *via* thermalization of charges. The practical PCE limits are only slightly lower than the theoretical detailed balance limit. In 1954, the first *p−n* junction silicon solar cell was developed at Bell Laboratories by Pearson, Chapin, and Fuller, giving a PCE of 6%[2]. By now, the record PCE is 26.8% for silicon heterojunction solar cells. The current photovoltaic market is dominated by crystalline silicon solar cells that provide PCEs of over 20%.
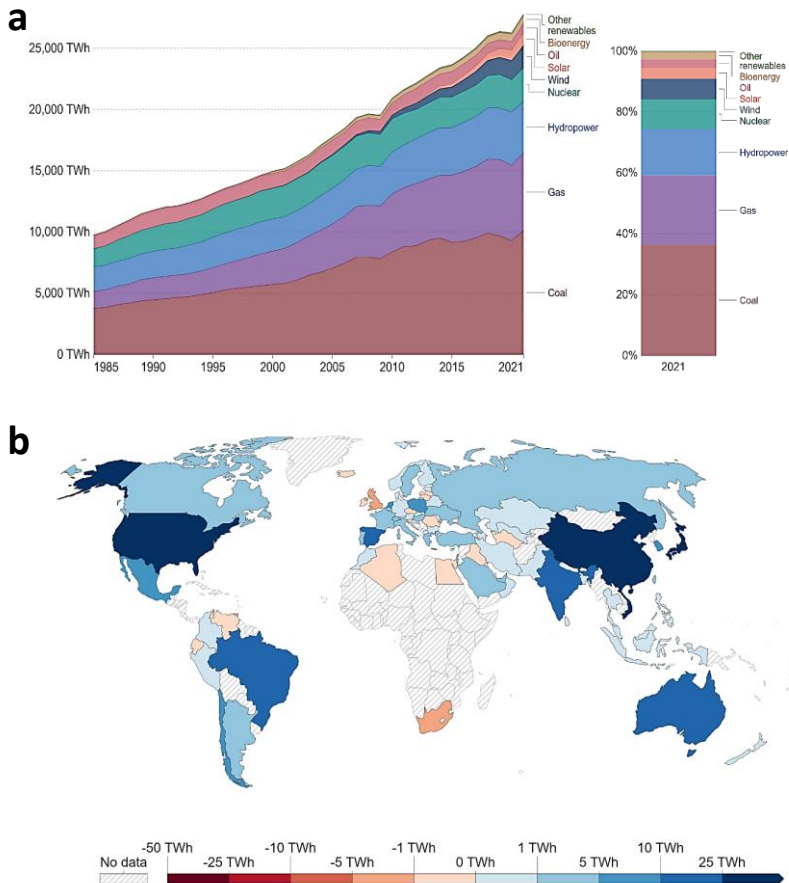
Figure 1.1. Electricity production in the world. a) Electricity production in the world, represented by sources, for the period between 1985 and 2021, with a special focus on the year 2021; 'Other renewables' includes wave, tidal, waste, and geothermal. **b)** Annual change in solar energy generation in 2021, relative to the previous year (Source: Our World in Data based on BP Statistical Review of World Energy (2022); Ember's Global and European Electricity Reviews (2022)[3])

Even though the PCE improved considerably over the last 70 years, single-junction silicon solar cells are unlikely to surpass a practical PCE limit of

slightly below 29%[4]. To surpass that limit, different absorber layers can be combined in a multi-junction device in which the incident solar light is spectrally distributed over different sub-cells to reduce transmission and thermalization losses. The detailed balance limit for a tandem cell is ~42% and can increase to ~68% when combining an infinite number of junctions. Multi-junction solar cells still have to meet the cost-efficiency balance but are considered as the future of the photovoltaic industry.

The photovoltaic industry is expected to have a key role in the electricity market in the long term. The conversion of solar energy into electrical energy has strong potential to reduce prices and our dependence on fossil fuels. High power conversion efficiency, low costs of materials and production, simple and eco-friendly manufacturing and circularity are the main requirements for solar cells. A prime candidate in such a search are perovskite solar cells.

1.2. Metal halide perovskite semiconductors

Perovskite is a term used for a class of compounds with the generic formula ABX_3 and a crystallographic structure similar to that of calcium titanate ($CaTiO_3$). The schematic representation of the cubic perovskite structure is shown in **Figure 1.2**. While many perovskites are oxide-based ($X = O^{2-}$), perovskites used for photovoltaic purposes are halide-based ($X = Cl^-$, Br^-, or I^-). In metal halide perovskites, A is a monocation for which methylammonium (MA^+), formamidinium (FA^+), or cesium (Cs^+) are most used, while B is a dication for which Pb^{2+} or Sn^{2+} are often employed. By using different combinations or mixtures of dissimilar A^+, B^{2+}, and X^- ions, the optical and electronic properties of perovskites can be tuned over a wide range and fitted to specific applications. There are, however, geometrical requirements that must be met to form a perovskite crystal structure. These can be expressed by two dimensionless parameters: Goldschmidt's tolerance factor[5] t and the octahedral factor[6] μ. Both factors depend on the ionic radii of the cations and anion (R_A, R_B, R_X) and can be expressed as $t = (R_A + R_X)/[\sqrt{2}(R_B + R_X)]$ and $\mu = R_B/R_X$. To form a stable perovskite crystal structure, t should be between $0.81 - 1.1$ and μ between $0.44 - 0.9$[7].
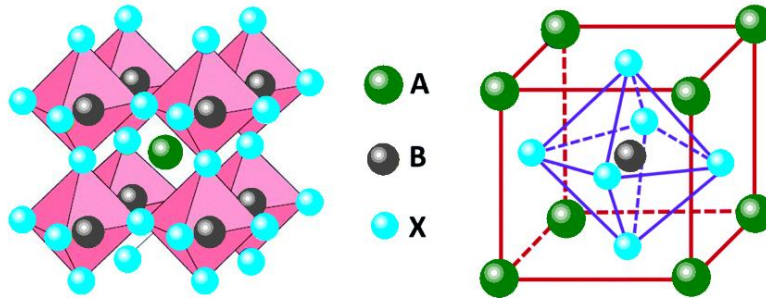
Figure 1.2. The structure of perovskite and its cubic unit cell with ABX$_3$ general formula.

In 2009, metal halide perovskites were first used as a sensitizer in dye-sensitized solar cells[8] and in 2012 for the first time as active layer in a thin-film device[9]. Since then, the research interest in metal halide perovskite has increased exponentially, motivated by the excellent structural and electronic properties of these materials, such as high defect tolerance, high absorption coefficient, long electron and hole diffusion lengths, low exciton binding energy, and low recombination rates[10,11]. Metal halide perovskites are easily processed as thin films. On a small scale this can be achieved *via* spin coating of precursors or colloidal solutions. On a large scale, methods for deposition are blade-coating[12,13], doctor-blade coating[14,15], slot-die coating[16,17], spray-deposition[18,19], roll-to-roll[20,21] coating, and inkjet printing[22,23]. Metal halide perovskites are an attractive material for the PV industry because they combine good efficiency, simple fabrication, and low costs with the possibility of up-scaling to an industrial level. Within only a few years after the first perovskite solar cells were reported, impressive PCEs have been achieved, with a record PCE of 25.8% (certified 25.5%) for perovskite single-junction cells[24].

Regardless of the success and research interest in metal halide perovskite semiconductor materials, perovskite solar cells −till now− face challenges with respect to long-term stability. Perovskite semiconductors are sensitive to environmental factors such as water and oxygen, but also to heat and light, i.e., factors that cannot be excluded by encapsulation and that are present under the working conditions[25]. The instability is related to the limited resilience of the perovskite lattice against loss and movement of ions. Solutions to these problems may be found by substituting MA$^+$ by FA$^+$ or Cs$^+$, or combinations thereof, which gives the material a higher resistance to thermal degradation and ion migration[26].

The easy tunability of the bandgap from roughly 1.2 to 3.0 eV[27,28] is one of the most attractive properties of metal halide perovskites. In contrast to conventional semiconductors in which bandgaps are formed between

5

antibonding and bonding orbitals, the bandgap in metal halide perovskites is formed between two antibonding orbitals[29]. The conduction band consists of antibonding orbitals formed by hybridization of the Pb 6p orbitals and the valence p orbitals of the halide. The valence band involves antibonding orbitals created from of the Pb 6s and the same halide p orbitals. The major contribution to the valence band maximum (VBM) comes from the halide valence p orbitals. Hence, by replacing the halide the valence band shifts in energy, but corresponding changes to the conduction band are small. This specific electronic structure is the main reason for successful tunability of the perovskite absorption spectra from the near infrared to the ultraviolet. This property puts metal halide perovskites in the leading position for multi-junction solar cells, where they can be used either with other materials, such as crystalline silicon[30], or alone in all-perovskite multi-junction solar cells[31].

1.3. Single-junction perovskite solar cells

Perovskite solar cells are mainly fabricated in two different device architectures, mesoporous or planar, and less commonly in a back-contact configuration. The different layouts are shown in **Figure 1.3**. In the mesoporous and planar configurations, the intrinsic perovskite photoactive layer is sandwiched between a p–type hole transport layer (HTL) and an n–type electron transport layer (ETL). Due to the high dielectric constant and the ambipolar nature of the perovskite photoactive layer, photogenerated charges separate in the film. The thickness and carrier diffusion length in the perovskite layer are the main factors for the choice of a certain architecture[32]. When the diffusion length is less than the perovskite layer thickness, a mesoporous blocking layer (e.g., mesoporous titanium dioxide (m-TiO$_2$)) can be introduced to prevent carrier recombination before they reach the charge selective layer (**Figure 1.3.c**). When the diffusion length is longer than the perovskite layer thickness, there is no need for a mesoporous blocking layer and a planar structure can be used.

Depending on the ordering of the charge transport layers deposition, two planar architectures are distinguished. When the incident light first goes through the ETL, the configuration is called normal or n–i–p (**Figure 1.3.a**)*.* Otherwise, it is called inverted or p–i–n planar (**Figure 1.3.b**)*.* Both configurations have advantages and disadvantages in performance and manufacturing, but the inverted structure offers the advantage of low-temperature processing and lower hysteresis[33].

Laboratory scale perovskite solar cells are usually manufactured by layer-by-layer deposition. On top of the glass substrate a transparent bottom electrode is deposited. The bottom electrode has to be transparent and highly conductive, to

limit resistive losses. The most common transparent electrode materials are indium tin oxide (ITO) and fluorine doped tin oxide (FTO).

Charge transport layers are preferably highly selective towards extracting either holes or electrons and combine this with high charge mobility and low parasitic absorption to minimize optical losses. Common ETLs are tin oxide (SnO_2) and titanium dioxide (TiO_2) for *n–i–p* and phenyl-C_{61}-butyric acid methyl ester (PCBM) and buckminsterfullerene (C_{60}) in *p–i–n* cell stacks. Often used HTLs are: 2,2′,7,7′-tetrakis(*N,N*-di(4-methoxyphenyl)amino)-9,9′-spirobifluorene (Spiro-OMeTAD) in *n–i–p* and poly[bis(4-phenyl)(2,4,6-trimethylphenyl)amine] (PTAA), poly(3,4-ethylenedioxythiophene) polystyrene sulfonate (PEDOT:PSS), nickel oxide (NiO_x), or self-assembled monolayers (SAMs) such as [2-(9*H*-carbazol-9-yl)ethyl]phosphonic acid (2PACz) in *p–i–n* configurations.

It is a common strategy to passivate the interface between the perovskite layer and the charge selective layers. Bulk and interface passivation reduce traps and defect states in the perovskite, and at the interfaces, mitigate the effects of a rough surface. Furthermore, it can align the energy levels of the charge transport layers with the valence or conduction bands of the perovskite.

In most common cell architectures, the stacks are finalized with an opaque and reflecting metal top electrode, usually formed *via* thermal evaporation. Top electrodes should be highly conductive to limit resistive losses. For this purpose, top contacts are often made of metals such as gold (Au), silver (Ag), aluminum (Al), or copper (Cu), but also non-metallic electrodes such as carbon are used. For semi-transparent cells, a sputtered ITO layer can be employed.

Because of its favorable energy level (work function) and its stability and hydrophobicity, carbon is an interesting material to be used as a top electrode, replacing the need for expensive metals (**Figure 1.3.d**). Since carbon extracts holes efficiently, it can be used to replace the HTL and/or metal electrode[34]. Carbon can be used in mesoporous and planar cell architectures. To prevent short-circuiting *via* a direct electrical contact between the mesoporous TiO_2 ETL and the carbon electrode, a thin interlayer of mesoporous zirconium dioxide (m-ZrO_2) is introduced. The layers can be screen printed and annealed at elevated temperature (450 °C) after which the perovskite is introduced by infiltration through the mesoporous stack. In planar device structure, carbon can be bladed on top of the perovskite, followed by low temperature annealing (100 °C)[35]. Perovskite HTL-free carbon-based solar cells show great potential because of their low cost production and superior stability in air[36].

Optical losses reduce light absorption in the perovskite layer and thereby limit the photocurrent and PCE. The light that is reflected from the front surface or absorbed by other layers than the perovskite does not contribute to charge generation. Optical losses can be reduced by using surface texturing and anti-

7

reflection layers, but they are inevitable in the conventional sandwiched structures where light propagates through a transparent substrate, a transparent electrode, and a charge transport layer. Back-contacted cell structures (**Figure 1.3.e**) are favorable for reducing these optical losses since they eliminate parasitic absorption and shading by the front contacts[37]. In a back-contact cell structure, both the anode and cathode are positioned on the same side of the perovskite layer. This reduces the risk of damaging perovskite since it is the last layer to be deposited.
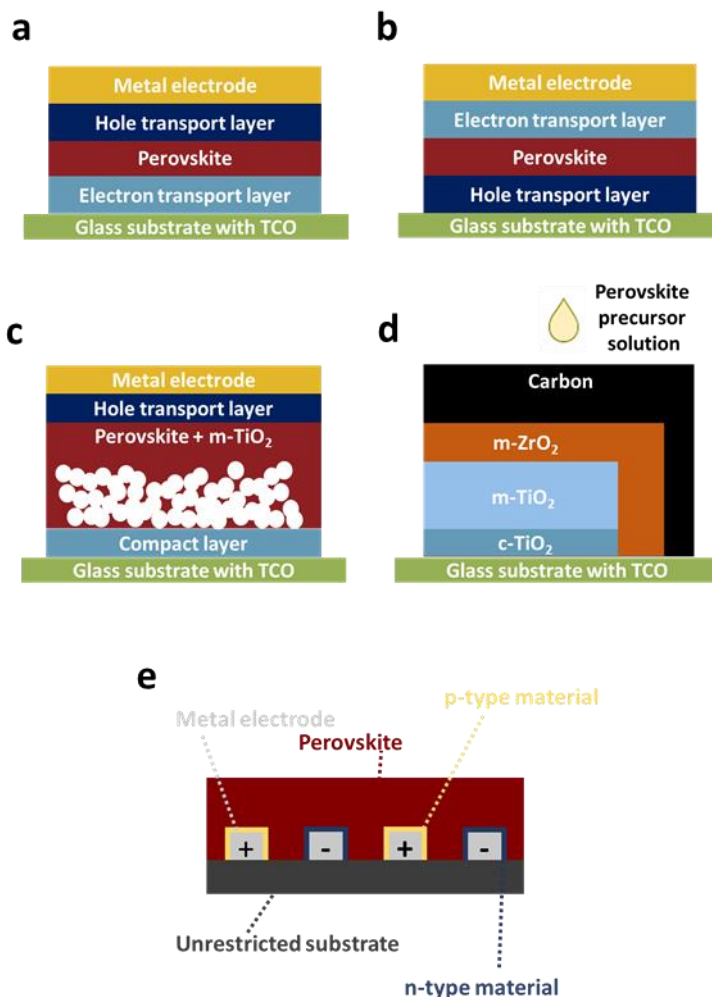
Figure 1.3. Different perovskite solar cell architectures. a) Planar *n–i–p.* **b)** Planar *p–i–n.* **c)** Mesoporous**. d)** Carbon-based HTL-free. **e)** Back-contact**.**

1.4. Perovskite nanocrystals

Colloidal semiconductor perovskite nanocrystals (NCs) are the most recent type of lead halide perovskites. These NCs are easy to process and use widely available chemical components, which makes them attractive for large-scale production. The facile and scalable synthesis of colloidal perovskite NCs, combined with tunability of the optoelectronic properties, high photoluminescence quantum yield (PLQY), and defect tolerance[38], render them a promising candidate for next-generation photonic devices, from photovoltaic cells to light-emitting diodes[39–43].

Perovskite NCs formed in the excited state *via* photon absorption can return to the ground state *via* photoluminescence (PL). For $CsPbBr_3$, NCs a linear dependence of the integrated PL intensity on excitation power with slope 1.34 has been found[44], from which the authors inferred that the PL of NCs is mainly due to spontaneous emission rather than a nonlinear phenomenon. The PLQY is a measure of the photon emission efficiency, and defined as the ratio of the number of emitted photons to the number of absorbed photons[45].

In the research on optical properties of nanosized lead halide perovskites, all inorganic cesium lead halide NCs ($CsPbX_3$, with X= Cl^-, Br^-, I^- or mixed halide systems) are receiving most attention. The structure of $CsPbX_3$ perovskites is composed of corner-linked $[PbX_6]^-$ octahedra with Cs^+ ions filling cavities between them. The structural strain arising from the high surface-to-volume ratio in NCs allows the stabilization of the perovskite phase at ambient conditions, unlike for the bulk perovskite with the same elemental composition[46,47]. $CsPbX_3$ NCs are easy to process, stable, and a viable candidate for bandgap manipulation. Protesescu et al.[38] showed that it is possible to span the PL emission of $CsPbX_3$ NCs from the ultraviolet (UV) to the near-infrared (NIR) spectral region. This is accomplished by adjusting the halide composition and using the quantum-size effect. Compositional changes can be achieved using different halide precursors or mixtures thereof in a certain ratio. The halide anions in all inorganic $CsPbX_3$ NCs can be extracted and replaced with other halides *via* a vacancy-assisted diffusion mechanism[48]. Interestingly, mixed halide perovskite NCs can also be made by ion exchange after completion of the quantum dot synthesis, for example by mixing particles initially made with different halogen atoms[48].

Properties of halide perovskites change from nanoscale, over microscale, to the bulk single crystal material. The dimension of the material not only influences its structural properties, but also optical and electronic properties[49]. As the NCs size decreases, the bandgap of the excitonic states shifts to higher energies and causes a blue shift of the PL emission[38] as a consequence of quantum confinement. When one or more dimensions of the nanoparticles are below the size of the exciton Bohr radius, the wave function of

the charge carriers becomes confined to the limiting dimension. When the NC size increases and leaves the strong quantum confinement regime, the properties will approach those of the bulk.

Colloidal perovskite NCs offer a unique platform to study fundamental properties such as structure, photoemission, absorption, and exciton binding energy. Temperature-dependent PL spectroscopy helps to obtain insight into the exciton behavior and photophysical properties of perovskite NCs[50]. Exciton-phonon coupling can be examined by analyzing changes in the width of the PL spectrum and exciton dissociation by examining PL thermal quenching. In conventional semiconductors, the peak energy where the PL has maximum intensity is red shifted due to the lattice expansion when the temperature increases[51]. Only a small group of materials, including perovskites, show opposite behavior, usually called an anomalous blue shift. This PL behavior comes from the already mentioned specific formation of the VBM and conduction band minimum (CBM) in lead halide perovskites. As the temperature increases, the thermal expansion of the lattice decreases the interaction between these two orbitals, resulting in widening of the bandgap. Hence, the anomalous blue shift at higher temperature in perovskites, arises from the destabilization of the VBM.

The relatively soft nature of the perovskite structure makes them interesting materials for investigating the effect of high pressure to gain a better understanding of how perturbation to the crystal structure affects the bandgap and optoelectronic properties. High pressure can decrease the cell volume and significantly increase the electron density[52]. Pressure is also a very efficient and simple tool to trigger structural transformations and helps achieving a better understanding of phase transitions and structure-property relations in perovskite NCs[53]. Under hydrostatic pressure, many metal halide perovskite NCs undergo solid-solid phase transitions and change of the mode of deformation as the pressure increases further, ultimately leading to amorphization at very high pressures[54]. This technique facilitates investigating the thermodynamics of materials without changing the chemical composition of the material.

1.4.1. Synthesis and growth mechanism

Perovskite NCs can have various shapes, including nanocubes, nanowires, nanospheres, nanorods, nanoplates, and two-dimensional nanosheets. However, cube-like $CsPbX_3$ NCs are most common. High quality perovskite NCs, with controlled size and shape, are usually produced *via* liquid-phase chemical reactions. The two most developed liquid-phase reactions are the hot-injection (HI) and the ligand-assisted re-precipitation (LARP) methods. In the hot-injection approach, one preheated precursor is rapidly injected into another precursor solution, while being heated[55]. The injection immediately causes the formation of

small nuclei, which continue to grow. The reaction has to be stopped during the size-defocusing regime, which is typically several seconds[56]. HI facilitates the control of the size, shape, and narrow distribution of NCs, but requires a controlled environment (air-free conditions) and is hard to scale up. Using the LARP synthesis route, NCs can be prepared under less stringent conditions, i.e., at room temperature and ambient conditions. The supersaturated recrystallization process consists of moving the solution from equilibrium concertation into a non-equilibrium state of supersaturation. LARP is a supersaturated recrystallization process in the presence of ligands. Ligands enable the formation and growth of crystals on the nanoscale. LARP is simple to scale up and opens the way for large-scale production. Protesescu et al.[38] reported the first use of HI while Li et al. were the first to use LARP to synthesize $CsPbX_3$ perovskite NCs[57]. The HI and LARP for the preparation of perovskite NCs are schematically presented in **Figure 1.4**.

The crystal growth of all-inorganic perovskite NCs has been explained in the case of $CsPbBr_3$ and can be extended to the other lead-halide NCs. To obtain a better insight into crystal growth, Wen et al.[58] introduced 1-bromohexane to decelerate this extremely fast reaction. When employed as halide precursor, 1-bromohexane provides a slow release of bromide which extends the reaction from typically a few seconds to 20 min. The chemical availability of bromide impacts the kinetics of the growth process and determines the crystal phase of the nanoparticle. Using X-ray diffraction (XRD), Wen et al. observed the formation of cubic CsBr after 2 min and hexagonal Cs_4PbBr_6 after 8.5 min along with a weak $CsPbBr_3$ signal. After 20 min, the XRD pattern showed Cs_4PbBr_6 and orthorhombic $CsPbBr_3$, while the CsBr peak vanished. This mechanism does not exclude that octahedral $[PbBr_6]^{4-}$ ions are formed in the solution but indicates that CsBr is the first to crash out before any lead-containing species. In a similar study, Koolyk et al.[59] studied the growth of cubic $CsPbBr_3$ NCs and found an average side length of 9 nm for 1 s growth. For 4 s it reaches 9.6 nm, for 20 s it is 8.4 nm, and for 40 s it is 9.3 nm. Koolyk et al. found that the full width at half maximum of the size distributions increases with the growth duration, implying an Ostwald ripening process. Since the monomer concentration is inversely proportional to the critical radius, particles smaller than the critical radius dissolve in a pool of monomers, and particles above the critical radius grow. When the monomer concentration is reduced because of the growing process, the critical radius is increased, causing dissolution of mode-sized particles and growth of larger particles. Since monomer concentration is decreasing fast in $CsPbBr_3$, to achieve a narrow size distribution, a high monomer concentration is required[59].

Ligands are critical components in the nucleation and growth in NC synthesis. Ligand molecules bind to the surface of NCs not only to protect them, but also to determine chemical behavior, passivate surface defects, and prevent agglomeration[61]. The role of ligands goes even further than that, because together with temperature they control the NC morphology (shape and size). Pan

et al.[62] reported the size and shape dependence of CsPbBr$_3$ NCs obtained by hot-injection on the chain length variation of ligands. Different pairs of alkyl amines and carboxylic acids with varying chain lengths were utilized. Using oleylamine and carboxylic acids with decreasing carbon chain lengths, nanocubes with increasing edge lengths were formed at 170 °C. However, using oleic acid and amines with shorter carbon chain lengths, afforded nanoplatelets, except in the case of oleylamine, with thinner nanoplatelets being formed for shorter chain amines. Pan et al. concluded that ammonium ions tune the growth of anisotropic platelet structures, while the stronger binding carboxylate ligands modulate the size of the relatively more isotropic nanocubes.
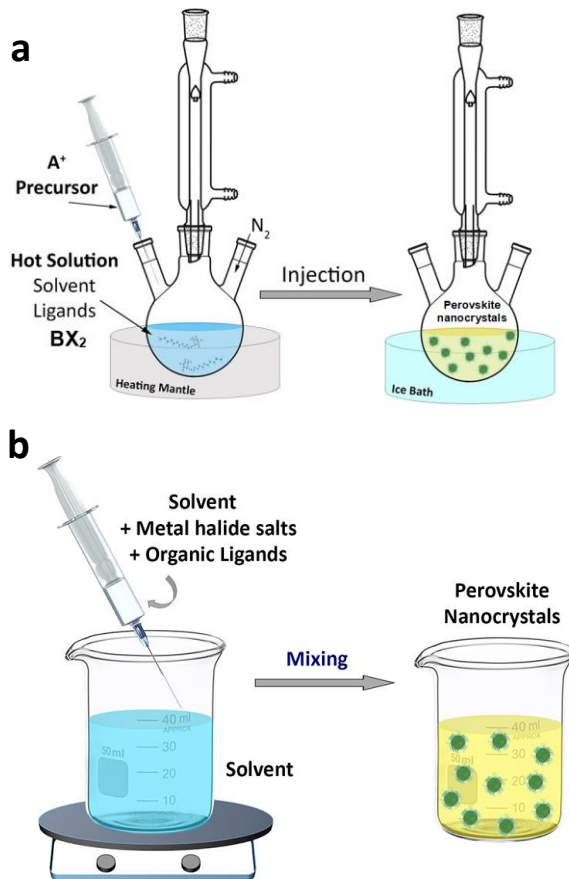
Figure 1.4. Schematic representation of the perovskite NCs with two main synthetic methods. a) Hot-injection. **b)** Ligand-assisted re-precipitation. Reprinted and adapted with permission from Ref[60] (https://pubs.acs.org/doi/10.1021/acs.chemrev.8b00644). Further permission related to the material excerpted should be directed to the ACS.

In comparison to classical quantum dots, all cesium lead halide NCs have more labile interaction with capping ligands and that is the reason why ligand binding is highly dynamic and ligands are easily removable by purification and isolation process[63]. The most common capping ligands are oleylamine, oleic acid, propionic acid, and butylamine. When oleic acid and oleylamine are used as surfactants they form an organic-inorganic interface. Carboxylic acids and long-chain amines are necessary to stabilize the surface, while amines proved to be crucial to achieve high PLQY. Long-chain hydrocarbon ligands also have a significant role in the NCs' colloidal properties and post-synthetic transformations.

$CsPbX_3$ NCs have high tolerance to surface defects, which has been attributed to lack of bonding-nonbonding interaction between the conduction and valence bands of the perovskite[64]. This tolerance was reported to be limited because the halide ions of the perovskite can form ammonium halide ion pairs with surface amine ligands that are then removed during purification[65], inducing a defect that acts as a trap state limiting the PLQY. For this reason, surface passivation, i.e., the process of rendering an inert semiconductor surface in order not to change semiconductor properties is important to improve the stability and optoelectronic properties of perovskite NCs.

1.5. Environmental impact

Although PV technology is considered essential to reach the much needed low-carbon energy scenario, the toxicity of materials used for solar cell production and installation can cause environmental hazards. In the past decade, enormous efforts were made to increase the PCE of perovskite solar cells and improve stability, but less to understand the environmental impact. The potential risk is often considered to be mostly coming from the B-site element, which is typically a heavy metal such as lead, and associated with risks of contamination of soil and water with adverse effects to flora, fauna, and humans. Heavy metals and other toxic materials can be released into the environment due to inadvertent damage to PV panels or during their disposal. It is estimated that more than 1 million of the global deaths are caused by lead contamination[66]. Solution-based deposition of perovskite is favorable for manufacturing, but at the same time causes concerns on environmental impact and impact on human health. Different polar and non-polar solvents are used to dissolve precursor solutions. The choice of solvents is often driven by yielding the best performance and less from the environmental and human health aspects. When moving from the lab-scale to large-scale production these aspects must be evaluated. To achieve full sustainability potential, the risks to marine and freshwater, soil, and human health in the production of perovskite solar cells, must be addressed.

The environmental impact of perovskite solar cells is important to determine since they are still in a process of development and the estimation of the potential risk is significant for the up-scaling process and mass production.

13

Thus, the assessment of all environmental impacts, from raw material extraction (cradle) through manufacture, use, maintenance and finally to the end of life (grave) is used to support decisions on how to improve the products. The most common method to estimate this performance is a life cycle assessment (LCA) (**Figure 1.5.**). LCA is a quantitative description of a broad range of environmental impacts. There are various impact categories, such as global warming, ionizing radiation, human health, fresh and marine water, land use, water consumption, etcetera. An LCA study identifies the major contributions to the environmental impacts and indicates where improvements other than technical can be found in future research.
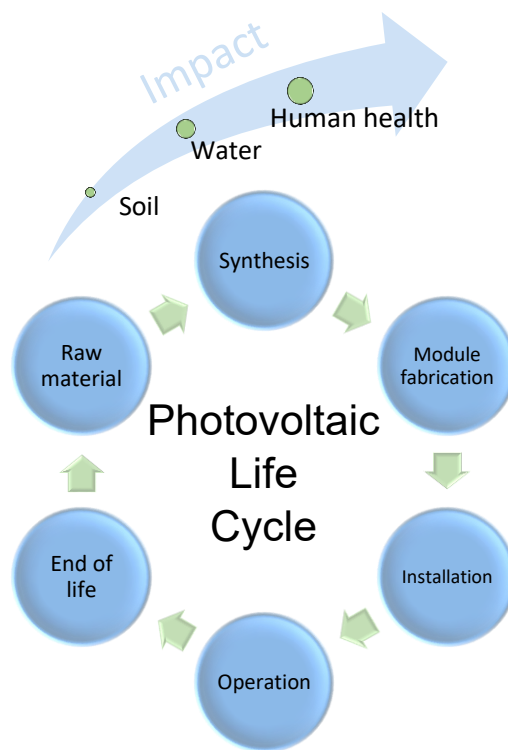
Figure 1.5. The life cycle of a photovoltaic device and its impact on the environment.

According to an LCA study performed in 2016[67], manufacturing of perovskite PV modules has 10-30% lower environmental impact than manufacturing commercially available monocrystalline silicon PV modules. Interestingly, the study reported a negligible toxicity impact of lead, coming from the perovskite absorbing layer. Gong et al. reported that higher environmental impact comes from the use of ITO substrates, organic solvents, and gold rather than from the perovskite itself[68]. Gong et al. conclude that perovskite solar

14

modules are potentially the most environmentally sustainable PV technology, when performance and lifetime can be increased. A similar conclusion was reached by Vidal et al. in their review of LCA studies. These authors conclude that in terms of energy payback time and environmental impact at industrial-scale perovskite PV are the lowest compared with commercial PVs, when using peak power as the functional unit[69].

1.6. Aim and outline of this thesis

Converting solar energy directly into chemical energy is a process called photosynthesis and occurs in green leaves of plants, already for billions of years[70]. Mimicking natural photosynthesis is enabled by an artificial leaf. An artificial leaf also converts solar energy into chemical energy and produces solar fuel such as hydrogen from water splitting or methane from carbon dioxide reduction. Creating an artificial leaf by printing technology is the objective of the eSCALED[1] project.

The process of artificial photosynthesis is a scientific challenge that can only be overcome by combining expertise in chemistry, physics, materials science, and biology. The eSCALED project brings the necessary expertise together through network entities in the private and public sectors, while training 14 early-stage researchers. The eSCALED artificial leaf aims to combine a bioinspired electrochemical stack, where H_2O oxidation and H^+ and/or CO_2 reduction are performed, with a solar harvesting unit, which captures the sunlight. The eSCALED project aims to make a step towards novel artificial leaf technology.

The focus of the research described in this thesis is on inorganic metal halide perovskites in the form of thin films and NCs, for photovoltaic purposes and with a special accent on solar cells. The work presented in this dissertation has been performed in a collaborative effort at five different institutes across Europe, as presented in **Figure 1.6**, benefiting from the specific expertise at each node.

The chapters in this thesis start with an introduction to the specific topic, followed by the experimental development of an idea, results and discussion, and ending with a conclusion. Chapters 2 and 3 address the synthesis, characterization and use of wide-bandgap inorganic perovskite NCs; Chapter 4 presents the study on the environmental impact of NC production, presented in Chapter 3; Chapter 5 focuses on the producing wide-bandgap solar cells *via* thin film deposition; Chapter 6 presents the development of polymer honeycombs structures.

---

[1] European School on Artificial Leaf: Electrodes and Devices

Chapter 2 reports the size dependent photophysical properties of $CsPbI_3$ NCs (in the range of 7 - 17 nm). Temperature and pressure were used as thermodynamic variables to control the energy and structural parameters of the $CsPbI_3$ NCs. The temperature-dependent change of the photoluminescence peak energy and linewidth can help with a fundamental understanding of the influence of both defects and electron-phonon interactions on luminescence efficiency, and their dependence on NC size. By studying the pressure response, it is possible to investigate how the lattice deformation mechanism affects the bandgap and recombination dynamics, stressing the importance of the structural engineering of this class of soft semiconductors. The study provides a useful synthesis guide for customized NCs for luminous applications. This work has been conducted at the Italian Institute of Technology, Milan.
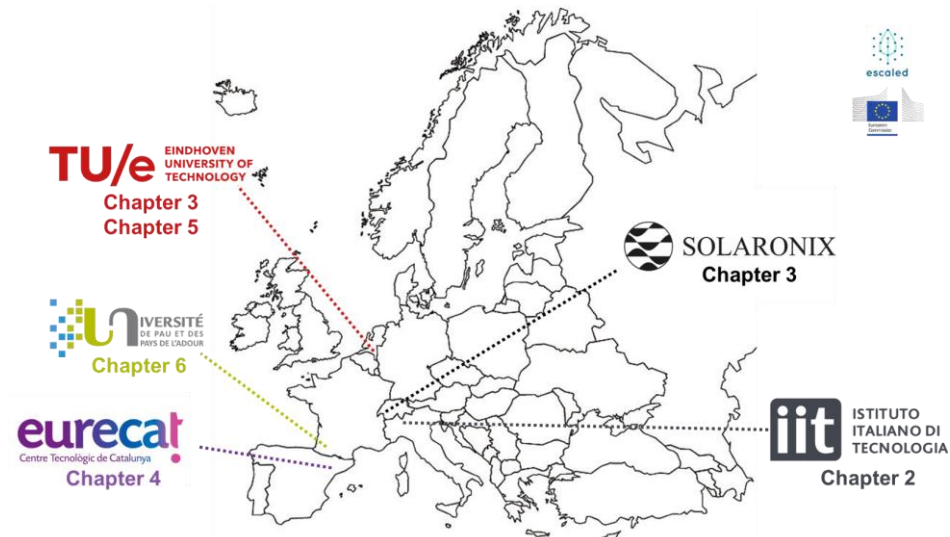
Figure 1.6. eSCALED project. The figure represents how the work reported in this thesis was performed across different institutes in Europe. The research time of slightly more than 4 years was divided between Eindhoven University of Technology, University of Pau and the Adour Region, Italian Institute of Technology, Solaronix and Eurecat.

Chapter 3 discusses two methods of synthesizing $CsPbBr_3$ NCs and the use of such NCs in solar cells. Inorganic perovskite $CsPbBr_3$ NCs have a wide bandgap (2.3 eV) and can be dispersed in hydrophobic and volatile low-boiling point organic solvents. Because of these properties $CsPbBr_3$ NCs are promising candidates for the fabrication of multi-junction solar cells. Colloidal solutions of $CsPbBr_3$ NCs were spin coated as a photoactive layer in the single-junction *n–i–p* planar structure or infiltrated as a passivation layer in the carbon-based perovskite solar cells. The work presented in Chapter 3 is conjoined work from the Eindhoven University of Technology, Eindhoven and Solaronix, Aubonne.

Results from Chapter 3 are used to conduct an LCA study. This study is presented in **Chapter 4** and provides an environmental aspect for the synthesis of the CsPbBr$_3$ NCs. The LCA study identified the major contributions to the environmental impacts, and indicated where improvements other than technical can be found in future research. This is a crucial step towards an up-scaled production of NCs. This work has been conducted at Eurecat, Manresa.

The results from Chapter 3 indicate that the use of NCs in solar cells is challenging and, hence, the focus of **Chapter 5** is on producing wide-bandgap solar cells *via* thin film deposition, in a *p–i–n* configuration planar configuration. For cells in a *p–i–n* configuration, the major contributors to the open-circuit voltage (V_{OC}) loss were identified as non-radiative recombination in the bulk of the perovskite layer and at the interface between the perovskite and the electron transport layer (ETL). To reduce trap states, the interface between the perovskite and the ETL was carefully engineered. Organic additives were introduced into all inorganic mixed halide perovskite to improve film morphology and yield devices with enhanced performance. This contributes to solving the main challenges of the wide-bandgap perovskites and achieve the high V_{OC} and high stability, required to make these materials suitable for multi-junction all-perovskite solar cells. This work has been conducted at the Eindhoven University of Technology, Eindhoven.

Chapter 6 reports the preparation of a poly(styrene-butadiene-styrene) (SBS) porous honeycomb structure, *via* the breath figure method. Porous surfaces possess a high specific surface area and are attractive for a variety of applications including solar cells. The key characteristics of SBS honeycomb porous films were investigated. This work shows that it is possible to form an organized hexagonal porous structure from an SBS copolymer, with low thickness and high resistance to elevated temperatures and solvents with different polarities. Such properties are significant for possible applications in solar cells. This work has been conducted at the University of Pau and the Adour Region, Pau.

This thesis gives an overview of wide-bandgap inorganic metal halide perovskites in the form of thin films and NCs, points out the biggest problems, and offers certain solutions. The study contains an assessment of the environmental impact.

1.7. References

1.	Shockley, W. & Queisser, H. J. Detailed Balance Limit of Efficiency of p-n Junction Solar Cells. *J. Appl. Phys.* **32**, 510–519 (1961).

2.	Chapin, D. M., Fuller, C. S. & Pearson, G. L. A New Silicon p-n Junction Photocell for Converting Solar Radiation into Electrical Power. *J. Appl. Phys.* **25**, 676–677 (1954).

3.	Our World in Data. *https://ourworldindata.org/energy*.

4.	Albrecht, S. & Rech, B. Perovskite solar cells: On top of commercial photovoltaics. *Nat. Energy* **2**, 16196 (2017).

5.	Goldschmidt, V. M. Die Gesetze der Krystallochemie. *Naturwissenschaften* **14**, 477–485 (1926).

6.	Li, C. *et al.* Formability of ABX_3 (X = F, Cl, Br, I) halide perovskites. *Acta Crystallogr. Sect. B Struct. Sci.* **64**, 702–707 (2008).

7.	Mitzi, D. B., Wang, S., Feild, C. A., Chess, C. A. & Guloy, A. M. Conducting Layered Organic-inorganic Halides Containing ⟨110⟩-Oriented Perovskite Sheets. *Science* **267**, 1473–1476 (1995).

8.	Kojima, A., Teshima, K., Shirai, Y. & Miyasaka, T. Organometal Halide Perovskites as Visible-Light Sensitizers for Photovoltaic Cells. *J. Am. Chem. Soc.* **131**, 6050–6051 (2009).

9.	Lee, M. M., Teuscher, J., Miyasaka, T., Murakami, T. N. & Snaith, H. J. Efficient Hybrid Solar Cells Based on Meso-Superstructured Organometal Halide Perovskites. *Science* **338**, 643–647 (2012).

10.	Saliba, M. *et al.* Cesium-containing triple cation perovskite solar cells: Improved stability, reproducibility and high efficiency. *Energy Environ. Sci.* **9**, 1989–1997 (2016).

11.	Chen, B., Yang, M., Priya, S. & Zhu, K. Origin of J-V Hysteresis in Perovskite Solar Cells. *J.Phys. Chem. Lett.* **7**, 905–917 (2016)

12.	Lao, Y. *et al.* The preparation method of double-blade coating to 'write' high efficiency perovskite solar cells. *Org. Electron.* **100**, 106374 (2022).

13.	Bi, Z. *et al.* High-performance large-area blade-coated perovskite solar cells with low ohmic loss for low lighting indoor applications. *Chem. Eng. J.* **446**, 137164 (2022).

14.	Hsu, H.-C., Wu, S.-H., Tung, Y.-L. & Shih, C.-F. Long-term stable perovskite solar cells prepared by doctor blade coating technology using bilayer structure and non-toxic solvent. *Org. Electron.* **101**, 106400 (2022).

15.	Deng, Y. *et al.* Scalable fabrication of efficient organolead trihalide perovskite solar cells with doctor-bladed active layers. *Energy Environ. Sci.* **8**, 1544–1550 (2015).

16.	Li, J. *et al.* 20.8% Slot-Die Coated $MAPbI_3$ Perovskite Solar Cells by Optimal DMSO-Content and Age of 2-ME Based Precursor Inks. *Adv. Energy Mater.* **11**, 2003460 (2021).

17.	Xu, K. *et al.* Slot-Die Coated Triple-Halide Perovskites for Efficient and Scalable Perovskite/Silicon Tandem Solar Cells. *ACS Energy Lett.* **7**, 3600–3611 (2022).

18.	Uličná, S. *et al.* Scalable Deposition of High-Efficiency Perovskite Solar Cells by

18

Spray-Coating. *ACS Appl. Energy Mater.* **1**, 1853–1857 (2018).

19. Amratisha, K. *et al.* Layer-by-layer spray coating of a stacked perovskite absorber for perovskite solar cells with better performance and stability under a humid environment. *Opt. Mater. Express* **10**, 1497 (2020).

20. Dou, B. *et al.* Roll-to-Roll Printing of Perovskite Solar Cells. *ACS Energy Lett.* **3**, 2558–2565 (2018).

21. Li, H. *et al.* Fully Roll-to-Roll Processed Efficient Perovskite Solar Cells via Precise Control on the Morphology of PbI_2:CsI Layer. *Nano-Micro Lett.* **14**, 1–12 (2022).

22. Wei, Z., Chen, H., Yan, K. & Yang, S. Inkjet Printing and Instant Chemical Transformation of a $CH_3NH_3PbI_3$ /Nanocarbon Electrode and Interface for Planar Perovskite Solar Cells. *Angew. Chemie Int. Ed.* **53**, 13239–13243 (2014).

23. Li, Z. *et al.* Ink Engineering of Inkjet Printing Perovskite. *ACS Appl. Mater. Interfaces* **12**, 39082–39091 (2020).

24. Min, H. *et al.* Perovskite solar cells with atomically coherent interlayers on SnO_2 electrodes. *Nature* **598**, 444–450 (2021).

25. Wang, R. *et al.* A Review of Perovskites Solar Cell Stability. *Adv. Funct. Mater.* **29**, 1808843 (2019).

26. Ng, Y. F. *et al.* Rapid Crystallization of All-Inorganic $CsPbBr_3$ Perovskite for High-Brightness Light-Emitting Diodes. *ACS Omega* **2**, 2757–2764 (2017).

27. Unger, E. L. *et al.* Roadmap and roadblocks for the band gap tunability of metal halide perovskites. *J. Mater. Chem. A* **5**, 11401–11409 (2017).

28. Caputo, M. *et al.* Electronic structure of $MAPbI_3$ and $MAPbCl_3$: importance of band alignment. *Sci. Rep.* **9**, 15159 (2019).

29. Walsh, A. Principles of Chemical Bonding and Band Gap Engineering in Hybrid Organic–Inorganic Halide Perovskites. *J. Phys. Chem. C* **119**, 5755–5760 (2015).

30. Akhil, S. *et al.* Review on perovskite silicon tandem solar cells: Status and prospects 2T, 3T and 4T for real world conditions. *Mater. Des.* **211**, 110138 (2021).

31. McMeekin, D. P. *et al.* Solution-Processed All-Perovskite Multi-junction Solar Cells. *Joule* **3**, 387–401 (2019).

32. Manjunath, V. *et al.* Perovskite Solar Cell Architectures. in *Perovskite Photovoltaics* 89–121 (Elsevier, 2018).

33. Príncipe, J., Duarte, V. C. M. & Andrade, L. Inverted Perovskite Solar Cells: The Emergence of a Highly Stable and Efficient Architecture. *Energy Technol.* **10**, 2100952 (2022).

34. Tang, M. *et al.* Toward efficient and air-stable carbon-based all-inorganic perovskite solar cells through substituting $CsPbBr_3$ films with transition metal ions. *Chem. Eng. J.* **375**, 121930 (2019).

35. Li, S. *et al.* Hole transport layer-free carbon-based perovskite solar cells with high-

efficiency up to 17.49% in air: From-bottom-to-top perovskite interface modification. *Chem. Eng. J.* 445, 140727 (2023).

36. Papadatos, D., Sygkridou, D. & Stathatos, E. Carbon-based, novel triple cation mesoscopic perovskite solar cell fabricated entirely under ambient air conditions. *Mater. Lett.* **268**, 127621 (2020).

37. Deng, S. *et al.* Back-contact perovskite solar cell fabrication via microsphere lithography. *Nano Energy* **102**, 107695 (2022).

38. Protesescu, L. *et al.* Nanocrystals of Cesium Lead Halide Perovskites (CsPbX$_3$, X = Cl, Br, and I): Novel Optoelectronic Materials Showing Bright Emission with Wide Color Gamut. *Nano Lett.* **15**, 3692–3696 (2015).

39. Huang, H. *et al.* Growth mechanism of strongly emitting CH$_3$NH$_3$PbBr$_3$ perovskite nanocrystals with a tunable bandgap. *Nat. Commun.* **8**, 996 (2017).

40. Fu, Y. *et al.* Metal halide perovskite nanostructures for optoelectronic applications and the study of physical properties. *Nat. Rev. Mater.* **4**, 169–188 (2019).

41. Stranks, S. D. & Snaith, H. J. Metal-halide perovskites for photovoltaic and light-emitting devices. *Nat. Nanotechnol.* **10**, 391–402 (2015).

42. Liu, D. *et al.* Metal halide perovskite nanocrystals: Application in high-performance photodetectors. *Mater. Adv.* **2**, 856–879 (2021).

43. Masuda, T. *et al.* All-inorganic cesium lead halide perovskite nanocrystals for solar-pumped laser application. *J. Appl. Phys.* **127**, 243104 (2020).

44. Shi, H., Zhang, X., Sun, X., Chen, R. & Zhang, X. Direct and Indirect Recombination and Thermal Kinetics of Excitons in Colloidal All-Inorganic Lead Halide Perovskite Nanocrystals. *J. Phys. Chem. C* **123**, 19844–19850 (2019).

45. Resch-Genger, U. & Rurack, K. Determination of the photoluminescence quantum yield of dilute dye solutions (IUPAC Technical Report). *Pure Appl. Chem.* **85**, 2005–2026 (2013).

46. Zhao, Q. *et al.* Size-Dependent Lattice Structure and Confinement Properties in CsPbI$_3$ Perovskite Nanocrystals: Negative Surface Energy for Stabilization. *ACS Energy Lett.* **5**, 238–247 (2020).

47. Ke, F. *et al.* Preserving a robust CsPbI$_3$ perovskite phase via pressure-directed octahedral tilt. *Nat. Commun.* **12**, 461 (2021).

48. Nedelcu, G. *et al.* Fast Anion-Exchange in Highly Luminescent Nanocrystals of Cesium Lead Halide Perovskites (CsPbX$_3$, X = Cl, Br, I). *Nano Lett.* **15**, 5635–5640 (2015).

49. Griffiths, J. T. *et al.* Effect of Size on the Luminescent Efficiency of Perovskite Nanocrystals. *ACS Appl. Energy Mater.* **2**, 6998–7004 (2019).

50. Lee, S. M. *et al.* Temperature-Dependent Photoluminescence of Cesium Lead Halide Perovskite Quantum Dots: Splitting of the Photoluminescence Peaks of CsPbBr$_3$ and CsPb(Br/I)$_3$ Quantum Dots at Low Temperature. *J. Phys. Chem. C* **121**, 26054–26062 (2017).

20

51. Cho, Y. *et al.* Temperature dependence on bandgap of semiconductor photocatalysts. *J. Chem. Phys.* **152**, 231101 (2020).

52. Mao, H. K. *et al.* Recent advances in high-pressure science and technology. *Matter Radiat. Extrem.* **1**, 59–75 (2016).

53. Katrusiak, A. High-pressure crystallography. *Acta Crystallogr., Sect. A: Found. Crystallogr.* **64**, 135–148 (2008).

54. Beimborn, J. C., Walther, L. R., Wilson, K. D. & Weber, J. M. Size-Dependent Pressure-Response of the Photoluminescence of CsPbBr$_3$ Nanocrystals. *J. Phys. Chem. Lett.* **11**, 1975–1980 (2020).

55. Yu, W. W. & Peng, X. Formation of high-quality CdS and other II-VI semiconductor nanocrystals in noncoordinating solvents: tunable reactivity of monomers. *Angew. Chem. Int. Ed. Engl.* **41**, 2368–71 (2002).

56. Manna, L., Milliron, D. J., Meisel, A., Scher, E. C. & Alivisatos, A. P. Controlled growth of tetrapod-branched inorganic nanocrystals. *Nat. Mater.* **2**, 382–385 (2003).

57. Li, X. *et al.* CsPbX$_3$ Quantum Dots for Lighting and Displays: Room-Temperature Synthesis, Photoluminescence Superiorities, Underlying Origins and White Light-Emitting Diodes. *Adv. Funct. Mater.* **26**, 2435–2445 (2016).

58. Wen, J.-R. *et al.* Chemical Availability of Bromide Dictates CsPbBr$_3$ Nanocrystal Growth. *Chem. Mater.* **31**, 8551–8557 (2019).

59. Koolyk, M., Amgar, D., Aharon, S. & Etgar, L. Kinetics of cesium lead halide perovskite nanoparticle growth; Focusing and de-focusing of size distribution. *Nanoscale* **8**, 6403–6409 (2016).

60. Shamsi, J., Urban, A. S., Imran, M., De Trizio, L. & Manna, L. Metal Halide Perovskite Nanocrystals: Synthesis, Post-Synthesis Modifications, and Their Optical Properties. *Chem. Rev.* **119**, 3296–3348 (2019).

61. Grisorio, R. *et al.* Exploring the surface chemistry of cesium lead halide perovskite nanocrystals. *Nanoscale* **11**, 986–999 (2019).

62. Pan, A. *et al.* Insight into the Ligand-Mediated Synthesis of Colloidal CsPbBr$_3$ Perovskite Nanocrystals: The Role of Organic Acid, Base, and Cesium Precursors. *ACS Nano* **10**, 7943–7954 (2016).

63. De Roo, J. *et al.* Highly Dynamic Ligand Binding and Light Absorption Coefficient of Cesium Lead Bromide Perovskite Nanocrystals. *ACS Nano* **10**, 2071–2081 (2016).

64. Kang, J. & Wang, L. W. High Defect Tolerance in Lead Halide Perovskite CsPbBr$_3$. *J. Phys. Chem. Lett.* **8**, 489–493 (2017).

65. Li, H. *et al.* Enhancing Luminescence and Photostability of CsPbBr$_3$ Nanocrystals via Surface Passivation with Silver Complex. *J. Phys. Chem. C* **122**, 12994–13000 (2018).

66. Stanaway, J. D. *et al.* Global, regional, and national comparative risk assessment of 84 behavioural, environmental and occupational, and metabolic risks or clusters

of risks for 195 countries and territories, 1990–2017: a systematic analysis for the Global Burden of Disease Stu. *Lancet* **392**, 1923–1994 (2018).

67. Celik, I. *et al.* Life Cycle Assessment (LCA) of perovskite PV cells projected from lab to fab. *Sol. Energy Mater. Sol. Cells* **156**, 157–169 (2016).

68. Gong, J., Darling, S. B. & You, F. Perovskite photovoltaics: Life-cycle assessment of energy and environmental impacts. *Energy Environ. Sci.* **8**, 1953–1968 (2015).

69. Vidal, R., Alberola-Borràs, J., Sánchez-Pantoja, N. & Mora-Seró, I. Comparison of Perovskite Solar Cells with other Photovoltaics Technologies from the Point of View of Life Cycle Assessment. *Adv. Energy Sustain. Res.* **2**, 2000088 (2021).

70. Johnson, M. P. Photosynthesis. *Essays Biochem.* **60**, 255–273 (2016).

2

Structural effects on the luminescence properties of CsPbI₃ nanocrystals

Abstract

Metal halide perovskite nanocrystals (NCs) are promising for photovoltaic and light-emitting applications. Due to the softness of their crystal lattice, structural modifications have a critical impact on their optoelectronic properties. Here, the size-dependent optoelectronic properties of CsPbI₃ NCs ranging from 7 to 17 nm are investigated, employing temperature and pressure as thermodynamic variables to modulate the energetics of the system and selectively tune interatomic distances. By temperature-dependent photoluminescence spectroscopy, we identify the luminescence quenching channels, finding increased non-radiative losses and weaker exciton-phonon coupling in larger nanocrystals, in turn affecting the luminescence efficiency. Through pressure-dependent measurements, supported by X-ray diffraction (XRD) characterization, we reveal a NC-size dependent solid-solid phase transition from the γ-phase to the δ-phase. Importantly, the optical response to these structural changes is strongly dependent on the size of the NC. The findings provide an interesting guideline to correlate the size, and structural and optoelectronic properties of CsPbI₃ NCs, which are important to tailor the functionalities of this class of soft semiconductors.

2.1. Introduction

The facile and scalable synthesis of colloidal $CsPbX_3$ (X= Cl, Br, I) lead halide perovskite nanocrystals (NCs), combined with the tunability of their optoelectronic properties, high photoluminescence quantum yield (PLQY), defect tolerance and excellent charge transport[1], render them as promising candidates for next-generation photonic devices from photovoltaic cells to light-emitting diodes[2–6]. Spectral tunability over the whole visible range can be achieved through chemical substitution and/or NC size engineering. Protesescu et al.[1] showed easy shifting of the emission wavelength for $CsPbX_3$ and $CsPb(I_{Y-1}Br_Y)_3$ from 410 to 700 nm, when changing the halide composition. The NC size plays a critical role not only by affecting the optical and electronic characteristics through quantum confinement, but also by changing the surface-to-volume ratio and consequently the structural properties[7]. Given that, the relaxed coordination geometry at the surface can locally induce different structural arrangements[8]. The relatively soft nature of the metal halide lattice can result in a wide range of structural distortions and defects that also have a huge impact on the optoelectronic properties[9–12]. This effect is particularly severe in cesium lead iodide ($CsPbI_3$) NCs, in which tensile strain allows the stabilization of its perovskite structure at room temperature, that would be otherwise thermodynamically unstable towards the conversion to the non-perovskite phase in bulk conditions[13,14].

The instability of bulk $CsPbI_3$ is due to the structure composed of corner-linked PbI_6 octahedra, with Cs^+ ions filling cavities between them. Due to the small size of Cs^+, perovskite phases made of corner-sharing octahedra are unstable at room temperature, and quickly convert to a non-perovskite phase. Bulk $CsPbI_3$ can be stable only at elevated temperatures (175 – 360 °C), having one of the three distinct perovskite crystal structures, labeled as α-, β-, and γ-$CsPbI_3$ with cubic, tetragonal, and orthorhombic crystal structures, respectively[13]. Unlike the bulk material, $CsPbI_3$ NCs are metastable as perovskite structure under ambient conditions. The structural strain arising from the high surface-to-volume ratio in NCs allows the stabilization of the perovskite phase also at ambient conditions, but the identification of the exact symmetry has been a matter of debate[15,16].

Good phase stability, favorable bandgap (around 1.73 eV), and a visible-light-absorption spectrum up to 700 nm, make $CsPbI_3$ NCs a promising material for photoelectronic devices. However, an accurate size-dependent study of perovskite NCs is required to single-out the complex contribution of particle size, quantum confinement, structural distortions, defect losses, and phonon scattering to retrieve fundamental structure-property relationships that allow a more precise and educated material design. Despite the advances in understanding the perovskite NCs photophysics,[7,15,17–26] reports investigating the size-dependence of their optical and structural properties are still very limited[7,13]. This is likely due to the challenges posed by the standard hot-injection synthesis, where limited control over the NCs nucleation and growth makes it difficult to achieve narrow

size distributions over a wide range. To properly study size-dependent properties, we first need to achieve narrow size distributions of the colloidal NCs solutions and then approach their optical and electronic characterization, by exploiting temperature and pressure as thermodynamic variables to controllably manipulate the photophysical and structural properties of the CsPbI$_3$ NCs.

Lowering temperature in structural investigation is a typical technique, which helps to obtain very precise structural data on crystallization and phase transitions. Temperature-dependent photoluminescence (PL) spectroscopy is a unique way for getting insight into the exciton behavior and photophysical properties of perovskite NCs. Exciton-phonon coupling can be examined by analyzing the PL response *via* PL peak broadening and shifting, and exciton dissociation *via* examining PL thermal quenching. Herein, measurements were conducted with a Linkam stage sample characterization chamber with controlled vacuum, humidity, and temperature. Linkam stages can be fitted with electrical connections allowing the measurement of the electrical properties of thin films and their change with temperature. Temperatures below room temperature are reached using liquid nitrogen cooling.

Given the soft nature of the perovskite lattice, pressure is an ideal post-synthesis method to investigate the structure-properties relationship by adjusting interatomic distances, lattice deformation, and band-to-band electronic overlap[15,17,27–30]. The biggest breakthrough in high-pressure research was the invention of the diamond anvil cell, which is made of two diamonds, with cut culets (tips), opposite to each other, as presented in **Figure 2.1.** In between them, there is a metal gasket (marking the surface to place the sample), the sample of interest, a pressure marker (ruby), and a hydrostatic fluid. Diamonds are used because of their hardness and transparency for ultraviolet, visible, and infrared wavelengths and very low absorption of short X-rays. Pressure is generated when the screws are tightened, and the sample is squeezed between anvils. By applying pressure, the ruby PL peaks shift towards longer wavelengths and by fitting peaks with Lorentzian profiles it is possible to determine the exact pressure. Silicon oil is applied as a pressure-transmitting medium to establish hydrostatic conditions. The choice of the pressure-transmitting medium[31] is important and depends on the maximum pressure that can be reached. Silicon oil does not dissolve samples, it is transparent, and nonreactive.

This chapter describes the investigation of size-dependent optical and structural properties of CsPbI$_3$ NCs. We employ the hot-injection synthesis method and adapt a size-selective precipitation strategy[13] to controllably isolate CsPbI$_3$ NCs with sizes ranging between the strong and weak quantum confinement regime (7 – 17 nm). Furthermore, we combine PL spectroscopy and X-ray diffraction (XRD) characterization to elucidate the size-dependent structural and photophysical properties. Low temperature luminescence measurements allow investigation of the PL quenching channels in NCs of different sizes,

identifying the critical role of exciton-phonon coupling. By loading the NCs in a diamond anvil cell, we then performed pressure dependent characterization up to 2.5 GPa, which allowed us to modulate the interatomic distances and study the effect of structural distortion and quantum confinement independently of size-related effects. We attributed the pressure response (PL peak shift, change in recombination dynamics and quenching at high pressures) to the lattice deformation mechanism, and found a different structural evolution pattern for the smallest size NCs. By highlighting the key role of the NC size, our findings shine a light on a fundamental relationship between structural and optoelectronic properties of $CsPbI_3$ NCs that can likely be applied to a wide range of perovskite systems.
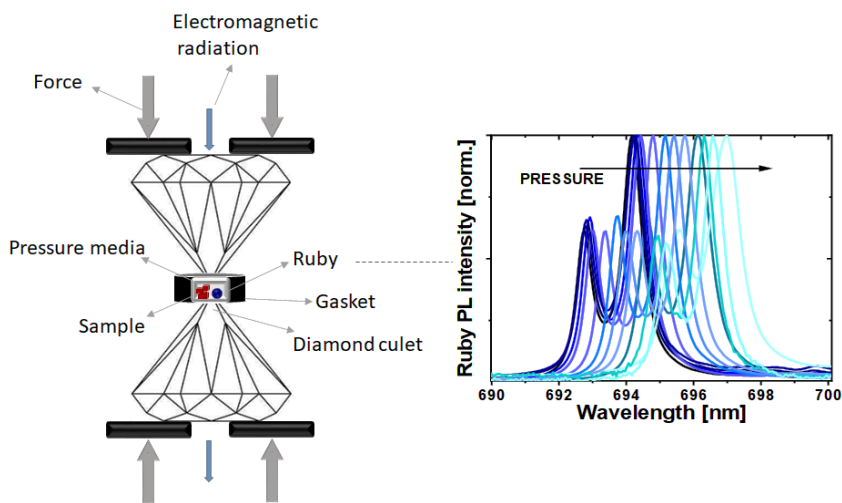
Figure 2.1. Schematic sketch of a diamond anvil cell. Two diamonds, with cut culets, are facing each other. A sample, pressure marker (ruby), and pressure-transmitting medium are placed on the surface marked by a gasket, between the diamonds. Pressure is made when force is applied. Pressure response is determined *via* the ruby PL peak shift when excited. By fitting the ruby PL peaks with Lorentzian profiles, it is possible to determine the exact pressure.

2.2. Results

2.2.1. CsPbI₃ nanocrystals solution preparation and characterization

To investigate the effect of particle size on the luminescence properties of $CsPbI_3$ NCs, we aimed at synthesizing particles in a broad range of sizes between 7 and 17 nm. Given that the Bohr radius for $CsPbI_3$ is about 12 nm[32], this range allows spanning from a strong to weak quantum confinement regime. For further characterization, we chose four solutions with 7, 10, 11, and 17 nm NC sizes.

Solutions were prepared using the previously reported hot-injection method[1]. Briefly, a precursor solution consisting of 1-octadecene (ODE), lead iodide (PbI$_2$), carboxylic acids (oleic acid - OA), and primary amines (oleylamine - OAm) was prepared at 120 °C under vacuum. Once the PbI$_2$ salt was completely dissolved, a N$_2$ flow was introduced into the flask, while heating the solution to the desired temperature (140 – 220 °C). Then, a Cs-oleate precursor was swiftly injected into the reaction flask. Within just a few seconds from the injection, the solution became turbid red. Further crystal growth and nucleation was stopped by immersing the reaction flask into an ice bath. To meaningfully study different sizes, size separation from the colloidal NC solution made *via* the hot-injection method, needs to be better than the typical size dispersion (> 10%) achieved by this synthesis method[1,13]. Since the reaction kinetics is very fast, usually completed within 5 s, control of nucleation and growth is the main challenge. Using a size-selective precipitation purification method[33] with methyl acetate (MeOAc), we were able to successfully achieve narrow size distributions. MeOAc was added to the initial colloidal CsPbI$_3$ NC solution in a volume ratio of 3:1 (NC solution/MeOAc). After centrifuging, larger NCs precipitated and the precipitate was collected and re-dispersed in *n*-hexane, while the supernatant was decanted for the next step. This same process was repeated until there was no obvious precipitate of NCs from the supernatant. Solutions were filtered and then kept in a refrigerated vial.

Representative transmission electron microscope (TEM) images in **Figure 2.2.** confirm the formation of CsPbI$_3$ NCs with cubic shapes and sizes of 7 ± 0.9, 10 ± 1, 11 ± 1 and 17 ± 4 nm. The largest particles show a higher deviation from the average size. This is not surprising since the biggest NCs are the first to precipitate in the size-selective precipitation. This is not considered as a problem because in the weak quantum confinement regime the properties are less sensitive to the size variation. To confirm the structure of the NCs, we performed X-ray diffraction (XRD) on drop-casted samples on a Si-wafer substrate (**Figure 2.3.a**). The diffractograms indicate the formation of the orthorhombic γ-phase (**Figure 2.3.b**), in agreement with other recent results[26, 34].

Absorption and PL spectra of four chosen solutions are presented in **Figure 2.4.a, b**. Due to the strong quantum confinement inside the NCs, optical excitations create a stable exciton population with large binding energy at room temperature, resulting in a sharp band edge absorption in the red spectral region (**Figure 2.4.a**) and a PL spectrum (**Figure 2.4.b**) with a small Stokes shift and a narrow full width at half maximum (FWHM) of 35 nm. Both absorption and PL spectra strongly depend on particle size. The smallest particles exhibit the strongest degree of quantum confinement, resulting in a more pronounced excitonic absorption peak at 645 nm for 7 nm size. As the NC size increases, the degree of quantum confinement experienced by the excitons decreases and the energy gap of the excitonic states is shifted to lower energies, resulting in a red

shift of the absorption and PL. With increasing NC size, the excitonic peak becomes less pronounced as the bandgap narrows.

a

b
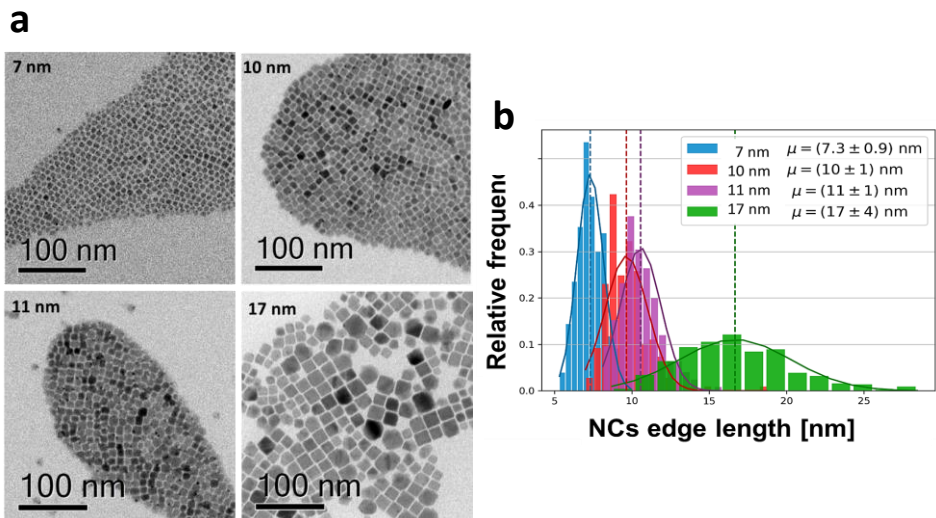
Figure 2.2. Transmission electron microscopy (TEM) images of four different CsPbI₃ NC samples. a) TEM images revealing cubic shape and average sizes of 7, 10, 11, and 17 nm. **b)** The solutions have a narrow size distribution (<1 nm) with an exception for the 17 nm solution. This is not surprising since the biggest NCs will precipitate first in the size-selective precipitation.

a

b
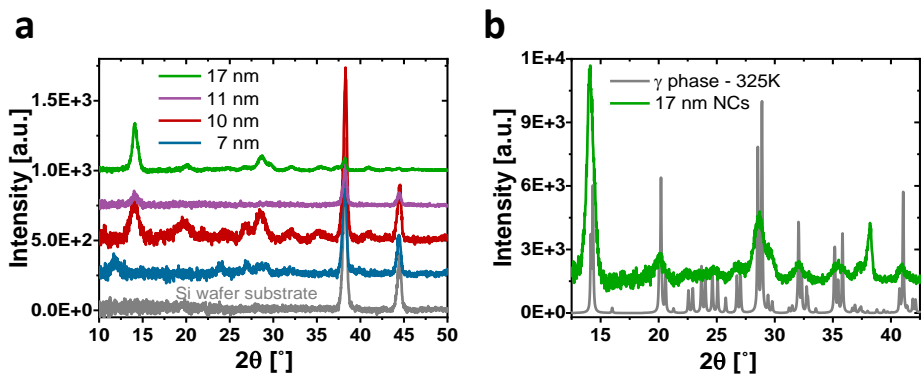
Figure 2.3. X-ray diffraction (XRD) pattern of CsPbI₃ NCs. a) XRD of four different solutions (7, 10, 11, and 17 nm) spin coated on a Si wafer substrate. The scattering intensity is lower for smaller size NCs. **b)** Comparison of the XRD experimental pattern of the 17 nm NCs with the simulated XRD pattern for the CsPbI₃ γ-phase (325 K), showing an excellent match in good agreement with the most recent reports[34].
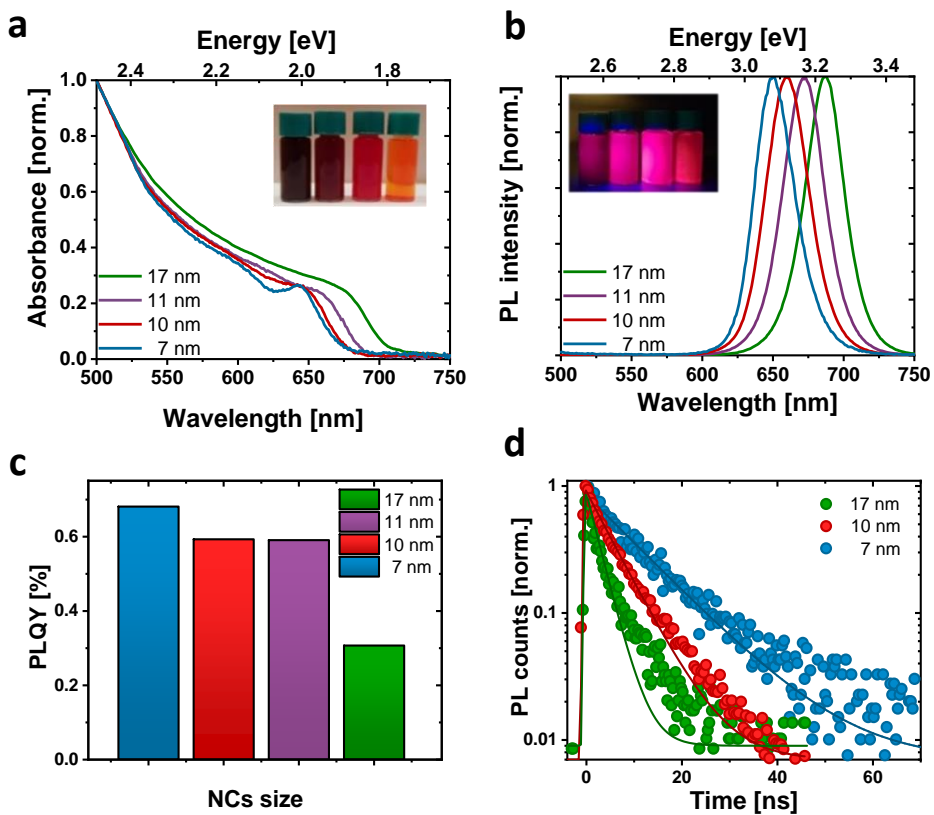
Figure 2.4. Characterization of size-dependent optical properties of CsPbI₃ NCs. a) Absorption spectra of colloidal solutions. A sharp band edge absorption is present in the red spectral region. **b)** PL spectra of colloidal solutions showing a small Stokes shift and a narrow FWHM of around 35 nm. **c)** PLQY of colloidal solutions, measured at 1.7 W/cm². **d)** TRPL decays for thin films of NCs at a fluence of 0.5 W/cm², recorded with a repetition rate of 2 MHz. With increasing NC size, the PL lifetime shortens.

The NC size not only affects the luminescence color but also the absolute PLQY (**Figure 2.4.c**). For an in-depth investigation, we considered the smallest and the largest NCs (7 and 17 nm respectively) as extreme cases and selected the 10 nm NCs as an intermediate case study. The absolute PLQY is measured under continuous wave (CW) excitation with a 405 nm laser at a fluence of 1.7 W/cm². The solutions show a remarkable PLQY of up to 70% for the 7 nm NCs and a reduction to less than 40% as the NC size increases to 17 nm. For the 10 and 11 nm NCs PLQY values, respectively 58% and 59%, were measured. This can be explained in light of the relatively broad polydispersity compared to the small difference in their average size (**Figure 2.2.b**), which does not allow to identify different PLQY characteristics. Therefore, it was decided to take the 10

nm NCs as representative case for the intermediate size for the following in-depth analysis.

To better understand the correlation between PLQY and crystal size we performed time-resolved photoluminescence (TRPL) measurements on drop-casted NC films. **Figure 2.4.d** shows the PL decays fitted with a single exponential. Particularly for larger particles, a small, long-lived component can be observed on top of the fast decay, with a decay time of the order of tens of ns. However, since it accounts for less than 5% of the observed amplitude decay, we are not considering its effects for the following discussion. An increase in PL lifetime from 3 to 11 ns is observed as the NC size decreases. Together with the corresponding increase in PLQY, this indicates a more significant contribution of the non-radiative recombination channel in the larger particles. To get an indication about the relative contribution of radiative and non-radiative recombination channels in different NCs, we consider that the observed PLQY can be expressed as the ratio between the radiative recombination rate k_{rad}, and total recombination rate $k_{tot} = k_{rad} + k_{non\,rad}$. Hence, from a measurement of the absolute PLQY (Eqn. 1):

$$\text{PLQY} = {k_{rad}}/{(k_{rad} + k_{non\,rad})} \tag{1}$$

together with the PL decay time (Eqn. 2)

$$\tau = {1}/{k_{tot}} \tag{2}$$

we can estimate the radiative and non-radiative contribution to recombination rates.

The results are summarized in **Table 2.1**. This simple model does not aim at an exact quantitative determination, for which much more detailed modeling of the recombination channels is required[35], but nevertheless, it allows for a comparison of the relative importance of radiative and non-radiative recombination channels across crystal sizes. Indeed, the results show that while the radiative recombination rate is relatively similar going from 7 to 17 nm NCs, changing less than a factor of 2, the non-radiative contribution is strongly size dependent, with an order of magnitude difference between the smallest and largest particles.

This observation can be rationalized by considering the larger surface-to-bulk ratio in smaller crystals, where binding to ligands ensures passivation of surface defects, reducing non-radiative losses and increasing the quantum yield. In larger NCs bulk defects represent a larger contribution compared to the well-passivated surface, resulting in a comparatively smaller emissivity.

Table 2.1. Effect of nanoparticle size on the relative importance of radiative and non-radiative recombination.

NC size (nm)	τ (ns)	PLQY	k_{rad} (1/ns)	$k_{non-rad}$ (1/ns)
7	11.40 ± 0.10	0.68	60	30
10	5.97 ± 0.05	0.59	100	70
17	2.98 ± 0.05	0.31	110	240

2.2.2. Low temperature-dependent study

CsPbI$_3$ NCs were deposited as thin films, by spin coating the colloidal solutions onto glass substrates, and drying under N$_2$ flow, multiple times, to ensure adequate substrate coverage. The PL measurements were conducted in vacuum, between 77 K and room temperature, under 405 nm CW excitation and the corresponding PL spectra are shown in **Figure 2.5**. We considered the smallest and the largest NCs (7 nm and 17 nm respectively) as extreme cases and the 10 nm NCs as an intermediate case study. With increasing temperature, we observe three main phenomena: a blue shift of the bandgap, a broadening of the PL, and a complex trend for the PL intensity. The rate of each phenomenon is size dependent. While the strongly quantum confined 7 nm NCs show only a moderate peak shift and relatively small changes in the FWHM and intensity, the 17 nm NCs show a larger blue shift and broadening, together with a more pronounced change in emission intensity. Intermediate NCs 10 nm exhibit a moderate blue shift but pronounced changes in broadening and intensity.

The integrated area under the PL spectrum is shown in **Figure 2.6.a**, normalized to its value at 77 K for easier comparison. The luminescence first decreases with heating, as scattering with a larger population of thermal phonons becomes more prominent, but then shows a recovery of intensity at temperatures higher than 200 K. This effect is the most prominent for the 17 nm NCs, which show a significant temperature dependent quenching with 70% luminescence loss, as well as a smaller recovery compared to the 10 nm NCs. Conversely, the PL of the smallest NCs is not as strongly affected, losing only 20% of PL intensity upon heating. Temperature-dependent absorption spectra do not show similar drastic changes at 200 K (**Figure 2.6.b**), suggesting that there is no phase transition involved in the process, and rather pointing to the conclusion that the PL recovery is more likely due to the de-trapping from non-emissive states. Excitonic peak is only present at lower temperatures when the excitonic binding energy is larger than thermal energy. At low temperatures, defects capture carriers resulting in non-radiative recombination. As the temperature increases,

the trapped carriers can gain enough energy from collisions with the surrounding environment to overcome the energy barrier for de-trapping and contribute to the emission, leading to the observed increase of PL intensity. The emerging picture is consistent with the conclusions drawn previously from static PL measurements (**Figure 2.4**.): in larger particles, the contribution from bulk defects is more significant due to the smaller surface-to-volume ratio. This results in a decrease in PLQY as well as PL lifetime, and more significant changes in temperature-dependent quenching, as de-trapping becomes more prominent.
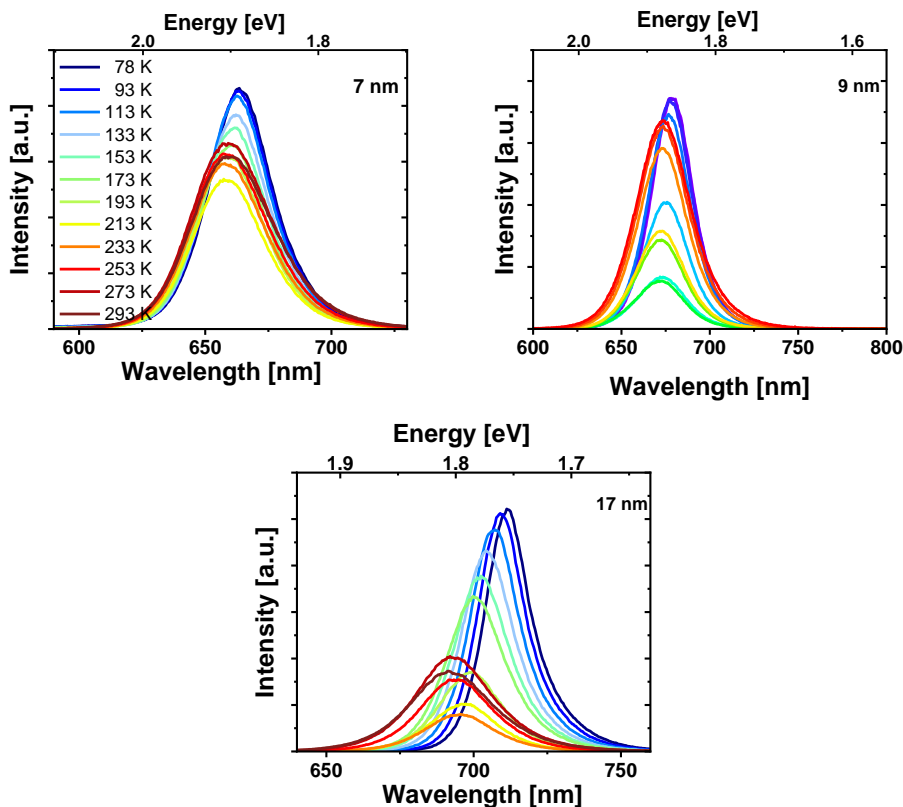
Figure 2.5. Temperature-dependent PL spectra for three different NC sizes. PL spectra of the 7, 10, and 17 nm NCs as a function of temperature, under CW excitation at 405 nm. Graphs indicate three main phenomena with increasing temperature: anomalous blue shift of the bandgap for semiconductors (but characteristic for perovskite), a broadening of the PL, and a variation in PL intensity, with inflection points observed at around 200 K.

However, the significant changes of intensity and linewidth with temperature also suggest a large involvement of electron-phonon coupling, whose strength can be studied *via* its effect on the temperature dependent PL linewidth (**Figure 2.6.c**). The total PL linewidth arises from intrinsic

inhomogeneities, acoustic phonon scattering, and optical phonon scattering[36]. The main source of thermal variation for PL width is the change in phonon population. While the contribution from the acoustic phonon population is only significant at much lower temperatures, for $T > 100$ K the scattering with longitudinal optical (LO) phonons represents the dominant broadening mechanism[37]. In our analysis, we thus neglect contributions from acoustic phonons and only consider intrinsic inhomogeneities and exciton-longitudinal optical phonon coupling. These different mechanisms of scattering between charge carriers and phonons or impurities can be expressed by Segall's expression (Eqn. 3)[38]

$$\Gamma(T) = \Gamma_{inh} + \frac{\Gamma_{LO}}{e^{\frac{E_{LO}}{kT}} - 1} \tag{3}$$

where Γ_{inh} is an inhomogeneous broadening constant, Γ_{LO} is an exciton-longitudinal optical phonon coupling coefficient and E_{LO} is energy of the LO phonons. The fits presented as solid lines in **Figure 2.6.c** are in good agreement with the measured data and the estimated model parameters are summarized in **Table 2.2.**

Table 2.2. Temperature-dependent FWHM: an estimate of parameters related to exciton-phonon coupling.

NC size (nm)	Γ_{inh} (meV)	Γ_{LO} (meV)	E_{LO} (meV)
7	82.8 ± 0.3	129 ± 14	43 ± 2.4
10	76.0 ± 1.4	90 ± 11	41 ± 4.8
17	43.7 ± 0.9	71 ± 12	26 ± 3.0

We find longitudinal optical phonon energies of 10s of meV, well in line with typical LO modes. The largest NCs have E_{LO} = 26 meV, which is in agreement with values reported in the literature for phonon modes in CsPbI$_3$[39]; smaller particles on the other hand show larger phonon energies around 40 meV. Such behavior can be explained in strongly confined systems where modes of comparable size with the NC can experience energy shifts due to the influence of surface modes[40,41]. The energy of optical phonons is a significant parameter to assess the effect of phonon scattering on radiative excitonic recombination: as the reported exciton binding energy of CsPbI$_3$ at room temperature is estimated to be 20 meV[1], phonon scattering does not represent a significant exciton dissociation path at cryogenic temperatures, but might be detrimental at room temperature conditions[24]. Inhomogeneous broadening has a strength between 44 and 83 meV, while broadening due to phonon coupling is the dominant contribution, with values from 71 to 129 meV. Both the inhomogeneous

broadening and LO-phonon coupling are reduced in larger particles. For inhomogeneous broadening, this can be related to a more significant size variability of smaller NCs and to the larger contribution from the surface, where ligand distribution might be uneven. The temperature-dependent PL broadening is instead mostly due to electron-phonon interaction. Here again, we find a more pronounced effect of phonon coupling in particles smaller than 10 nm.

a

b

c

d
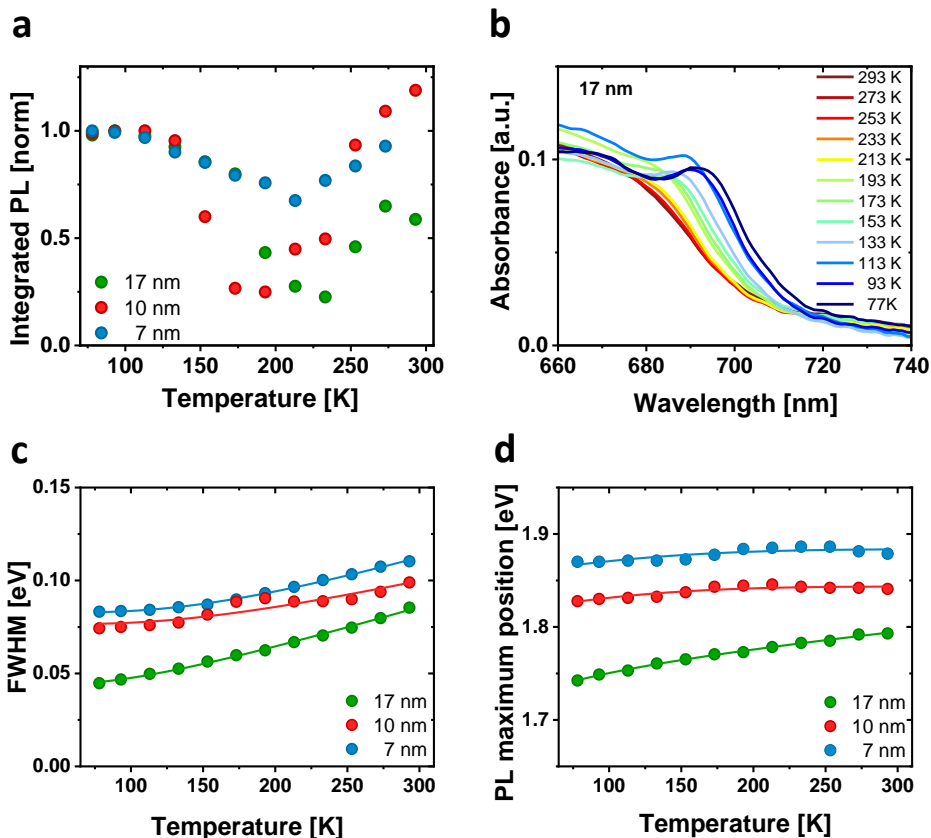
Figure 2.6. Temperature-dependent PL. a) Integrated PL intensity, normalized to the value at 77 K: the decrease in luminescence and subsequent recovery as the temperature is increased suggests the presence of non-radiative states that can be accessed at higher temperatures. **b)** Temperature dependent absorbance of the 17 nm NCs: no phase transition is observed between 77 and 300 K. It is the same for other sizes. **c)** Temperature dependence of the PL FWHM and corresponding fit (solid lines) with Eqn. 3. **d)** Change of PL peak position with temperature and corresponding fit (solid lines) with Eqn. 4.

The PL peak energy $E_g(T)$ (**Figure 2.6.d**) is blue shifted as the temperature increases across all particle sizes because of the lattice thermal expansion. The relative shift is related to electron–phonon (EP) interaction and lattice thermal expansion through a single oscillator model (Eqn. 4)[42]

$$E_g(T) = E_0 + A_{TE}T + A_{EP}\left[2\Big/\left(e^{\frac{\hbar\omega}{kT}} - 1\right) + 1\right]$$ (4)

where E_0 is the un-renormalized bandgap, A_{TE} and A_{EP} are the weights of the thermal expansion and carrier-phonon interaction, respectively, and $\hbar\omega$ represents the average optical phonon energy. Parameters obtained from the temperature-dependent PL peak fitting are reported in **Table 2.3.** As expected, due to quantum confinement the normalized bandgap $E_g(T = 0) = E_0 + A_{EP}$ decreases with increase in NC size. The thermal expansion A_{TE} on the other hand is increased. The more pronounced effect of phonon coupling in particles smaller than 10 nm is also corroborated by the trend in the weight of the carrier-phonon interaction, A_{EP} (**Table 2.3.**).

Table 2.3. Parameters obtained from the temperature-dependent PL peak fitting.

NC size (nm)	$E_g(T = 0)$ (eV)	A_{TE} 10^{-4} (eV/K)	A_{EP} (eV)
7	1.856	1.97 ± 0.78	-0.066 ± 0.041
10	1.809	2.29 ± 0.63	-0.067 ± 0.026
17	1.721	5.01 ± 0.54	-0.050 ± 0.010

In NCs, phonon propagation can be disrupted by scattering from the NC surface, causing phonon confinement within the nanograin[43] and enhancing the coupling of exciton with lattice phonons in smaller particles[44]. In addition, bonding with ligands has also been shown to enhance EP coupling[45]: again, a larger contribution of the bulk can explain the lack of observed enhancement for less strongly confined NCs.

2.2.3. Pressure-dependent study

The size-dependent optical response (evolution of the PL response) of the NCs to the application of hydrostatic pressure is studied by placing drop-casted NCs in a diamond anvil cell. The sample was loaded several times and dried under a N_2 flux between the depositions. Ruby powder was used as a pressure marker and silicon oil as a pressure-transmitting medium. The PL evolution with pressure shows a similar trend, for all different NC sizes in this study, with some exceptions for the smallest particles, as presented in **Figure 2.7.a**. Initially, the PL peak energy remained nearly constant up to 0.35 GPa, with a minimal red shift of about 1-5 meV (**Figure 2.7.b**). A small red shift was followed by an abrupt blue shift at higher pressure up to 2.5 GPa. Considering the specific composition of metal halide perovskite band structure, such change can be ascribed to two different deformation modes of the crystal lattice: compression of the Pb-I bonds, followed by tilting of the PbX_6 octahedra[17,15,20,34].

For CsPbI$_3$, the valence band maximum (VBM) originates from the antibonding interaction of Pb 6s and I 5p electronic orbitals while the conduction band minimum (CBM) arises primarily from the I 5p orbitals and Pb 6p orbitals[46]. The reduction of the unit cell volume at higher pressures proceeds in the first phase with the compression of the lead iodide octahedra. The reduced Pb-I bond length enhances the orbital overlap bringing the Pb 6s and I 5p orbitals closer. This destabilizes the VBM and pushes it to higher energies, reducing the bandgap[17]. On the other hand, the CBM is largely unaffected by octahedral compression because of the nonbonding character of the CBM, and small changes in the Pb−I distance will not have a destabilizing effect. The resulting bandgap narrowing rationalizes the initial red shift seen at low pressures. Similar considerations apply to the PL red shift observed at lower temperatures, which follows the lattice contraction (**Figure 2.5.** and **Figure 2.6.**). Conversely, above 0.35 GPa, the lattice deformation through the tilt of the PbI$_6$ octahedra becomes dominant, and the smaller Pb-I-Pb bond angles decrease the electronic band dispersion, opening the bandgap with a consequent blue shift of the PL[9,10,28]. A schematic representation of these structural changes is given in **Figure 2.7.c**.

Previous reports have shown that small CsPbI$_3$ NCs possess a lower octahedral tilt, being closer to a cubic symmetry than their bigger counterparts[13] and this might affect their deformation behavior under pressure. During the whole pressurization cycle, the PL intensity is gradually quenched before finally disappearing (**Figure 2.7.d**). While the trend in PL peak shift is retained for all NCs sizes, we note that the rate of change of the peak position with pressure above 0.35 GPa is smaller for the smallest NCs (7 nm). However, a more drastic change occurs in the PL quenching behavior. While the darkening occurs around 2.5 GPa for the biggest size NCs, we observe the total PL quenching of the 7 nm NCs already at 1.25 GPa.

To understand the origin of this behavior, we performed pressure-dependent XRD analysis (**Figure 2.8.a**), focusing on the 17 nm NCs, which provided the best diffraction intensity. In the range 24° − 27° we probed an evolution of the diffraction peaks with the gradual appearance of a new pattern at high pressure, suggesting the occurrence of a solid-solid phase transition from the initial orthorhombic perovskite (γ-phase) to the δ-phase. While a few reports suggest the loss of long-range order at high pressures[10,15, 27,47], we did not probe clear signs of amorphization in our measurement range up to 6 GPa. The results are in good agreement with the changes we observed in the PL intensity. The δ-phase is a poorly emissive non-perovskite structure with a much larger bandgap of about 3.0 eV. While at mild pressures there is still enough emissive γ-phase to produce a strong PL signal, at higher pressure the non-emissive δ-phase takes over and luminescence rapidly diminishes until it is quenched. As we expected the phase transition to proceed from a nucleation site in the NCs[7,48], the fluctuation length scale triggering the structural change could be shorter in smaller NCs, where the higher surface-to-volume ratio could also allow greater

36

surface fluctuations of the octahedral tilt favoring structural rearrangements[8]. This supports why PL quenching occurs much earlier for the 7 nm NCs than for the bigger NCs. Interestingly, the pressure-induced change is fully reversible in the investigated range of pressures (**Figure 2.8.b**).
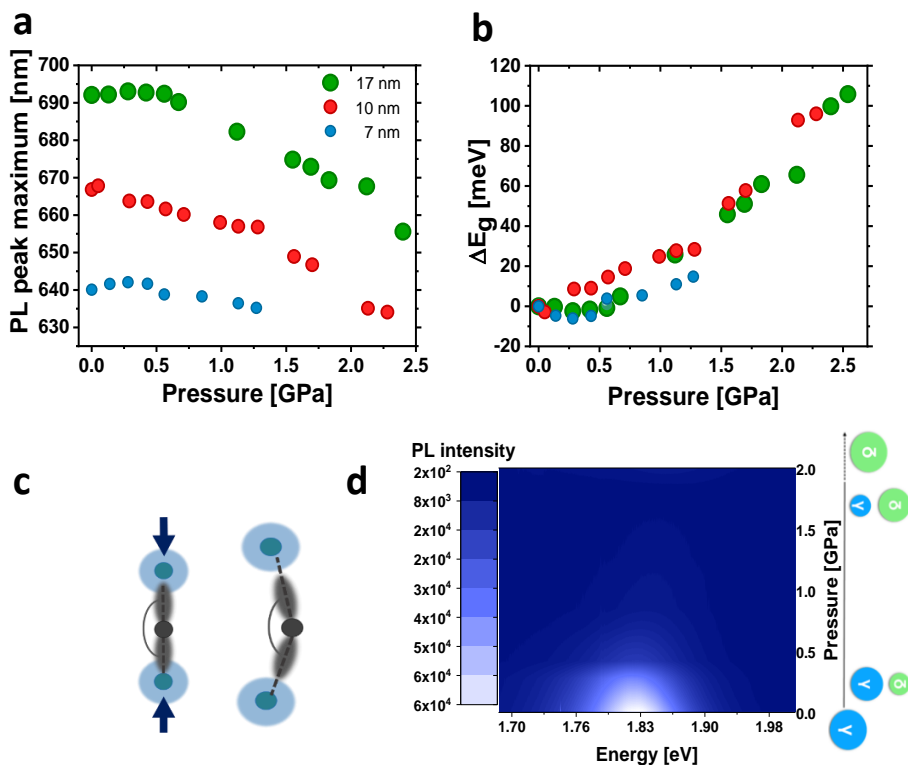
Figure 2.7. PL pressure response of CsPbI₃ NCs of different size. **a)** PL peak shift of CsPbI$_3$ NCs with sizes of 7, 10, and 17 nm. **b)** Bandgap energy changes as the deviation of the PL peak at a given pressure from the ambient peak position. **c)** Schematic representation of the deformation mechanisms of Pb-I bonds. When the pressure initially increases, the Pb-I bonds start to shorten, which increases the orbital overlap and results in bandgap narrowing and a red shift of the PL. Further increase in pressure starts to tilt the octahedra, decreasing the Pb-I-Pb angle (<180°) and decreasing the orbital *overlap,* causing the increased bandgap and a blue shift of the PL. **d)** Representative pressure-dependent PL spectra of 10 nm NCs, showing gradual quenching of the PL intensity with pressure. The green circles represent the δ-phase, and the blue circles represent the γ-phase.

a

b
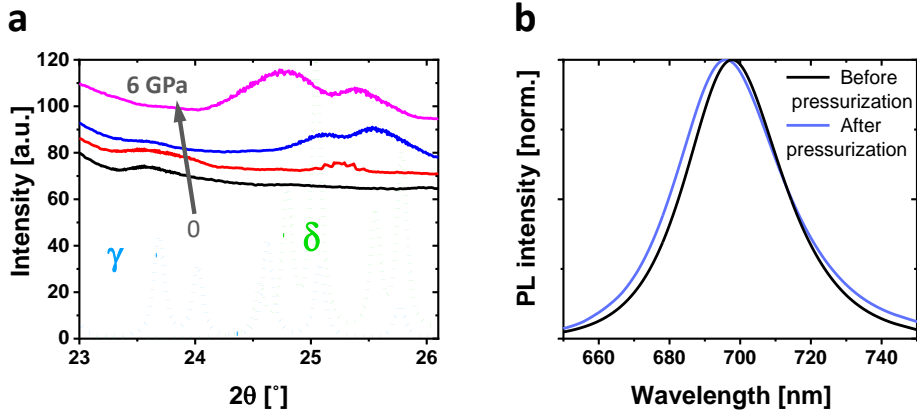
Figure 2.8. Effects of pressurization a) Pressure dependent XRD. The continuous lines show the experimental data at 0 (black), 0.13 (red), 1.85 (blue), and 6.14 GPa (magenta). The dotted lines show the calculated diffraction pattern for $CsPbI_3$ γ-phase (light blue) and δ-phase (green). With increasing pressure, the peak at 23.7° (γ-phase) gradually disappears, while two new peaks at 25.1° and 25.6° arise indicating formation of the δ-phase. **b)** PL spectra recorded for NCs at atmospheric pressure before applying pressure (black line) and after the release of the highest applied pressure (blue line). During the whole pressurization cycle, the PL intensity is gradually quenched before finally disappearing, but the pressure-induced changes are fully reversible, in the investigated range of pressures.

Finally, we investigated the effect of structural deformations on the exciton recombination through time-resolved PL measurements as a function of pressure, focusing on an intermediate NC size (**Figure 2.9.a, c**). As the pressure is increased, the PL at first decays more rapidly, but at pressures higher than 1 GPa the luminescence clearly becomes more long-lived and cannot be well described by a single exponential decay. To accommodate data at all pressures, we fit the PL decays with a double exponential function (Eqn. 5)

$$I(t) = A_1 \cdot e^{-t/\tau_1} + A_2 \cdot e^{-t/\tau_2} \tag{5}$$

where A_1 and A_2 are corresponding fractional amplitudes, and τ_1 and τ_2 are the fast and slow decay times, respectively. The results are reported in **Table 2.4**. The fast decays are typically a couple of ns and relatively independent of pressure, while the slow decay times vary from 7 to 20 ns. Interestingly, the evolution of the PL kinetics (**Figure 2.9.b**) closely follows the trend of the PL peak shift and can be equally divided into two main trends. In the Pb-I compression region (< 0.35 GPa) the lifetime is getting shorter with an increase in pressure, while a marked prolongation of the lifetime is observed at higher pressurization. This is not consistent with defect formation upon compression, which would lead to a decrease of the carrier lifetime,[49,50] and possibly indicates structural robustness of the NCs against defect formation. The increase in lifetime is instead

38

consistent with the lattice distortion occurring at higher pressure: as the Pb-I-Pb bond angles are deformed, so is the band structure, resulting in a loss of overlap between the electronic states responsible for exciton formation. This results in a reduction of the recombination rate[51,52,53] and consequently an increase in PL lifetime, stressing the key role of controlling the structural properties to modulate the recombination dynamics of these complex semiconductors.
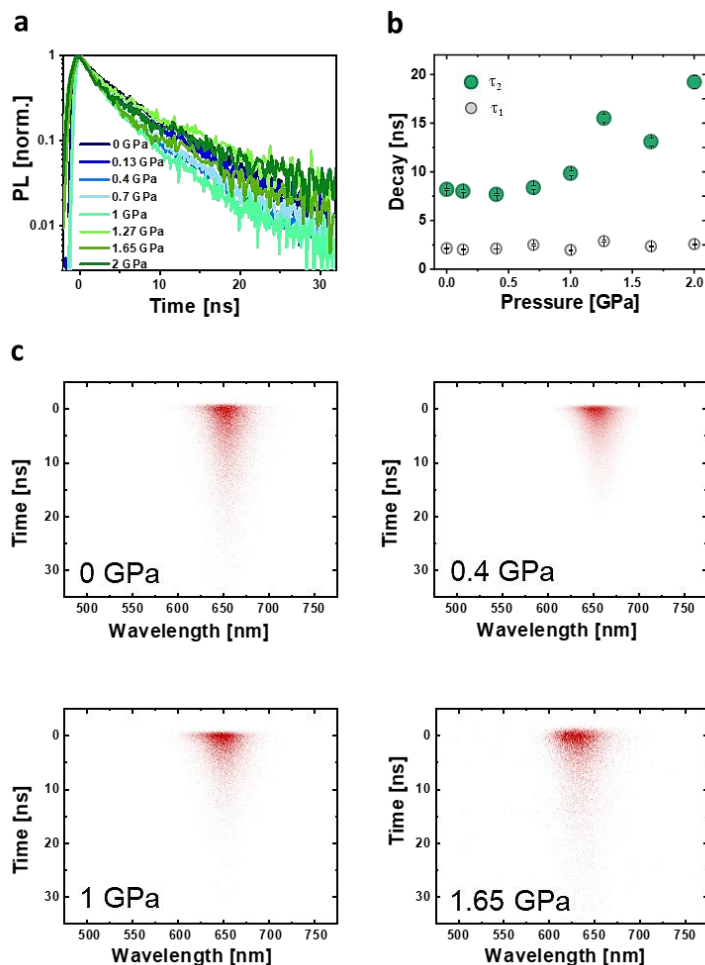
Figure 2.9. TRPL measurements as a function of pressure. a) Evolution of PL kinetics as a function of pressure for the intermediate size particles (10 nm): the initial decrease in a lifetime upon pressurization is then reversed at even higher pressures. The data is retrieved by the TRPL maps by integrating the PL spectra in 600– 675 nm. **b)** TRPL results: evolution of PL kinetics as a function of pressure, for 10 nm NCs. Exponential data are fitted with bi-exponential Eqn. 5 extracting fast and slow decay time. **c)** Representative TRPL data at different pressures, showing the luminescence maps as detected in time-resolved single photon counting mode.

Table 2.4. Parameters obtained from the double-exponential fit of the pressure dependent PL decays.

Pressure (GPa)	A_1	τ_1 (ns)	A_2	τ_2 (ns)
0	0.35 ± 0.02	2.30 ± 0.1	0.65 ± 0.02	7.9 ± 0.2
0.13	0.65 ± 0.02	2.28 ± 0.08	0.40 ± 0.01	8.2 ± 0.2
0.40	0.75 ± 0.01	2.07 ± 0.04	0.25 ± 0.01	7.0 ± 0.1
0.70	0.84 ± 0.02	2.52 ± 0.06	0.25 ± 0.02	7.9 ± 0.3
1.00	0.75 ± 0.02	1.99 ± 0.06	0.25 ± 0.02	6.3 ± 0.2
1.27	0.75 ± 0.02	2.8 ± 0.100	0.25 ± 0.02	12.1 ± 0.5
1.65	0.80 ± 0.04	2.0 ± 0.200	0.20 ± 0.03	8.5 ± 0.6
2.00	0.81 ± 0.03	3.3 ± 0.200	0.19 ± 0.03	16.4 ± 1.8

2.3. Conclusion

In this work, we have investigated the size-dependent photophysical properties of $CsPbI_3$ NCs (in the range of 7 − 17 nm) by employing temperature and pressure as thermodynamic variables to controllably modulate the energetic and structural parameters of the system. The temperature dependent PL peak energy and linewidth highlight the influence of both defects and electron-phonon interaction on efficient luminescence, and their dependence on NC size. We find that the level of surface coverage not only directly affects the availability of non-radiative loss channels but also affects the NCs luminescence through more subtle phonon coupling effects, which increase in strength in smaller nanoparticles. This observation stresses the need for careful consideration of the chosen ligands. Since electron-phonon coupling sets a fundamental intrinsic limit to charge transport, it is closely related to the optoelectronic properties and thus to technological applications[54]. Understanding electron-phonon coupling dependence on the NC size and how to control it provides useful synthetic guidelines for tailoring NCs for light-emitting applications.

By studying the pressure response, we identify fundamental structure-properties relationships of the NCs. We observe a solid-solid transition from the γ-phase to the δ-phase at high pressures with a transition pressure that becomes lower for smaller size NCs. This likely contributes to the progressive PL quenching at high pressures. Furthermore, it demonstrates that the lattice deformation mechanism strongly affects the material's bandgap and recombination dynamics stressing the importance of the structural engineering of this class of soft semiconductors.

40

2.4. Methods

Synthesis and sample preparation

Cs-oleate: In a 25 mL three-neck flask, we first added 0.200 g Cs_2CO_3 (cesium carbonate), 10 mL ODE (1-octadecene), and 0.65 mL OA (oleic acid). The mixture was degassed at 120 °C for 30 min under vacuum to form the Cs-oleate precursor solution. After 30 min, a N_2 flow was introduced into the flask and solution was kept under N_2 until all Cs_2CO_3 had completely dissolved in the solution and reacted with OA.

PbI_2 precursor: The PbI_2 precursor was formed by mixing 0.250 g PbI_2 (lead iodide) and 12.5 mL ODE in a three-neck flask and heated at 120 °C for 30 min under vacuum. While the solution was still under vacuum, 1.25 mL of preheated OA and 1.25 mL of preheated OA (oleylamine) were quickly injected into the PbI_2 solution. OA and OAm helped with dissolving PbI_2 quickly, making the previously turbid orange solution into transparent yellow.

Growth of $CsPbI_3$ nanocrystals: When the PbI_2 precursor was completely dissolved, N_2 flow was introduced into the flask heating it up to the desired temperature (140 – 220 °C). Then 1 mL of the Cs-oleate precursor was swiftly injected into the reaction flask. Within just a few seconds from the injection, the solution became turbid red. Further crystal growth and nucleation was stopped by immersing the reaction flask in an ice bath. After cooling to room temperature, $CsPbI_3$ NCs size-selective precipitation and purification was introduced. Methyl acetate (MeOAc) was added to the initial $CsPbI_3$ NCs solution in a volume ratio of 3:1 (NC solution/MeOAc). After centrifuging at 7500 rpm for 5 min, larger NCs were precipitated. The precipitate was collected and re-dispersed into 3 mL of *n*-hexane and supernatant was decanted for the next step (MeOAc) was added again in the same ratio. This second centrifugation produced another batch of NCs with a smaller size, compared to the first one. This same process was repeated until there was no obvious precipitate of NCs from the supernatant. The average number of batches from one synthesis was three. Some of the final solutions required one more centrifugation (without adding extra MeOAc) in order to discard supernatant which sometimes contained some bigger agglomerates or precursor crude leftovers. All solutions were filtered through a PVDF/L0.22 μm filter and then kept in a vial inside the fridge (5 °C). These solutions were stable for a month. For longer stability of the solutions, up to a few months, they were kept in a freezer (−21 °C).

Thin film deposition: $CsPbI_3$ NCs were first deposited as thin films prepared by spin coating the colloidal solution onto a glass substrate and drying it under N_2 flow multiple times, to ensure adequate substrate coverage. The spectra of the films at room temperature are nearly identical with the PL spectra of the NCs in solution, validating the success of the deposition procedure. Only deviation has been seen for the smallest, 7 nm, NCs.

X-ray diffraction (XRD)

Spin coated films of NCs on Si wafers were characterized by X-ray diffraction (XRD) using a BRUKER D8 ADVANCE with Bragg-Brentano geometry, Cu Kα radiation (λ = 1.54056 Å), step increment of 0.02° and 2 s of acquisition time. Pressure dependent XRD analysis on the 17 nm NCs were conducted on a Bruker APEX-II diffractometer equipped with sealed-tube and CCD detector, using Mo-Kα radiation (λ = 0.71073 Å). NC samples were

measured at room temperature. Specifically, the 17 nm NCs were loaded, in silicon oil, on a Diamond Anvil Cell (DAC) with diamond anvil type Ia and culet of 0.4 mm. The internal pressure was measured using the ruby fluorescence method [1]. The NCs-loaded DAC was mounted on a standard goniometer head and centered to the X-ray beam. The diffraction patterns at different pressures were collected on the CCD detector and the obtained two-dimensional ring patterns were integrated and converted to one dimensional powder profile using CrysAlis Pro program. Tested pressure: 0 GPa, 0.13 GPa, 1.85 GPa, 6.14 GPa.

Steady-state absorption and photoluminescence (PL)

Steady-state absorbance of perovskite solutions was measured in a quartz cuvette using a Shimadzu uv-2700 UV-vis spectrophotometer. PL of the same solutions was recorded using a NanoLog Fluorometer (Horiba Jobin-Yvon) with excitation at 450 nm and a 2 nm spectral resolution, using an iHR320 detector in the visible range.

Absolute photoluminescence quantum yield (PLQY)

Absolute values of PLQY were obtained from measurements performed in an integrating sphere (Labsphere). Excitation was provided by a 405 nm CW diode laser and spectra were acquired through an optical fiber coupled from the sphere to a spectrometer (Ocean Optics Maya Pro 2000) with an intensity of 10 mW. PLQY values were calculated employing the method proposed by de Mello et al. [55]

Temperature-dependent steady state absorption and photoluminescence

All temperature dependent measurements were performed under vacuum using a Linkam stage cooled with liquid nitrogen. Steady state absorption spectra were measured on perovskite thin films deposited on quartz using a UV-vis-NIR spectrophotometer (Lambda 1050, PerkinElmer). PL was excited using a 405 nm Oxxius laser focused on the sample with a 10 cm lens. PL was detected using a Maya1000 visible spectrometer.

Pressure-dependent measurements

All pressure-dependent measurements were performed on a diamond anvil cell (One20DAC) with diamond anvil type Ia and culet of 0.4 mm. A stainless steel gasket, with the pre-indented hole, was centered on one of the diamonds. The sample was loaded by drop casting several times and drying under a nitrogen flux between the depositions. When the sample was dried, a pressure marker (ruby powder) and pressure transmitting medium (silicon oil, 100cSt) were placed into the hole in the gasket. Silicon oil was applied as a pressure-transmitting medium in order to establish hydrostatic conditions. The pressure was measured by using the ruby fluorescence method[56]. With applying pressure ruby PL peaks are shifting toward longer wavelengths and by fitting peaks with Lorentzian profiles it is possible to determine the exact pressure[57]. The high-pressure evolution of steady-state PL spectra was collected using a micro Raman confocal microscope (*via* Raman Microscope Renishaw, 50× objective, 532 nm excitation wavelength).

Time-resolved PL (TRPL)

TRPL in the ps range was performed using a Hamamatsu streak camera and a Coherent Chameleon oscillator (pulse duration 30 fs, repetition rate 80 MHz) as a pump, using a pump wavelength λ = 400 nm obtained by frequency doubling the fundamental at 800 nm

42

in a BBO crystal. An acousto-optic modulator (AOT) was used to reduce the laser repetition rate to 2 MHz. The measurements were performed using a measurement window of 50 ns for pressures up to 1 GPa, and a 100 ns widow for higher pressure (respectively 0.5 ps and 1 ns temporal resolution). The sample was pressurized in a diamond anvil cell, in the previously described way, and light was focused on NCs clusters through a 50× long working distance microscope objective, ($r = 2$ μm), corresponding to a typical pump fluence of 150 mW/cm^2.

Transmission electron microscopy (TEM)

Transmission electron microscopy (TEM) for size distribution analysis was performed using a JEM-1400Plus (JEOL) equipped with a thermionic source (LaB6) and operated at 120 kV. Images were acquired by means of bright field-TEM technique. The samples contained colloidal suspensions of CsPbI$_3$ NCs (size ranging from 7 − 20 nm) which were used in the further experiments reported here. Specimens were prepared by drop casting 5 μL of additionally diluted solution in *n*-hexane (1:10 vol.) on the ultra-thin carbon film with Cu grid. Samples were dried 5-10 min at room temperature.

A statistic on NCs dimension was performed measuring the cube edge length of approximately 200 particles for each sample. The values were acquired manually with the help of Digital Micrograph software and collected in the histogram NCs average sizes match the expected values for 7, 10, and 11 nm samples, with a narrow size dispersion. The biggest NCs have an average size of 17 nm and a broader dispersion compared with the other samples.

2.5. References

1. Protesescu, L. *et al.* Nanocrystals of Cesium Lead Halide Perovskites (CsPbX$_3$, X = Cl, Br, and I): Novel Optoelectronic Materials Showing Bright Emission with Wide Color Gamut. *Nano Lett.* **15**, 3692–3696 (2015).

2. Huang, H. *et al.* Growth mechanism of strongly emitting CH$_3$NH$_3$PbBr$_3$ perovskite nanocrystals with a tunable bandgap. *Nat. Commun.* **8**, 996 (2017).

3. Fu, Y. *et al.* Metal halide perovskite nanostructures for optoelectronic applications and the study of physical properties. *Nat. Rev. Mater.* **4**, 169–188 (2019).

4. Stranks, S. D. & Snaith, H. J. Metal-halide perovskites for photovoltaic and light-emitting devices. *Nat. Nanotechnol.* **10**, 391–402 (2015).

5. Liu, D. *et al.* Metal halide perovskite nanocrystals: Application in high-performance photodetectors. *Mater. Adv.* **2**, 856–879 (2021).

6. Masuda, T. *et al.* All-inorganic cesium lead halide perovskite nanocrystals for solar-pumped laser application. *J. Appl. Phys.* **127**, 243104 (2020).

7. Beimborn, J. C., Walther, L. R., Wilson, K. D. & Weber, J. M. Size-Dependent Pressure-Response of the Photoluminescence of CsPbBr$_3$ Nanocrystals. *J. Phys. Chem. Lett.* **11**, 1975–1980 (2020).

8. Aoyagi, S., Kuroiwa, Y., Sawada, A., Kawaji, H. & Atake, T. Size effect on crystal

structure and chemical bonding nature in BaTiO$_3$ nanopowder. *J. Therm. Anal. Calorim.* **81**, 627–630 (2005).

9.   Zhang, L., Wang, K., Lin, Y. & Zou, B. Pressure Effects on the Electronic and Optical Properties in Low-Dimensional Metal Halide Perovskites. *J. Phys. Chem. Lett.* **11**, 4693–4701 (2020).

10. Beimborn, J. C., Hall, L. M. G., Tongying, P., Dukovic, G. & Weber, J. M. Pressure Response of Photoluminescence in Cesium Lead Iodide Perovskite Nanocrystals. *J. Phys. Chem. C* **122**, 11024–11030 (2018).

11. Cortecchia, D. *et al.* Structure-controlled optical thermoresponse in Ruddlesden-Popper layered perovskites. *APL Mater.* **6**, 114207 (2018).

12. Cortecchia, D. *et al.* Broadband emission in two-dimensional hybrid perovskites: The role of structural deformation. *J. Am. Chem. Soc.* **139**, 39–42 (2017).

13. Zhao, Q. *et al.* Size-Dependent Lattice Structure and Confinement Properties in CsPbI$_3$ Perovskite Nanocrystals: Negative Surface Energy for Stabilization. *ACS Energy Lett.* **5**, 238–247 (2020).

14. Ke, F. *et al.* Preserving a robust CsPbI$_3$ perovskite phase via pressure-directed octahedral tilt. *Nat. Commun.* **12**, 461 (2021).

15. Cao, Y. *et al.* Pressure-Tailored Band Gap Engineering and Structure Evolution of Cubic Cesium Lead Iodide Perovskite Nanocrystals. *J. Phys. Chem. C* **122**, 9332–9338 (2018).

16. Swarnkar, A. *et al.* Quantum dot-induced phase stabilization of α-CsPbI$_3$ perovskite for high-efficiency photovoltaics. *Science.* **354**, 92–95 (2016).

17. Xiao, G. *et al.* Pressure Effects on Structure and Optical Properties in Cesium Lead Bromide Perovskite Nanocrystals. *J. Am. Chem. Soc.* **139**, 10087–10094 (2017).

18. Wang, L., Wang, K., Xiao, G., Zeng, Q. & Zou, B. Pressure-Induced Structural Evolution and Band Gap Shifts of Organometal Halide Perovskite-Based Methylammonium Lead Chloride. *J. Phys. Chem. Lett.* **7**, 5273–5279 (2016).

19. Lee, J.-H., Jaffe, A., Lin, Y., Karunadasa, H. I. & Neaton, J. B. Origins of the Pressure-Induced Phase Transition and Metallization in the Halide Perovskite (CH$_3$NH$_3$)PbI$_3$. *ACS Energy Lett.* **5**, 2174–2181 (2020).

20. Liang, Y. *et al.* New Metallic Ordered Phase of Perovskite CsPbI$_3$ under Pressure. *Adv. Funct. Mater.* **6**, 1900399 (2019).

21. Iaru, C. M., Geuchies, J. J., Koenraad, P. M., Vanmaekelbergh, D. & Silov, A. Y. Strong Carrier-Phonon Coupling in Lead Halide Perovskite Nanocrystals. *ACS Nano* **11**, 11024–11030 (2017).

22. Diroll, B. T., Zhou, H. & Schaller, R. D. Low-Temperature Absorption, Photoluminescence, and Lifetime of CsPbX$_3$ (X = Cl, Br, I) Nanocrystals. *Adv. Funct. Mater.* **28**, 1–7 (2018).

23. Lee, S. M. *et al.* Temperature-Dependent Photoluminescence of Cesium Lead Halide Perovskite Quantum Dots: Splitting of the Photoluminescence Peaks of

44

CsPbBr$_3$ and CsPb(Br/I)$_3$ Quantum Dots at Low Temperature. *J. Phys. Chem. C* **121**, 26054–26062 (2017).

24. Saran, R., Heuer-Jungemann, A., Kanaras, A. G. & Curry, R. J. Giant Bandgap Renormalization and Exciton–Phonon Scattering in Perovskite Nanocrystals. *Adv. Opt. Mater.* **5**, 1–9 (2017).

25. Zhang, X. Y., Pang, G. T., Xing, G. C. & Chen, R. Temperature dependent optical characteristics of all-inorganic CsPbBr$_3$ nanocrystals film. *Mater. Today Phys.* **15**, 100259 (2020).

26. Liu, A. *et al.* Effect of dimensionality on the optical absorption properties of CsPbI$_3$ perovskite nanocrystals. *J. Chem. Phys.* **151**, 191103 (2019).

27. Yesudhas, S. *et al.* Pressure-Induced Phase Changes in Cesium Lead Bromide Perovskite Nanocrystals with and without Ruddlesden-Popper Faults. *Chem. Mater.* **32**, 785–794 (2020).

28. Lü, X., Yang, W., Jia, Q. & Xu, H. Pressure-induced dramatic changes in organic-inorganic halide perovskites. *Chem. Sci.* **8**, 6764–6776 (2017).

29. Mao, H. K. *et al.* Recent advances in high-pressure science and technology. *Matter Radiat. Extrem.* **1**, 59–75 (2016).

30. Liang, Y. *et al.* New Metallic Ordered Phase of Perovskite CsPbI$_3$ under Pressure. *Adv. Sci.* **6**, 1900399 (2019).

31. Shen, Y., Kumar, R. S., Pravica, M. & Nicol, M. F. Characteristics of silicone fluid as a pressure transmitting medium in diamond anvil cells. *Rev. Sci. Instrum.* **75**, 4450–4454 (2004).

32. Ha, S. T., Su, R., Xing, J., Zhang, Q. & Xiong, Q. Metal halide perovskite nanomaterials: synthesis and applications. *Chem. Sci.* **8**, 2522–2536 (2017).

33. Tovstun, S. A. & Razumov, V. F. Theory of size-selective precipitation. *J. Nanoparticle Res.* **19**, 11051 (2017).

34. Beimborn, J. C., Hall, L. M. G., Tongying, P., Dukovic, G. & Weber, J. M. Pressure Response of Photoluminescence in Cesium Lead Iodide Perovskite Nanocrystals. *J. Phys. Chem. C* **122**, 11024–11030 (2018).

35. Treglia, A. *et al.* Effect of electronic doping and traps on carrier dynamics in tin halide perovskites. *Mater. horizons* **9**, 1763–1773 (2022).

36. Lee, Koteles & Vassell. Luminiscence linewidths of excitons in GaAs QW below 150 K. *Phys. Rev. A* **33**, 5512 (1986).

37. Zhang, X. B., Taliercio, T., Kolliakos, S. & Lefebvre, P. Influence of electron-phonon interaction on the optical properties of III nitride semiconductors. *J. Phys. Condens. Matter* **13**, 7053–7074 (2001).

38. S Rudin, TL Reinecke, B. S. Temperature-dependent exciton linewidths in semiconductors. *Phys. Rev. B. Condens. Matter* **42**, 218–231 (1990).

39. Saran, R., Heuer-Jungemann, A., Kanaras, A. G. & Curry, R. J. Giant Bandgap Renormalization and Exciton–Phonon Scattering in Perovskite Nanocrystals. *Adv.*

Opt. Mater. **5**, 1–18 (2017).

40. Ruppin, R. Surface effects on optical phonons and on phonon-plasmon modes. *Surf. Sci.* **34**, 20–32 (1973).

41. Folpini, G. *et al.* Strong Local-Field Enhancement of the Nonlinear Soft-Mode Response in a Molecular Crystal. *Phys. Rev. Lett.* **119**, 097404 (2017).

42. Wei, K. *et al.* Temperature-dependent excitonic photoluminescence excited by two-photon absorption in perovskite $CsPbBr_3$ quantum dots. *Opt. Lett.* **41**, 3821 (2016).

43. Bouarissa, N. Phonon confinement in nanostructured InP. *J. Comput. Theor. Nanosci.* **10**, 1284–1289 (2013).

44. Li, S., Liu, G., Liu, Q., Nie, L. & Yao, G. Ultrastable Zero-Dimensional Cs_4PbBr_6 Perovskite Quantum Dot Glass. *ACS Sustain. Chem. Eng.* **8**, 10646–10652 (2020).

45. Yazdani, N., Volk, S., Yarema, O., Yarema, M. & Wood, V. Size, Ligand, and Defect-Dependent Electron − Phonon Coupling in Chalcogenide and Perovskite Nanocrystals and Its Impact on Luminescence Line Widths. *ACS Photonics* **7**, 1088–1095 (2020).

46. Shamsi, J., Urban, A. S., Imran, M., De Trizio, L. & Manna, L. Metal Halide Perovskite Nanocrystals: Synthesis, Post-Synthesis Modifications, and Their Optical Properties. *Chem. Rev.* **119**, 3296–3348 (2019).

47. Wang, Y. *et al.* Pressure-Induced Phase Transformation, Reversible Amorphization, and Anomalous Visible Light Response in Organolead Bromide Perovskite. *J. Am. Chem. Soc.* **137**, 11144–11149 (2015).

48. Tolbert, S. H. & Alivisatos, A. P. High-pressure structural transformations in semiconductor nanocrystals. *Annu. Rev. Phys. Chem.* **46**, 595–625 (1995).

49. Kong, L. *et al.* Simultaneous band-gap narrowing and carrier-lifetime prolongation of organic-inorganic trihalide perovskites. *Proc. Natl. Acad. Sci. U. S. A.* **113**, 8910–8915 (2016).

50. Beimborn, J. C., Walther, L. R., Wilson, K. D. & Weber, J. M. Size-Dependent Pressure-Response of the Photoluminescence of $CsPbBr_3$ Nanocrystals. *J. Phys. Chem. Lett.* **11**, 1975–1980 (2020).

51. Sivalertporn, K., Mouchliadis, L., Ivanov, A. L., Philp, R. & Muljarov, E. A. Direct and indirect excitons in semiconductor coupled quantum wells in an applied electric field. *Phys. Rev. B - Condens. Matter Mater. Phys.* **85**, 045207 (2012).

52. Alexandrou, A. *et al.* Electric-field effects on exciton lifetimes in symmetric coupled $GaAs/Al_{0.3}Ga_{0.7}As$ double quantum wells. *Phys. Rev. B* **42**, 9225–9228 (1990).

53. Chow, W., Kira, M. & Koch, S. W. Microscopic theory of optical nonlinearities and spontaneous emission lifetime in group-III nitride quantum wells. *Phys. Rev. B - Condens. Matter Mater. Phys.* **60**, 1947–1952 (1999).

54. Wright, A. D. *et al.* Electron–phonon coupling in hybrid lead halide perovskites. *Nat. Commun.* **7**, 11755 (2016).

46

55. De Mello, J. C., Wittmann, H. F. & Friend, R. H. An improved experimental determination of external photoluminescence quantum efficiency. *Adv. Mater.* **9**, 230–232 (1997).

56. Mao, H. K., Xu, J. & Bell, P. M. Calibration of the ruby pressure gauge to 800 kbar under quasi-hydrostatic conditions. *J. Geophys. Res.* **91**, 4673 (1986).

57. Syassen, K. Ruby under pressure. *High Press. Res.* **28**, 75–126 (2008).

3

CsPbBr$_3$ nanocrystals for perovskite solar cells

Abstract

Cesium lead tribromide (CsPbBr$_3$) perovskite nanocrystals (NCs) are synthesized using the hot-injection (HI) and ligand-assisted re-precipitation (LARP) methods. HI yields highly stable colloidal NCs solutions but the long organic ligands are less favorable for producing thin films that are suitable for solar cell applications as they are easily wiped off or removed by solvents. LARP also yields monodisperse dispersions of CsPbBr$_3$ NCs, but solutions are less stable because the NCs tend to agglomerate due to the shorter organic ligands used. Using the LARP method, thin films are easier to prepare because multiple layers can be sequentially deposited. The CsPbBr$_3$ NCs are incorporated in two different solar cell configurations. First, they are used as wide-bandgap thin film absorbers in planar *n–i–p* solar cells. The power conversion efficiency (PCE) of these cells is 2.7%, and while the devices provide a considerable open-circuit voltage, they lack short-circuit current. Secondly, CsPbBr$_3$ NCs are employed to passivate the titania electron transport layer in mesoporous *n–i–p* solar cells that use methyl ammonium lead triiodide (MAPI) as absorber and a carbon-based electrode. Solar cells with CsPbBr$_3$ passivation layers have a PCE of 13.6%, which is 10% higher compared to the same devices without passivation.

3.1. Introduction

Cesium lead tribromide ($CsPbBr_3$) perovskite nanocrystals (NCs) are direct wide-bandgap semiconductors with a strong ionic nature and weak internal chemical bonding[1]. The ionic nature results in a low energy barrier for formation, facile ion exchange, and solubility in polar solvents, while the weak ionic bonding results in easy low-temperature synthesis. Their photophysical characteristics such as visible photoluminescence (PL) and high photoluminescence quantum yield (PLQY), and primary optoelectronic properties, such as direct and size-tunable bandgap, rather low charge recombination rates and high carrier mobility, make $CsPbBr_3$ NCs an interesting wide-bandgap semiconductor for different applications, such as lasers, photodiodes, and light-emitting diodes. $CsPbBr_3$ NCs are also suitable for solar cells.

CsPbBr_3 NCs can be synthesized from widely available chemical compounds, which makes them attractive for larger scale production and use. The two most common liquid-phase methods to synthesize colloidal perovskite NCs are the hot-injection (HI) method and the ligand-assisted re-precipitation (LARP) method. Both methods use two separately prepared precursor solutions, one containing cesium cations and another with lead bromide ($PbBr_2$) and appropriate organic carboxylic acid and organic primary amines as coordinating ligands. Mixing these solutions triggers nucleation and growth of NCs. HI requires a controlled atmosphere (nitrogen or argon flow), elevated temperature, and is accomplished by injection of a hot cesium-oleate solution into a hot solution of $PbBr_2$, together with long organic coordinating ligands. In the LARP process, colloidal $CsPbBr_3$ NCs are prepared at room temperature under ambient conditions by injecting a cesium propionate solution and a solution of $PbBr_2$, with short organic ligands, into a mixture of polar and non-polar solvents.

The formation of $CsPbBr_3$ perovskite NCs is an extremely fast reaction, usually completed within 1 to 5 s. Because of the fast kinetics, understanding the crystal growth in all inorganic $CsPbBr_3$ perovskite NCs is still a relatively unexplored field. Li et al.[2] "slowed down" the reaction rate with a kind of microwave-assisted synthesis and proposed the model for $CsPbBr_3$ NCs formation mechanism. The crystal growth starts with $[PbBr_6]^{4-}$ octahedrals which form a framework structure that is gradually stabilized by Cs^+ ions filling some of the interstitial voids. When the first single-species nuclei are formed, they subsequently grow into larger particles. The growth mechanism of NCs starts with LaMer nucleation, followed by Ostwald ripening, coalescence, and intraparticle growth[3]. According to a study by Koolyk et al.,[4] the growth of $CsPbBr_3$ NCs is characterized by size de-focusing, i.e., an increase of the full width at half maximum (FWHM) of the size distribution, from the beginning of the growth.

CsPbBr_3 NCs can be formed with different morphologies, including nanocubes, nanowires, nanospheres, nanorods, nanoplates, two-dimensional

nanosheets, etcetera. Cube-shaped $CsPbBr_3$ NCs are the most common morphology[2]. The shape of the NCs can be controlled by varying the relative amounts of ligands, by using different poor polar solvents, and by the reaction time. Surface ligands, used during the synthesis to dissolve precursors, provide elimination or passivation of surface defects, and increase PLQY and stability. However, at the same time, organic ligands create an insulating shell against charge injection or extraction. In fact, the organic and insulating nature of the ligands is a significant obstacle for charge transport between NCs and must be addressed in the fabrication of optoelectronic NCs devices[5]. Besides the choice of appropriate ligands, the purification process of NCs solutions is possibly even more important. Before purification, ligands are present in the solution and bound to the NCs surface. When the ligands are removed from the solution during purification, the surface capping ligands can also be removed because the ionic nature of the $CsPbBr_3$ NCs makes that bonds with the ligands are rather labile. Hence, the presence of an excess of primary amines in the solution, after purification, can result in a high PLQY. On the other hand, the presence of excess amines, because of their insulating nature, can have a negative effect on the active layer in solar cells[6].

$CsPbBr_3$ NCs are in the cubic crystal structure at higher temperature (HI method)[7] and in an orthorhombic phase at lower reaction temperatures (for HI) or room temperature (LARP method)[6]. Brennan et al. suggest the dependence of $CsPbBr_3$ crystal structure on size, since their study showed that very small particles (5 nm) are exclusively cubic, while larger particles (in their study with a size of 10 nm) show coexistence of cubic and orthorhombic phases[8].

$CsPbBr_3$ NCs can be re-dispersed in common low-boiling point organic solvents such as *n*-hexane or toluene. The hydrophobic nature of the solvents used to disperse these particles makes them interesting for application in multi-junction solar cells. Multi-junction solar cells require two or more perovskite films, separated by appropriate charge transport layers. Presently, the way to process the second perovskite film without harming the first is the use of a solvent barrier layer that protects the first layer from the polar, high-boiling point, slowly evaporating solvents used to process the second perovskite film. These barrier layers often consist of atomic layer deposited or sputtered metal oxides, which cannot be deposited by solution or ink-based techniques. Perovskite formulations based on non-polar, low-boiling point, volatile solvents such as toluene, *n*-hexane, or similar, will open a route to new and simplified device layouts, because the evaporation rate of the solvent is a crucial parameter when multiple layers are deposited on top of each other, as required for making multi-junction solar cells. The important benefit of using $CsPbBr_3$ NCs in multi-junction solar cells is that their wide-bandgap can open the possibility to reach a high open-circuit voltage (V_{OC}), which is the main aspect of the higher efficiency of multi-junction solar cells. To get to the point of using $CsPbBr_3$ NCs in multi-junction solar cells, single junction first needs to be optimized.

This chapter describes the preparation and characterization of CsPbBr$_3$ NCs solutions and films and their use in solar cells. CsPbBr$_3$ NCs are used as a photoactive layer in planar n–i–p wide-bandgap solar cells and as a passivation layer to enhance the open-circuit voltage (V_{OC}) of mesoporous n–i–p solar cells that use methylammonium lead triiodide (MAPI) as absorber layer.

3.2. Results

3.2.1. Hot-injection method - solution and film characterization

The HI method for CsPbBr$_3$ NCs was first presented by Protesescu et al.[7]. Briefly, a cesium oleate solution is swiftly injected in a hot solution (140 to 200 °C) of 1-octadecene (ODE), PbBr$_2$, a carboxylic acid (mostly oleic acid, OA), and a primary amine (mostly oleylamine, OAm). The solutions are kept under nitrogen flow during the reaction. The formation reaction of CsPbBr$_3$ NCs *via* the HI method is:

$$2\ Cs(C_{17}H_{33}COO)_2 + 3\ PbBr_2 \rightarrow 2\ CsPbBr_3 + Pb(C_{17}H_{33}COO)_2 \qquad (1)$$

NCs formation is an extremely fast reaction, usually completed within 1 to 5 s. The crystallization is stopped by immersing the reaction flask into an ice bath. The HI method enables the synthesis of small NCs with a narrow size distribution. The key parameters to control the shape and size of as-synthesized NCs are the temperature, the concentration of the precursors, the ratio between surfactant and precursor, and the duration of the reaction. By varying the ratio of the OA and OAm ligands, while keeping the temperature constant, it is possible to the tune the shape and size of the NCs[9]. Also, by keeping the ratio between ligands the same but changing temperature, it is possible to obtain different morphologies. Here, the focus is on the formation of CsPbBr$_3$ nanocube morphologies.

NCs made this way were re-dispersed in toluene. The solution is green, highly fluorescent, and does not precipitate over time or degrade when exposed to the ambient atmosphere (**Figure 3.1.a**). The PL emission peak is around 520 nm when measured with excitation at 400 nm. The PLQY determined relative to rhodamine 6G is 45%. Transmission electron microscopy (TEM) images (**Figure 3.1.b**) show nicely organized NCs, but also indicate the presence of NCs morphologies that deviate from the cubic shape. Instead of having equal sides, some particles have one side elongated and the other shortened. This morphology is known as nanoplates.
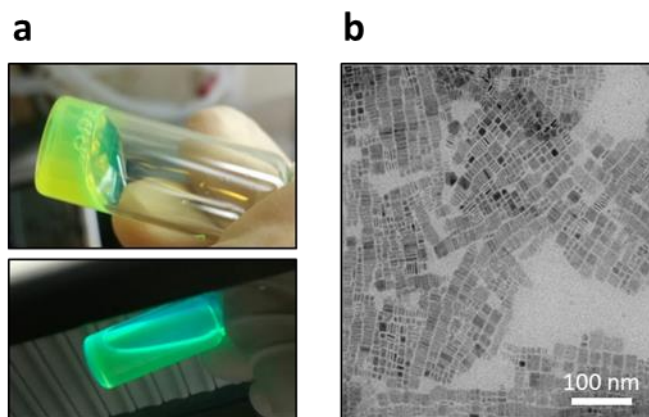
Figure 3.1. CsPbBr₃ NCs solutions made with HI. a) In daylight the solution is green (top photo), does not precipitate over time nor degrade when exposed to ambient atmosphere, and is highly fluorescent under the UV light (bottom photo). **b)** TEM image of NCs obtained with the HI method.

Films were made by spin coating the CsPbBr₃ NCs solution in ambient atmosphere (1000 rpm for 45 s). Aside from the main peak observed around 520 nm of the NCs, the films show additional smaller PL peaks at 460 and 475 nm. The additional peaks are attributed to PL from nanoplates.

To avoid pinholes and cracks in the films and to achieve a reasonable film thickness, multiple layers must be deposited on top of each other. **Figure 3.2.a** presents a comparison of the PL spectra for films with one and with five sequential depositions. Depositing more layers on top of each other does not improve the PL intensity. In contrast, after depositing five layers, the PL intensity decreased (**Figure 3.2.a**). Probably, with every new spin coating cycle, some of the previously deposited material was removed such that film thickness did not improve.

Both problems, the pronounced undesired additional blue-emitting component and the decrease in PL emission with multiple depositions, can be reduced or eliminated by introducing a washing step after every deposition step to remove the organic ligands. This is accomplished by spin coating a lead nitrate (Pb(NO₃)₂) solution in methyl acetate on top of the deposited layer[10]. After five sequential deposition and washing steps, the PL spectrum shows an enhanced intensity and a single peak around 520 nm and no signals in the blue spectral region (**Figure 3.2.b**). Films made in this way are on average thinner than 200 nm, which limits their use in photovoltaic devices.

a

b
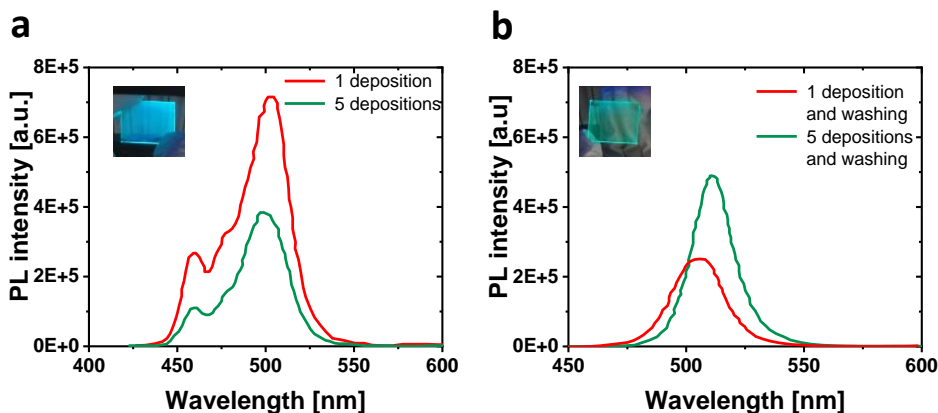
**Figure 3.2. PL spectra and images of CsPbBr₃ NCs layers made *via* the HI method.
a)** Comparison of single deposition and five sequential depositions without washing. **b)**
Same bust with washing ligands using Pb(NO₃)₂ in methyl acetate after each deposition
step.

3.2.2. Ligand-assisted re-precipitation - solution and film characterization

Unlike the HI method, the LARP method does not require elevated temperatures or a controlled atmosphere. The cesium precursor solution is made by dissolving cesium carbonate (Cs_2CO_3) in propionic acid. The second precursor solution is made by dissolving $PbBr_2$ in a mixture of butylamine, propionic acid, and 2-propanol. The order of solvents is important, and it should be used in this order. After stirring for a few hours to completely dissolve the components, the cesium propionate solution is added to a mixture of *n*-hexane and 2-propanol (2:1 v/v). Directly after that the $PbBr_2$ precursor solution is injected, while stirring. The formation reaction of CsPbBr₃ NCs *via* the LARP method is:

$$2\ Cs(C_2H_5COO)_2 + 3\ PbBr_2 \rightarrow 2\ CsPbBr_3 + Pb(C_2H_5COO)_2 \qquad (2)$$

 Purification is done by centrifugation and NCs were re-dispersed in toluene.

        When following the procedure reported by Akkerman et al.[11], the solution was turbid and looked greenish-yellow, strongly fluorescent, and showed a PL peak around 525 nm, when measured with excitation at 400 nm. However, solutions show fast, within minutes, precipitation of CsPbBr₃ NCs. Likely because of the short-chain organic ligands, the particles tend to stick to each other, agglomerate, and subsequently precipitate. The measured PLQY is up to 20%, significantly lower than the PLQY achieved *via* the HI method. NCs have a tendency to stick to the glass of vials and pipettes, which makes tracking concentration hard. TEM revealed that solutions contain nanocubes in a size range between 10 and 20 nm.

54

Substantial improvement was achieved by using anhydrous solvents, doubling the concentration of the cesium propionate solution, and reducing the centrifugation rates. Dispersions made this way, were more stable and gave higher PLQY. After purification, the NCs morphology was retained. It is interesting that up-scaling the process made the solutions more resistant to precipitation. The optimized solutions are greenish yellow, strongly fluorescent with a PL peak at 525 nm when measured with excitation at 400 nm (**Figure 3.3.a** and **Figure 3.3.b**), and an improved average PLQY of around 30%. TEM images of $CsPbBr_3$ crystals made *via* the optimized LARP method revealed that the solutions contain nanocubes in a size range of 10 to 20 nm, without unwanted morphologies (**Figure 3.3.c**).

a

b **c**
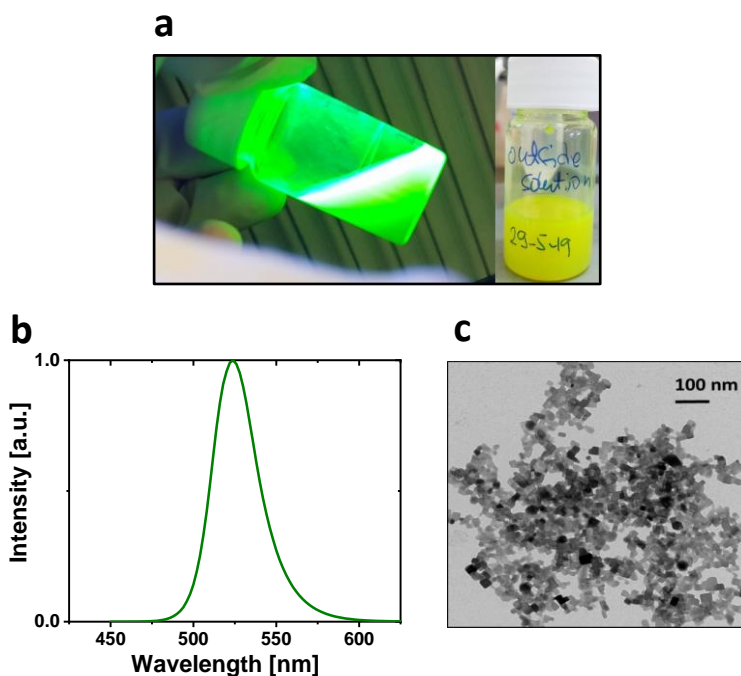
Figure 3.3. CsPbBr₃ NCs solutions made with LARP. a) In daylight the solution is greenish yellow (right photo) and is highly fluorescent under the UV light (left photo). **b)** PL spectrum. **c)** TEM image of the NCs obtained with LARP.

Thin single-layer films prepared directly from colloidal $CsPbBr_3$ solutions *via* spin coating, resulted in hazy and rough layers as seen by scanning electron microscopy (SEM) (**Figure 3.4.a**). Atomic force microscopy (AFM) revealed that the surface is only partly covered with NCs resulting in an average surface roughness of 30 nm (**Figure 3.4.b**). The X-ray diffraction (XRD) pattern indicates that $CsPbBr_3$ NCs were formed in the orthorhombic phase (**Figure 3.4.c**). Hazy,

too thin, and incomplete covered layers are not desirable in photovoltaic devices since they reduce absorption of light and cause shorts.

Contrary to spin coating multiple layers from NCs solutions made *via* HI, solutions made with the LARP method allow depositing additional material to the stack in each subsequent spin coating step. This is important for fabricating devices, because is not possible to achieve sufficient active layer thickness in one spin coating cycle. **Figure 3.4.d** presents the absorption spectra of films with 1 to 10 spin coating cycles. Every layer was spin coated at 1000 rpm for 45 s and dried for 5 min between depositions. The absorbance increases almost linearly with the number of steps, only small deviations have been observed.
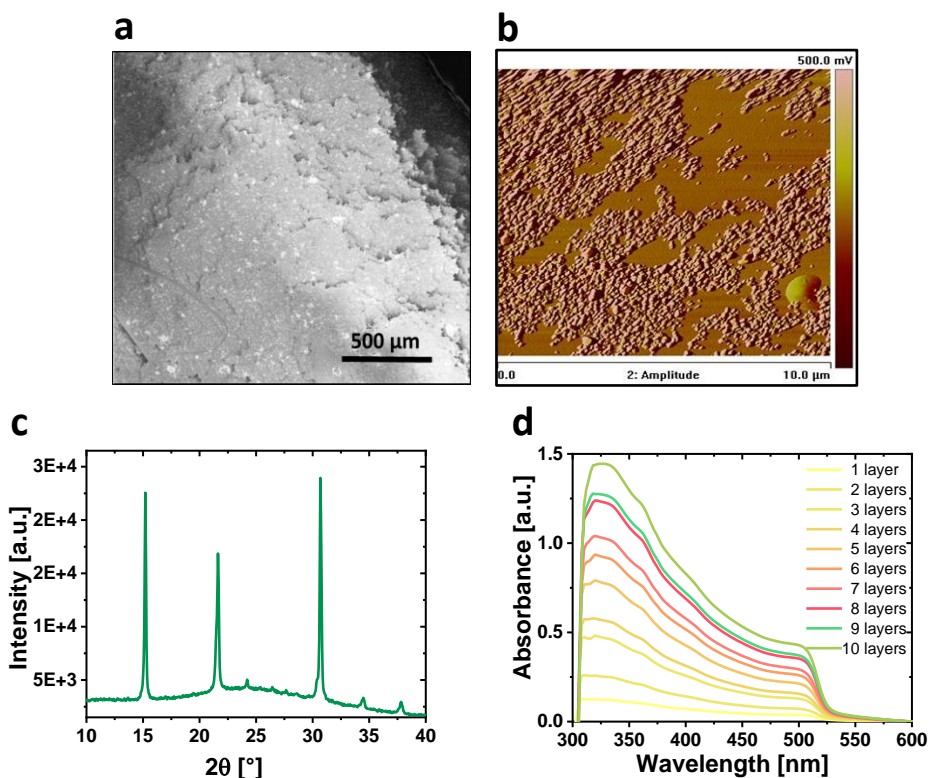
Figure 3.4. Characterization of thin film CsPbBr₃ NCs synthesized *via* LARP. a) SEM image shows a hazy and rough layer. **b)** AFM image reveals that the surface is only partly covered with the NCs. **c)** XRD pattern indicates that CsPbBr₃ NCs are in the orthorhombic phase. **d)** Absorption spectra of 1 to 10 layer depositions show a linear increase of absorbance with the number of deposition steps.

The main advantage of the LARP method is that multilayers can be easily made and that the ligands can be removed by simple drying or annealing. With this procedure it is possible to make thick enough active layers for a functional

56

solar cell. In addition, the amount of material that can be made in the LARP procedure is higher than *via* the HI method. These were the main reasons for using the LARP method to obtain $CsPbBr_3$ NCs for application in single-junction photovoltaic cells.

3.2.3. Planar CsPbBr₃ NCs *n–i–p* solar cells

$CsPbBr_3$ NCs solar cells were prepared in a *n–i–p* configuration. Briefly, on patterned indium tin oxide (ITO) covered glass substrates, a tin oxide (SnO_2) film was deposited as electron transport layer (ETL). The $CsPbBr_3$ NCs made *via* the LARP method were spin coated from the colloidal solution. As hole transport layer (HTL) a doped 2,2′,7,7′-tetrakis(*N*,*N*-di(4-methoxyphenyl)amino)-9,9′-spirobifluorene (spiro-OMeTAD) layer was used. To finish the device, Au was thermally evaporated under a high vacuum as a top electrode.

The $CsPbBr_3$ NCs absorber layer was deposited in ambient conditions, usually in 10 consecutive depositions. Each deposition was followed by thermal annealing. The effect of thermal annealing on the photoactive layer was investigated by measuring the UV-vis absorption spectra of layers on glass substrates annealed at temperatures in the range of 100 to 200 °C. **Figure 3.5.a** shows that thermal annealing results in an increase and narrowing of the excitonic peak in the visible region at the onset of absorption spectra together with a small red shift.

The impact of thermal annealing on the device performance is summarized in **Table 3.1.**, which shows the open-circuit voltage (V_{OC}), short-circuit current density (J_{SC}), fill factor (FF), and maximum power output (P_{max}) of the solar cells. The measurements were performed under simulated solar light (AM1.5G) and recorded in fast downward scans. Compared to drying in air at room temperature, thermal annealing enhances the device performance. P_{max} improves with increasing temperature up to 200 °C but drops for higher temperatures, possibly due to decomposition of the perovskite. The annealing time, either 15 or 30 min, had no significant effect on performance levels. The most pronounced increase is found for J_{SC}, while trends for V_{OC} and FF with temperature are less clear. Because the difference between the annealing temperature of 175 °C and 200 °C is negligible, 175 °C was chosen and used as the annealing temperature for further experiments.

Because the boiling point of the short-chain ligands used in the LARP method is lower than 175 °C, we expect that thermal annealing results in evaporation of ligands from the film. To evaluate if this was indeed the case, we introduced a washing step with $Pb(NO_3)_2$ after depositing the nanoparticles, but the performance did not improve. This shows that thermal annealing is sufficient to remove the ligands.

Table 3.1. Effect of annealing temperature on the photovoltaic performance of CsPbBr$_3$ NCs solar cells. Parameters were recorded in fast downward scans. All samples have 10 sequential layer depositions.

	V_{OC}(V)	J_{SC} (mA/cm^2)	FF	P_{max} (mW/cm^2)
Drying	1.12	1.31	0.75	1.09
100 °C	1.25	1.65	0.56	1.14
150 °C	1.10	1.67	0.74	1.36
175 °C	1.21	2.24	0.63	1.72
200 °C	1.25	2.41	0.59	1.79
225 °C	1.09	1.90	0.63	1.32

To reach sufficient optical absorption, multiple CsPbBr$_3$ NCs layers have to be deposited on top of each other, during several spin coating cycles. **Table 3.2.** shows that with an increasing number of layers J_{SC} continuously increases. This is ascribed to the increased absorption of light and the associated increased charge generation. The trend in V_{OC} is less clear and variations may be due to a different number of occasional pinholes in the generally rough films that reduce the V_{OC} by creating shunt paths. The FF slightly drops with the number of layers, which is in accordance with an increased charge recombination relative to charge collection for thicker layers. Using more concentrated solutions and very low spin coating rates, the number of deposition cycles can be reduced. However, the increased concentration increases the viscosity which can hamper spin coating.

Table 3.2. Effect of the number of deposition cycles on the photovoltaic performance of CsPbBr$_3$ NCs solar cells. Parameters were recorded in fast downward scans.

Number of depositions	V_{OC}(V)	J_{SC} (mA/cm^2)	FF	P_{max} (mW/cm^2)
5	1.04	1.81	0.63	1.18
10	1.21	2.24	0.63	1.72
15	1.23	2.55	0.60	1.90
20	1.30	3.21	0.60	2.44
30	1.17	3.80	0.61	2.70

Figure 3.5.b shows the current density – voltage (*J-V*) characteristics measured in a fast downward sweep of CsPbBr$_3$ NCs solar cells made with 20 depositions and annealing at 175 °C. Several shortcomings are evident. First, the inverse slope of the *J-V* curve around V_{OC} of about 125 Ω/cm^2 reveals a high series resistance. Second, the minimum at *V* = 0.7 V hints at a relatively large hysteresis in the cells. Although the V_{OC} of 1.3 V is relatively high, it should be noted that the minimal photon energy loss, defined as the energy difference between the optical bandgap (E_g) and qV_{OC} is 2.38 − 1.30 = 1.08 eV, which is large.
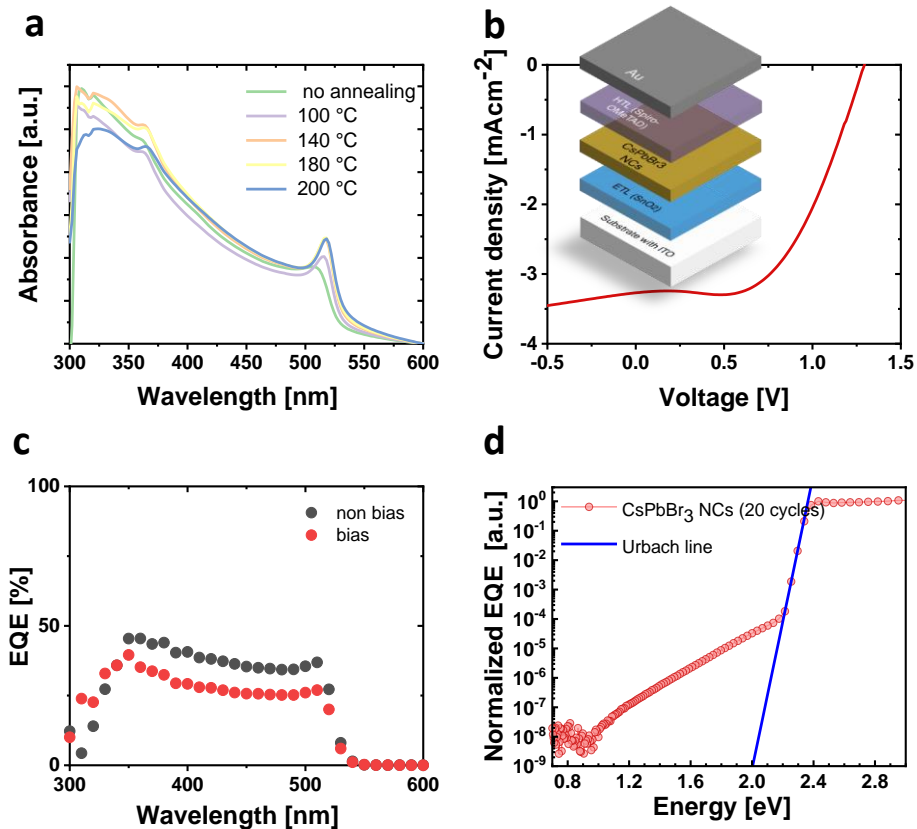
Figure 3.5. Solar cells with CsPbBr$_3$ NCs as a photoactive layer. a) Absorption spectra for films showing an effect of annealing temperature. **b)** *J-V* curve. The device configuration is presented in the inset. **c)** EQE measured without (black markers) and with bias light (red markers). **d)** Sub-bandgap EQE showing an Urbach energy of 17 meV and a significant sub-bandgap signal that originates from defects in the film or at the interface layers.

Figure 3.5.c shows the external quantum efficiency (EQE) of the cells measured without and with a light bias equivalent to 1 sun illumination. There is a

considerable decrease in EQE under light bias by about 10%. In the blue region a more charges are extracted, and current generation drops in the visible range. Devices can extract up to 50% of incident photons.

To characterize the solar cells in more detail sub-bandgap EQE measurements were performed. In these measurements, the EQE is measured sensitively over a wide range of photon energies. **Figure 3.5.d** shows an exponential decrease in EQE just below the bandgap. The Urbach energy (E_U), determined from the slope is 17 meV. E_U is a measure of energetic disorder. The value of 17 meV is typical for $CsPbBr_3$ perovskite layers at room temperature[12]. Below the Urbach tail the EQE shows a considerable response. This implies the presence of a significant number of defects.

Changing different parameters such as concentration, ligand washing, annealing time, spin coating speed, and the number of deposited layers, resulted in a reproducible device with relatively high $V_{OC} = 1.31$ V, but moderate $J_{SC} = 3.5$ mA/cm^2 and FF = 0.59, resulting in $P_{max} = 2.7$ mW/cm^2.

3.2.4. Mesoporous HTL-free *n–i–p* solar cells using CsPbBr$_3$ NCs

One of the most stable architectures for perovskite solar cells, which does not require fabricating thin films, or the use of expensive materials, is a multi-layer screen-printed mesoporous stack with a carbon top electrode. Fabrication of such a cell involves spraying a compact TiO_2 (c-TiO_2) on a glass substrate with a fluorinated tin oxide (FTO) electrode to create a closed contact layer. Next, a mesoporous TiO_2 (m-TiO_2) ETL is deposited on top *via* screen printing. The cells do not use a HTL but employ a carbon top electrode in direct contact with the perovskite active layer. Carbon is an appealing substitute for expensive electrodes, such as Au, commonly used in *n–i–p* configurations, due to its low cost and work function (−5 eV) that is almost the same as for Au. To prevent direct electrical contact between the m-TiO_2 and the carbon electrode, which would short circuit the cell, the m-TiO_2 is separated from the carbon top electrode by a thin layer of mesoporous zirconium dioxide ZrO_2 (m-ZrO_2). The mesoporous layers and carbon top electrode can all be made *via* screen printing and the perovskite is introduced by infiltration through the mesoporous stack. Infiltration on a laboratory scale is mostly done manually with a pipette or by inkjet. The perovskite goes through the mesoporous carbon and m-ZrO_2 layers to fill the m-TiO_2. Crystallization of the perovskite in the m-TiO_2 is accomplished by drying at an elevated temperature. The structure is self-adaptable, and several types of perovskites can be used to infiltrate the stack.

In the standard solution made *via* the LARP method, NCs are re-dispersed in toluene. Toluene evaporates extremely fast and when the solution is dropped on the carbon top electrode to pass the m-ZrO_2 layer and fill the m-

60

TiO$_2$, the solvent evaporates before the NCs enter the m-TiO$_2$ to make a functional solar cell. Using energy-dispersive X-ray spectroscopy (EDX) it was not possible to detect traces of any structural element of the NCs (Cs, Pb, Br) in the cross-section of the mesoporous solar cell stack. Because the solvent quickly evaporates, all photoactive material remains on top of the carbon layer. SEM revealed that the NCs on the surface are not on nanoscale but microscale. It is suspected that the carbon layer, made of active carbon, is acting as a filter, and prevents NCs from impregnating the layer stack. NCs halted on the top tend to agglomerate into clusters.

In search of a more compatible solvent to re-disperse NCs, solvents with lower evaporation rates than toluene were used: γ-butyrolactone (GBL), *N,N*-dimethylformamide (DMF), and dimethyl sulfoxide (DMSO). In these solvents, the fluorescence of the CsPbBr$_3$ NCs diminished to varying degrees. When the CsPbBr$_3$ NCs were dispersed in the highly polar DMF, an unusual effect under UV light was observed. In daylight, the solution became colorless, but under UV light the solution produced an intense orange PL emission, i.e., red shifted from the green emission in a polar solvent. The red shifted PL is tentatively attributed to originate from trap states but does not give detailed information on the changes that occur in the NCs. The process is partly reversible. By adding toluene, the solution becomes turbid yellow, but less fluorescent under UV light than previously. Also, when the solution was spin coated and annealed at 60 °C for a few minutes, the film turned from colorless to yellow.

The observed red shifted emission in DMF under UV illumination is in contrast with observations made by Zhao et al.[13], who reported dimming of fluorescence in polar solvents, due to the instability of the ionic crystal structure. With increasing solvent polarity, the size and morphology of the NCs change. Zhao et al. claim that NCs morphology changes from cuboid to spherical and the size decreases, indicating the destruction of NCs. When the solvent environment is highly polar, protective ligands are removed from the surface and the size decreases, accompanied by the formation of a large number of defects and surface states. The shift of PL band position is a dynamic process, which is jointly determined by the competition between the emission of the free carriers and radiative trap recombination. The PL peak position red shifts when trap emission is enhanced. A slight blue shift can be observed when the emission of free carriers is strong enough.

CsPbBr$_3$ NCs re-dispersed in DMF were infiltrated into the m-TiO$_2$ *via* the carbon electrode with a robot pipette and allowed to dry for 15 min outside and 30 min inside an oven at 60 °C. Then, a MAPI solution was infiltrated by inkjet and allowed to crystallize by drying for 10 min before incubation in an oven at 42 °C for 120 h (with NCs) or 135 h (without NCs) (see Methods for details). In this way, the CsPbBr$_3$ NCs are introduced in the device structure to function as a passivation layer between the m-TiO$_2$ ETL and the MAPI photoactive layer. In

fact, Gao et al.[14] showed that when $CsPbBr_3$ NCs are introduced in an antisolvent, they induce a formation of the passivation layer on top of the perovskite layer, significantly improving the charge transport and power conversion efficiency.

Comparison of solar cells that only use the standard MAPI solution and cells that use $CsPbBr_3$ NCs deposited from DMF before applying the standard MAPI solution showed promising improvements for both fresh and incubated samples. The average *J-V* characteristics are presented in **Figure 3.6.c** and the photovoltaic parameters are summarized in **Table 3.3.** for the best devices. **Figure 3.6.d** shows performance statistics for devices with and without $CsPbBr_3$ and compares performance before and after incubation.
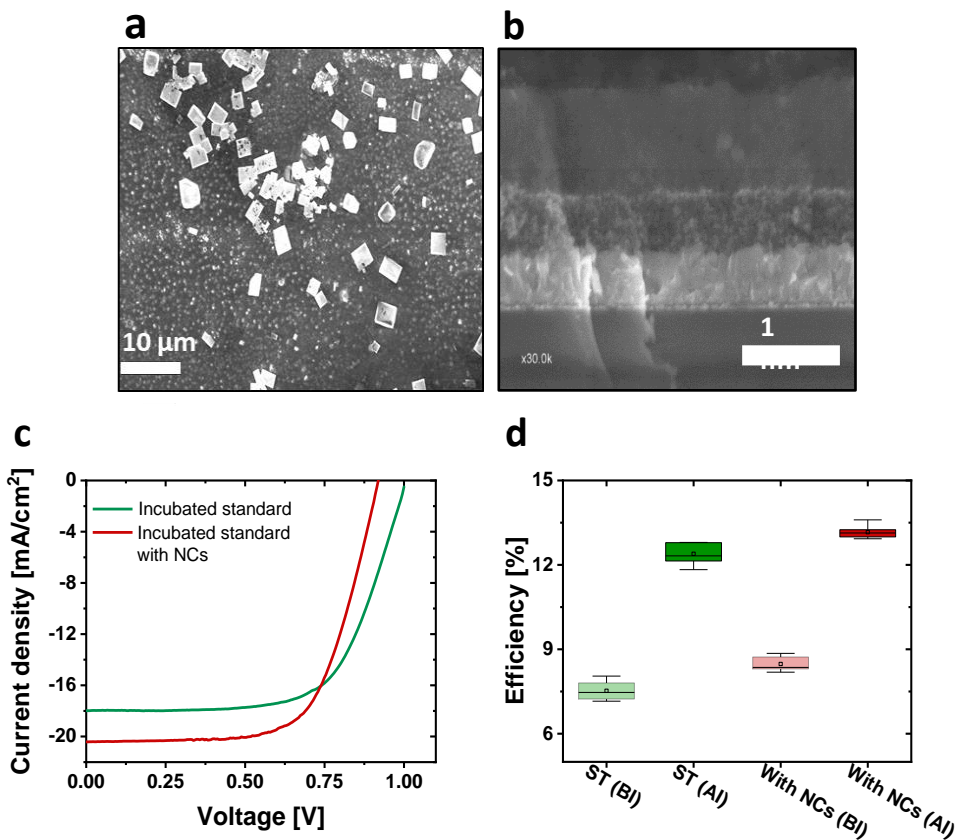
Figure 3.6. Carbon-based-electrode HTL free solar cells. a) SEM image scanned from the top of the device. **b)** EDX analysis of a cross-section of the solar cell. **c)** *J-V* characteristics for MAPI device with and without $CsPbBr_3$. **d)** PCE statistics for MAPI devices without (standard, ST) and with $CsPbBr_3$ NCs passivation before incubation (BI) and after incubation (AI).

The main contribution to the enhanced efficiency comes from the increased V_{OC}, which is on average 0.92 V for the standard stack (MAPI) and 0.98 V for the stack with $CsPbBr_3$ NCs. Repeated experiments gave comparable results. Hence, with a very simple additional step using infiltration of $CsPbBr_3$ NCs dispersed in DMF, the standard device performance improved by about 10%. The experiments with NCs infiltration used a shorter incubation time, which is an important parameter for up-scaling and industry. Even though the efficiency of both stacks decreased in a period of a few months, the devices with the infiltrated $CsPbBr_3$ NCs kept better performance.

Table 3.3. Summary of the solar cell parameters measured for standard MAPI carbon-based devices with and without $CsPbBr_3$ NCs as a passivation layer before incubation (BI) and after incubation (AI).

Configuration	V_{OC} (V)	J_{SC} (mA/cm^2)	FF	PCE (%)
MAPI (BI)	0.90	12.6	0.71	8.0
MAPI with $CsPbBr_3$ (BI)	0.92	14.3	0.67	8.9
MAPI (AI)	0.93	20.0	0.68	12.8
MAPI with $CsPbBr_3$ (AI)	0.98	20.0	0.69	13.6

3.3. Conclusion

Two different methods, HI and LARP, have been explored and optimized to synthesize $CsPbBr_3$ NCs. Both methods come with advantages and disadvantages. For NCs synthesized at room temperature *via* LARP, the main problem is precipitation which leads to hazy and rough layers. This precipitation occurs because the NCs have a tendency to agglomerate, likely because of the short organic ligands. However, the LARP method is easy to reproduce, and the short ligands make layers resilient against wiping off and removal in subsequent depositions. In the optimized LARP method, precipitation was largely overcome and only occurred on time scales of tens of minutes to hours. The main disadvantage of NCs made *via* the HI procedure, is that layers are very thin and fragile and thus need an extra washing step with $Pb(NO_3)_2$ after each deposition step to fixate the previous layer before a new layer can be applied. Considering these characteristics, the LARP method was chosen to fabricate *n–i–p* solar cells.

Optimizing a range of processing parameters such as concentration, ligand washing, thermal annealing time, and spin coating speed, led to reproducible planar *n–i–p* solar cell devices with $V_{OC} \approx 1.3$ V, $J_{SC} \approx 3.5$ mA/cm^2, and FF ≈ 0.6 resulting in a PCE of up to 2.7%. While these results show that working nanocrystalline $CsPbBr_3$ cells can be obtained, the efficiency reached is

not up to par with what is expected or necessary for their use in multi-junction solar cells.

Even though no high efficiencies were reached using CsPbBr$_3$ NCs as absorbing layer, their use as passivation layer between m-TiO$_2$ and MAPI in carbon-based devices proved beneficial. CsPbBr$_3$ NCs were re-dispersed in DMF and used for an additional infiltration step for mesoporous *n–i–p* solar cell devices with MAPI as absorbing layer. With this approach, the performance of standard devices improved by 10% even at a shorter incubation time.

3.4. Methods

3.4.1. CsPbBr$_3$ NCs synthesis, films and planar *n–i–p* devices

Materials

Propionic acid, 2-propanol, cesium carbonate (Cs$_2$CO$_3$), butylamine, methyl acetate, oleic acid, oleylamine, rhodamine 6G, lead nitrate (Pb(NO$_3$)$_2$), acetonitrile (anhydrous 99.8%), 4-tert-butylpyridine, and bis(trifluoromethylsulfonyl)amine lithium salt (99.95% trace metal basis) were purchased from Sigma Aldrich. Anhydrous *n*-hexane and toluene were purchased from Thermo Fisher. Lead bromide (>98%) was purchased from TCI. An aqueous colloidal dispersion of tin oxide (SnO$_2$) (15 wt%) was purchased from Alfa Aesar. Spiro-OMeTAD (99.5%) was obtained from Lumtec and tris(2-(1H-pyrazol-1-yl)-4-tert-butylpyridine)cobalt(III) tri[bis(trifluoromethane)sulfonimide] (Co(III)-TFSI) from Greatcell Solar. Sodium dodecyl sulphate (99%) was from Acros.

Hot-injection

Two precursor solutions were made. The cesium precursor was made by mixing Cs$_2$CO$_3$ (100 mg), oleic acid (0.6 mL), and octadecene (5 mL) under nitrogen flow at 150 °C for 1 h. The lead precursor was made using octadecene (5 mL) and PbBr$_2$ (0.36 mmol). To this mixture oleylamine (0.5 mL) and oleic acid (0.5 mL) were added to stabilize the solution. The PbBr$_2$ precursor solution was heated at 180 °C for 1 h. Then, the cesium precursor solution (0.4 mL) was added to the lead precursor solution and kept at 180 °C for 10 s, after which the crystallization was stopped by immersion in an ice bath to quickly cool the solution. Particles were re-dispersed in toluene.

Ligand-assisted re-precipitation

The cesium propionate precursor solution was made by dissolving Cs$_2$CO$_3$ (162.42 mg) in propionic acid (0.25 mL). The lead bromide precursor solution was made by dissolving PbBr$_2$ (183.5 mg) in a mixture of butylamine (0.3 mL), propionic acid (0.3 mL), and 2-propanol (0.3 mL). The order of solvents is important, and they should be used in this order: butylamine, propionic acid, and 2-propanol. Then the cesium propionate solution (50 µL) was added to a mixture of *n*-hexane (10 mL) and 2-propanol (5 mL), and almost at the same time (as fast as possible after first precursor), the PbBr$_2$ precursor solution (500 µL) was injected. Both precursors were added under the vigorous stirring. Directly after the synthesis, purification was done by centrifugation at 400 relative centrifugal force

(around 1000 rpm) for 4 min and re-dispersion in 6 mL of toluene. Purification was done two times in a row.

Film and solution characterization

UV-vis-NIR spectra were measured using a PerkinElmer Lambda 1050 spectrometer. Surface morphology was characterized using a scanning electron microscope (Thermo Fischer Scientific, Quanta 3D FEG) using a 10 kV electron beam and a secondary ion beam detector. PL spectra of either solutions or films were recorded with an Edinburgh Instruments FLSP920 double-monochromator spectrometer. For TEM, a Tecnai G2 Sphera transmission electron microscope (FEI) operated at 200 kV has been used. XRD measurements were conducted in ambient conditions using a Bruker 2D phaser using Cu Kα (λ = 1.5405 Å) as X-ray source. Measurements were performed in the range 3° to 40° with a step size of 0.02° and collection time of 1 s.

Photoluminescence quantum yield (PLQY)

The PLQY is defined as the ratio of emitted photons (N_e) and the number of absorbed photons (N_a) at a given wavelength:

$$\Phi_f = \frac{N_e}{N_a} \tag{3}$$

Since the absolute value of N_e cannot be easily determined quantitatively, the PLQY of a solution (sample) Φ_f^s is usually determined relative to that of a known reference Φ_f^r :

$$\phi_f^s = \phi_f^r \frac{f_r(\lambda_{ex})}{f_s(\lambda_{ex})} \frac{\int_{\lambda_{em}} F^s(\lambda_{em})\,d\lambda_{em}}{\int_{\lambda_{em}} F^r(\lambda_{em})\,d\lambda_{em}} \frac{n_s^2}{n_r^2}$$

$$f_s(\lambda_{ex}) = 1 - 10^{-A_s(\lambda_{ex})}$$

$$f_r(\lambda_{ex}) = 1 - 10^{-A_r(\lambda_{ex})} \tag{4}$$

Here $f_s(\lambda_{ex})$ and $f_r(\lambda_{ex})$ are the fractions of absorbed photons at the excitation wavelength (λ_{ex}), $F^s(\lambda_{em})$ and $F^r(\lambda_{em})$ are the PL intensities at the respective emission wavelengths (λ_{em}), n_s and n_r are the refractive index of the solvents used to dissolve the sample and reference, and A_s and A_r are the aborbance for sample of interest and reference.

The absorption and emission spectra of the sample and reference material should be in similar wavelength ranges and the absorbances and A_s and A_r should be less than 0.1.

Device fabrication

Bare glass (for thin films) or patterned ITO coated glass (for solar cells) substrates (Naranjo Substrates, 15-17 Ω/sq.) were cleaned in an ultrasonic bath of acetone, followed by scrubbing with a sodium dodecyl sulphate soap solution in deionized water, sonication in the soap solution, rinsing in deionized water followed by sonication in 2-propanol. They were then exposed to UV-O$_3$ treatment for 30 min. As ETL, a commercial 15 wt% tin oxide (SnO$_2$) aqueous colloidal dispersion was spin coated at 2800 rpm for 60 s, subsequentially annealed at 150 °C for 30 min. The CsPbBr$_3$ NCs absorber layer was deposited at 900 rpm, for 45 s. Usually, several consecutive layers were spin coated. Experiments showed

that spin coating of NCs is preferably done in ambient condition instead of in a glove box under inert (dry and oxygen free) atmosphere. For the hole transport layer (HTL), spiro-OMeTAD (80 mg) was dissolved in chlorobenzene (1 mL) with 4-tert-butylpyridine (28.5 µL) (Sigma-Aldrich, 99.5%) and bis(trifluoromethylsulfonyl)amine lithium salt (17.5 µL) of a stock solution (520 mg/mL) in anhydrous acetonitrile at 60 °C. Before depositing the HTL, Co(III)-TFSI (20 µL) of a stock solution (500 mg/mL) in anhydrous acetonitrile was added to the spiro-OMeTAD solution. The HTL was spin coated at 2000 rpm for 50 s, without further annealing. On top of Au was thermally evaporated under high vacuum (~3 × 10^{-7} mbar) as top electrode, with a thickness of 80 nm.

Device characterization

Current density versus voltage characterizations of solar cells (*J-V*) were performed in reverse or forward sweeps (between + 1.5 V and – 0.5 V) at a rate of 0.25 V/s by a Keithley 2400 source meter. Illumination was done with a tungsten-halogen lamp filtered by a UV filter (Schott GG385) and daylight filter (Hoya LB120) with an intensity adjusted to 100 mW/cm^2. A shadow mask with an aperture smaller than the active area (0.0676 or 0.1296 cm^2) was used to define the illumination area of the cell.

For EQE measurements, the cells were contacted in a nitrogen-filled container. A 50 W tungsten halogen lamp was used as light source. The light was chopped at 158 Hz before passing into a monochromator (Oriel, Cornerstone 130). A reference silicon detector was used to calibrate the current from the cell which was fed into a current pre-amplifier (Stanford Research, SR 570). The resulting voltage was measured using a lock-in amplifier (Stanford Research, SR 830). A green (Thorlabs, M530L3) LED was used as a light bias to generate approximately 1-Sun equivalent illumination intensity. Integration of the EQE with the AM1.5G spectrum afforded values of J_{SC}. To measure EQE in the sub-bandgap region, an Oriel 3502 light chopper, Cornerstone 260 monochromator (CS260-USB-3-MC-A), a Stanford Research SR 570 low-noise current preamplifier, a Stanford Research SR830 lock-in amplifier, and a 250 W tungsten-halogen lamp were used.

For sensitive EQE experiments the procedure described in Chapter 5 was used.

3.4.2. Carbon-based electrode devices

Materials

Metal oxide pastes (Ti-Nanoxide T165/SP and Zr-Nanoxide ZT/SP), silver paste (Elcosil SG/SP), carbon paste (Elcocarb B/SP), and methylammonium lead iodide perovskite solution (MAPI) were provided by Solaronix SA. Acetone and 2-propanol were purchased from Carl-Roth. *N,N*-dimethylformamide (DMF), titanium diisopropoxide bis(acetylacetonate), absolute ethanol, and terpineol were purchased from Sigma Aldrich.

Screen printing of the carbon-based electrode devices

Screen-printing is a process of transferring a pre-made design onto a desired surface using ink, a mesh screen, and a squeegee. This method involves creating a stencil on a mesh screen and then pushing ink through it, to create a desired design on the surface. In the process of making solar cells, the inks are pastes containing TiO$_2$, ZrO$_2$, or carbon and

the substrate is glass covered with FTO. Printing is carried out on the DEK 248 screen printer, using screens provided by Solaronix SA. Most of the following descriptions can also be found in the Solaronix brochure[2].

Silver contact: The silver contacts are printed from silver paste and dried at 125 °C for 10 min. Before drying, contacts are easy to wipe. After leveling and drying, the layer is sturdy enough to be used later for a subsequent printing without firing. Firing helps with adhesion to the FTO and it is done at very high temperatures, such as 500 °C, for 30 min.

Compact TiO$_2$: Freshly cleaned substrates are warmed at 410 °C on a titanium hot plate set to 450 °C. The areas for future electrical contacts are masked to protect the FTO surface. A diluted solution of titanium diisopropoxide bis(acetylacetonate) ($[(CH_3)_2CHO]_2Ti(C_5H_7O_2)_2$) in absolute ethanol is sprayed with an air brush using O$_2$ as a carrier gas.

Mesoporous titania layer: The titania paste Ti-Nanoxide T/SP, used to obtain a thin layer m-TiO$_2$ layer, is made with 1:1 dilution of Ti-Nanoxide T/SP in terpineol. The Ti-Nanoxide T/SP paste contains anatase titania particles of 15 to 20 nm, at concentration of ~18 wt% in terpineol with organic binders. The resulting layer is transparent. The ink viscosity changes with temperature and it is best to print at a room temperature between 22 and 25 °C. The titania paste formulation contains binders to avoid a decrease in viscosity that accompanies dilution.

The mesoporous titania layer is printed and dried at 120 °C for 10 min, after 10 min of leveling. Printing on a 165-30 polyester mesh typically yields a 500 nm thick layer after firing at 500 °C for 45 min.

Mesoporous zirconia layer: The zirconia paste Zr-Nanoxide ZT/SP is used to obtain an insulating layer. The Zr-Nanoxide ZT/SP paste contains zirconia particles of 20 to 40 nm at a concentration of ~18 wt% in terpineol with organic binders. The ink viscosity changes with temperature and is best to print at a room temperature between 22 and 25 °C.

The mesoporous zirconia layer is printed and dried at 120 °C for 10 min, after 10 min of leveling. Printing was performed on a 90-48 polyester mesh and yields a 1-micron thick layer after firing at 500 °C for 45 min. After firing, the zirconia particles form a mesoporous layer allowing perovskite impregnation of the underneath layers. Thanks to a composition exclusively made of nanoparticles, the resulting zirconia layers can be around 1 µm thin, whilst ensuring electrical insulation without sacrificing device thinness and charge extraction.

Carbon layer: The carbon paste is based on a 4:1 mix of graphite and carbon black. A low sheet resistivity (≈ 20 ohm/sq) is achieved by the use of larger graphite particles and more suitable milling conditions. Their adhesion is excellent on multiple substrates. It is possible to stack several prints to achieve the desired electrode thickness and resistivity. The carbon paste Elcocarb B/SP is printed and dried at 120 °C after 10 min of leveling. Printing on a 43-80 polyester mesh typically yields a 15 µm thick layer after firing at 400 °C.

The carbon layer is fired on programmable titanium hot plate at 400 °C for 30 min, after a 30 min ramp. It is not advised to fire carbon layers above 450 °C, because they become

---

[2] https://www.solaronix.com/materials/products/

brittle. Firing at 400 °C leads to a highly conductive, hydrophobic, and non-metallic layer that remains porous. The chemical inertness of this layer enables a broad range of material compatibility with no risk of corrosion. Ink viscosity changes with temperature and it is best to print at a room temperature between 22 and 25 °C.

Figure 3.7 shows 18 cells prepared by screen-printing layers, ready for infiltration of the perovskite solution to complete the device.
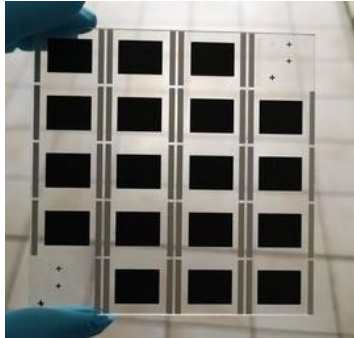
Figure 3.7. Plate with 18 cells prepared by screen-printing layers. In this configuration the cells are ready for infiltration of the perovskite solution to complete the device.

Infiltration

The perovskite solution can be infiltrated in a single step (with the perovskite precursor solution) or in two steps. For the **one-step** solution deposition method, an equimolar solution of lead (II) iodide (PbI_2) and methylammonium iodide (MAI) is deposited on a top of the mesoporous electrode. For the **two-step** solution deposition method, lead (II) iodide is first introduced from a solution into the mesoporous electrodes and subsequently transformed into the $MAPbI_3$ by exposing it to a solution of methylammonium iodide (MAI). The single step is preferable from an industry point of view and for practical reasons.

In the work presented here, we used one-step solution deposition. Substrates are masked with impregnation mask to prevent spreading of the perovskite precursor solution. This is a crucial step which helps with avoiding lead traces on the glass and also preserves the exact volume of infiltrated solution. The infiltration is accomplished by drop-casting a preferred volume of solution, with a pipette. The volume is adjusted depending on the carbon area from an empirical reference amount of 5.75 μL. Drop casting can be done manually or with a robot-pipette. Another technique is inkjet printing, which can be performed at Solaronix with a SÜSS LP50 desktop inkjet printer, using PiXDRO technology.

The drying process for drop-cast method consisted of several steps:

- Drying in a closed box at a room temperature for 30 min.

- The box with its lid on was placed in an oven at 50 °C, to initiate slow crystallization.

- After 30 min, the lid was removed, and the substrates were allowed to dry for 60 min more.

- At this point the cells looked completely dry, showing a brown-orange colored rim on the edge. The active layer is deep black, glossy and homogenous.

Freshly obtained samples were immediately measured using a solar simulator and these samples have 6-8 % efficiency for standard solution. Then, the samples are left for incubation in an oven at 42 °C. In a plastic box, the samples are placed on a small shelf (facing carbon side down) with a small bowl containing water and sodium chloride, next to them. The aim of the salt and water is to establish 75% RH. Standard for incubation is 135 h, when samples are reaching 12-13% efficiency.

Characterization

The current density-voltage (*J-V*) characteristics of the solar cells were measured with a source meter at a scan rate of 5 mV/s using a class A solar simulator providing 1000 W/m^2 simulated AM1.5G illumination, corrected for spectral mismatch. Cells were covered with a mask of 0.64 cm^2 area.

EDX images were obtained using Zeiss EVO 10 scanning electron microscope.

3.5. References

1. Koscher, B. A., Nett, Z. & Alivisatos, A. P. The Underlying Chemical Mechanism of Selective Chemical Etching in CsPbBr$_3$ Nanocrystals for Reliably Accessing Near-Unity Emitters. *ACS Nano* **13**, 11825–11833 (2019).

2. Li, Y., Huang, H., Xiong, Y., Kershaw, S. V. & Rogach, A. L. Revealing the Formation Mechanism of CsPbBr$_3$ Perovskite Nanocrystals Produced via a Slowed-Down Microwave-Assisted Synthesis. *Angew. Chem.* **130**, 5935–5939 (2018).

3. Thanh, N. T. K., Maclean, N. & Mahiddine, S. Mechanisms of nucleation and growth of nanoparticles in solution. *Chem. Rev.* **114**, 7610–7630 (2014).

4. Koolyk, M., Amgar, D., Aharon, S. & Etgar, L. Kinetics of cesium lead halide perovskite nanoparticle growth; Focusing and de-focusing of size distribution. *Nanoscale* **8**, 6403–6409 (2016).

5. Pan, J. *et al.* Bidentate Ligand-Passivated CsPbI$_3$ Perovskite Nanocrystals for Stable Near-Unity Photoluminescence Quantum Yield and Efficient Red Light-Emitting Diodes. *J. Am. Chem. Soc.* **140**, 562–565 (2018).

6. He, X., Qiu, Y. & Yang, S. Fully-Inorganic Trihalide Perovskite Nanocrystals: A New Research Frontier of Optoelectronic Materials. *Adv. Mater.* **29**, 1700775 (2017).

7. Protesescu, L. *et al.* Nanocrystals of Cesium Lead Halide Perovskites (CsPbX$_3$, X = Cl, Br, and I): Novel Optoelectronic Materials Showing Bright Emission with Wide Color Gamut. *Nano Lett.* **15**, 3692–3696 (2015).

8. Brennan, M. C., Kuno, M. & Rouvimov, S. Crystal Structure of Individual $CsPbBr_3$ Perovskite Nanocubes. *Inorg. Chem.* **58**, 1555–1560 (2019).

9. Liang, Z. *et al.* Shape-Controlled Synthesis of All-Inorganic $CsPbBr_3$ Perovskite Nanocrystals with Bright Blue Emission. *ACS Appl. Mater. Interfaces* **8**, 28824–28830 (2016).

10. Sanehira, E. M. *et al.* Enhanced mobility $CsPbI_3$ quantum dot arrays for record-efficiency, high-voltage photovoltaic cells. *Sci. Adv.* **3**, eaao4204 (2017).

11. Akkerman, Q. A. *et al.* Strongly emissive perovskite nanocrystal inks for high-voltage solar cells. *Nat. Energy* **2**, 16194 (2016).

12. Falsini, N. *et al.* Analysis of the Urbach tail in cesium lead halide perovskites. *J. Appl. Phys.* **131**, 010902 (2022).

13. Zhao, A. *et al.* Fluorescent dynamics of $CsPbBr_3$ nanocrystals in polar solvents: A potential sensor for polarity. *Nanotechnology* **32**, 135701 (2021).

14. Gao, Y. *et al.* $CsPbBr_3$ perovskite nanoparticles as additive for environmentally stable perovskite solar cells with 20.46% efficiency. *Nano Energy* **59**, 517–526 (2019).

4

Life cycle assessment of CsPbBr₃ perovskite nanocrystals and solar cells

Abstract

High power conversion efficiency, low costs of materials, simple and eco-friendly manufacturing are key requirements for solar cells. A promising candidate in such search are perovskite solar cells. Perovskite nanocrystals (NCs) are semiconductors with exceptional photophysical and primary optoelectronic properties. In addition, their easy synthesis and processability by using widely available chemical components makes them attractive for mass production. CsPbBr₃ NCs can be synthesized *via* the hot-injection (HI) and ligand-assisted re-precipitation (LARP) methods. From the point of view of ecodesign, a life cycle assessment (LCA) is essential to choose and/or redefine the processes that are to be up-scaled to an industrial level. To determine the environmental impact of perovskite solar cells, a cradle-to-gate LCA study has been conducted. Results show that for lead halides the highest contribution in all impact categories stems from lead. However, for CsPbBr₃ NCs prepared *via* LARP, 2-propanol has the largest impact, while in the HI method it is octadecene. A comparison of the contributions to emissions, coming from the HI and LARP methods to produce 1 kg of CsPbBr₃, shows that LARP has a lower impact in almost all categories. Perovskite NCs itself do not significantly contribute to global emission as compared to other layers in perovskite solar cell fabrication, which is a promising outcome for the future of perovskite solar cells.

4.1. Introduction

With the growth of the world population, the demand for energy is constantly increasing. Besides the fact that non-renewable energy sources are decreasing, conventional fossil-fuel energy production causes environmental issues so that switch to renewable energy sources is required. Still, the majority of the total primary energy comes from coal, oil, and natural gas (see Chapter 1). This causes an increase in carbon dioxide emission and leads to an increase in average global temperature above 1 °C, severely impacting the world's climate. By signing the Paris agreement (COP21-2015)[1], 196 parties recognized global warming as an important issue through a legally binding international treaty, and agreed to provide financial and technological solutions to the problem. The goal of this agreement is to limit global warming to well below 2 °C, preferably to 1.5 °C.

The environmental impact is important because businesses and research aim to improve the environmental performance of their products and activities. The assessment of all environmental impacts from raw material extraction (cradle), through manufacture, maintenance, and, finally, to the end of life (grave) is used to support decisions on ways to improve the products. The most common method to assess the environmental performance of a product is life cycle assessment (LCA).

In ISO 14040, LCA is defined as the "compilation and evaluation of the inputs, outputs, and potential environmental impacts of a product system throughout its life cycle"[2]. LCA provides quantitative information of each stage involved in the whole life cycle, as presented in **Figure 4.1**.**a**. LCA is an iterative process aimed at providing an improvement of the environmental performance of products (**Figure 4.1.b**). LCA is a quantitative description of a broad range of environmental impacts *via* various impact categories, such as global warming, ionizing radiation, human health, fresh and marine water, land use, water consumption, etcetera. LCA can be used for comparison of already existing products and is likewise important in the development of new products.

LCA is a tool for the analysis of the environmental burden of products, from the extraction of resources, through the production of materials, product parts and the product itself, and the use, transport and maintenance of the product. Usually, LCA includes management of the product after it is discarded, either by reuse, recycling, or final disposal. Depending on the starting and ending points of the analysis, there are four types of LCA:

- Cradle-to-grave (from raw material resources, through the use phase, ending with the end of life).
- Cradle-to-gate (from raw material resources to the factory gate).

- Cradle-to-cradle (from raw material resources, through the use phase and end of life, ending with considering disposal stage).
- Gate-to-gate (impact of a single production step).
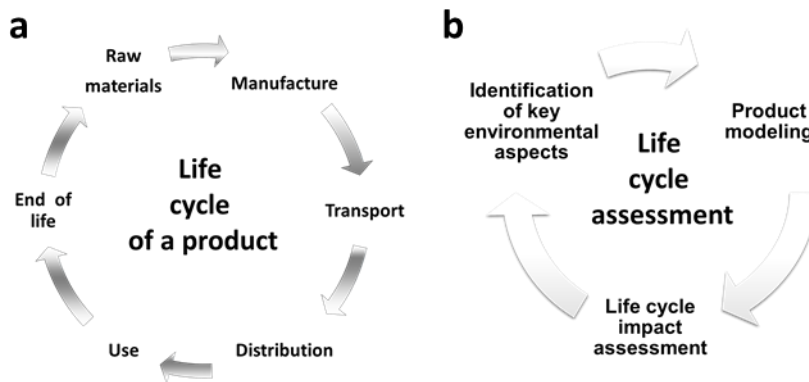
Figure 4.1. Life cycle assessment (LCA). a) Life cycle of a product, from raw material to end of life. **b)** Iterative nature of LCA.

Perovskite nanocrystal (NC) semiconductors are easy to process with widely available chemical components, which makes them very attractive for large-scale production. Different synthetic processes for $CsPbBr_3$ NCs have been reported, but the hot-injection (HI) and ligand-assisted re-precipitation (LARP) methods are most used. The difference between these methods is in the processing conditions. While LARP is conducted in a less strictly controlled environment, HI requires elevated temperatures and a nitrogen atmosphere. To form $CsPbBr_3$ NCs, both methods use two complementary precursor solutions. One precursor solution contains lead bromide ($PbBr_2$) and the other contains a cesium source, prepared from cesium carbonate (Cs_2CO_3). In addition, different ligands are used in NC formation. LARP uses short-chain ligands (butylamine and propionic acid), while HI employs long-chain ligands (oleylamine and oleic acid). Because perovskite solutions and perovskite solar cells are still in a stage of development, it is important to determine their environmental impact before considering their up-scaling processing or industrial production.

Following the recommendations from the ISO 14040 standards series, this chapter provides a LCA on $CsPbBr_3$ perovskite NCs and solar cells based on perovskite NCs as a photoactive layer. The study gives an insight into the environmental impact of the production of 1 kg $CsPbBr_3$ NCs synthesized *via* HI and LARP and their use in solar cell technology.

4.2. Life cycle assessment - Methodology

A methodology to conduct LCA is provided by the International Organization for Standardization (ISO) in ISO 14040:2006(E) and ISO14044:2006(E)[3]. The methodology consists of four stages, shown in **Figure 4.2**. In order, the four phases are: goal and scope, inventory analysis, impact assessment, and interpretation.
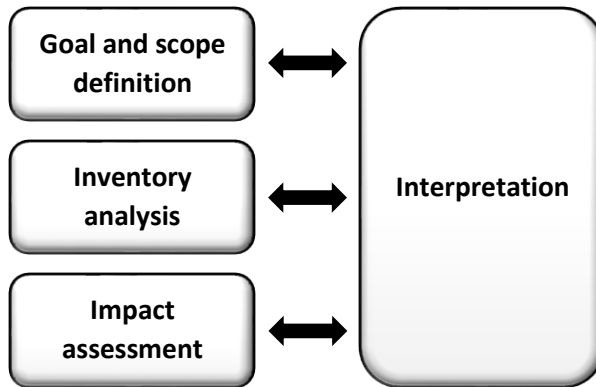
Figure 4.2. The phases of LCA according to ISO 14040:2006

- Goal and scope definition of the study

    Defining the goal and scope is the first step in a LCA study. In this step, it is necessary to define the reasons for carrying out the study, the intended application, target audience, and to describe the limitations of the study. Additionally, this phase describes the functional unit, data requirements, system boundaries, main assumptions, methodology, and interpretation method.

- Life cycle inventory

    When data are collected and interpreted, the analyses of the result are presented in a flow chart. The data must be adjusted to the functional unit and material flow. Energy requirements have to be calculated for each process.

- Life cycle impact assessment

    The life cycle impact assessment (LCIA) provides information for the final stage (interpretation phase) from an environmental perspective using different environmental category indicators. Following the ISO 14044:2006 guidelines, the LCIA phase must be carefully planned to achieve the goal and scope of an LCA study. The LCIA phase must be

coordinated with other phases of the LCA to consider possible omissions and sources of uncertainty.

- Interpretation of the study

   Interpretation, as a final stage is aimed to analyze the results and relate them to the goal and scope. In this stage the conclusions of the entire study are presented.

4.3. Goal and scope

This LCA has been conducted in the framework of the European Joint Doctorate (EJD) project eSCALED. The scientific goal of eSCALED is the development of new materials to be integrated into an artificial photosynthetic device. In this section, the goal and scope of the LCA are described. The goal is determined by the purpose and reason to carry out the study, the target audience, and the dissemination of the results to the public. The scope considers the product system, functional unit, system boundaries, data source, data quality requirements and assumptions.

4.3.1. Goal

4.3.1.1. Purpose and reasons for the study

In the work presented here, we consider the environmental impact of the production of perovskite NCs and their use in solar cells. The cells are considered as a component of a future artificial leaf that mimics natural photosynthesis, e.g., producing H_2 or solar fuels at the cathode and O_2 at the anode by catalyzed electrochemical reactions, driven by solar energy.

Our study aims to pinpoint the elements of NC manufacturing that have the largest environmental impact. This chapter focuses on defining the methodology for the production and integration of the required materials into a solar cell, at the laboratory level. Special emphasis was put on perovskite NCs which are used as a photoactive layer. The subsequent phases – use and end-of-life phases – are not evaluated in this study because there is not sufficient data on, e.g., maintenance of the device, disassembling, and disposal, meaning that the cradle-to-gate approach has been finally considered.

4.3.1.2. Intended applications and audience

This study should serve as an evaluation of the possible large-scale production of perovskite NCs and the up-scaling of perovskite solar cells. The intended audience of this report is the European Commission (EC) and the academic partners and private commercial beneficiaries that are involved in the eSCALED

project. In addition, the scientific community is addressed through this PhD thesis, presentation at international conferences, and the potential publication of scientific papers. Results of this study have been shared with the audience during the Society of Environmental Toxicology and Chemistry (SETAC) Europe 32nd annual meeting in Copenhagen (May 2022).

4.3.1.3. Type of critical review

This study has been reviewed internally by LCA experts at Eurecat Technology Center.

4.3.2. Scope

4.3.2.1. Functional unit

The functional unit describes the primary function to be fulfilled by a product system and indicates how much of this function is to be considered in the intended LCA study. This study was conducted in two directions: LCA for NCs and LCA for solar cells. In this sense, there are two functional units. Depending on the direction of the LCA, they are:

- Concerning the production of the NCs, the functional unit is defined as the amount of materials and energy required for the manufacturing of 1 kg $CsPbBr_3$ NCs. Thus, the functional unit was chosen to be 1 kg. This applies to 1 kg of crude substance, without being re-dispersed in a particular solvent.
- Concerning the production of the solar cell, the functional unit is defined as the amount of materials and energy required for manufacturing a 9 cm^2 laboratory-scale device with four small solar cells of which two have an active area of 0.09 cm^2 and two of 0.16 cm^2. Hence, the functional unit was chosen to be a 9 cm^2 device.

4.3.2.2. System boundaries

The LCA study aims to provide a full picture of the environmental impact of the development of perovskite NCs solutions and perovskite solar cells with a photoactive layer made of NCs, following a cradle-to-gate approach. This approach provides insight into the environmental impact of perovskite NCs and perovskite solar cells from the raw materials (cradle) to the end of production (gate). Studying the impact of the usage of solar cells would have been too complicated at this stage of development and it would add greater uncertainties to the study.

4.3.2.3. Data source and quality requirement

Primary data is acquired by the PhD candidate, coming from the different experimentation tests held. The secondary data has been recovered from the literature and the Ecoinvent v3.3 database included in the SimaPro software.

The retrieved data have been analyzed under the following requirements:

- All processes at each stage are accurately modelled to reflect a real situation. Sources and references for modeling are always provided.
- Data is reproducible and everybody should be able to conduct the study and obtain comparable results.
- Data was collected during the three years of the e-SCALED project and updated on demand.
- Data should be gathered as an average for the European Union.

4.3.2.4. Cut-off criteria

As stated in ISO 14040: 2006 the "cut-off" criteria are a specification of the amount of material or energy flow, or the level of environmental significance associated with unit processes or product systems to be excluded from a study. This LCA study has not developed any cut-off based on mass, energy, or environmental relevance. All inputs to processes are considered in all stages.

4.3.2.5. Assumptions

Quantifying the full range of chemicals required for LCA studies can be a challenging task, especially when laboratory level products are discussed. The SimaPro 8.3.0. database covers many common chemicals and solvents that are required for the manufacturing, but several of them, had to be modelled. Some materials were modelled based on patent data, some with approximation and some from other databases (mostly publications). Due to the lack of data in the SimaPro base, we considered the following assumptions and hypotheses for the production of NCs:

- $PbBr_2$ was modeled according to Gong et al.[4], assuming the same process route applies for $PbBr_2$ and PbI_2.
- Cesium carbonate (Cs_2CO_3) precursor was modeled by lithium carbonate (Li_2CO_3). According to Khalifa et al.,[5] Cs ore (pollucite) can modeled with lithium ore (spodumene). The parallel has been made and Li_2CO_3 is used instead of Cs_2CO_3. The production of both carbonates is similar, and Li and Cs belong to the same group of elements (1A-alkali metals).
- Since butylamine is missing from the database we approximate it with *tert*-butylamine. *Tert*-butylamine is part of the SimaPro database. The difference in the production of butylamine and *tert*-butylamine is in the

use of butanol vs. *tert*-butanol. Since these are isomers, this is a justified approximation.

- In LARP, waste is *n*-hexane, 2-propanol, and leftovers of the unreacted precursor solution. Since we do not have data on the percentage of unreacted precursor solution, we assume that waste products are only *n*-hexane and 2-propanol.
- Fatty acid was used to model oleic acid. This is justified by the fact that oleic acid is a type of fatty acid[6].
- Octadecene (ODE) was modeled as *n*-olefin according to Wickerts et al.[6]
- Oleylamine was modeled according to Baldassarri et al.[7]
- Purification processes are not included because it is not necessary for all and also depends on the application.
- Re-dispersion in non-polar solvents is not included, but a comparison of the impact of the two most-used solvents (*n*-hexane and toluene) is included.
- In HI, waste is octadecene and leftovers of the unreacted precursor solution. Since we do not have data for unreacted precursor solutions, we assume that waste is only octadecene.
- Due to the very low consumption, nitrogen flow was not included.

Furthermore, due to the lack of data in the SimaPro base, we considered assumptions and hypotheses for the production of perovskite solar cells:

- Data for the glass substrate and indium tin oxide (ITO) are from Gong et al.[4].
- The photoactive layer (CsPbBr$_3$ NCs) was modeled as described above.
- Data for the hole transport layer (spiro-OMeTAD) are from Gong et al.[4]. Here, it is important to note that we use Spiro-OMeTAD with two dopants, to achieve better performance. However, because of the negligible amounts that are used and the complexity of modeling, we neglected the dopants in calculations.
- Data for the silver paste is from Gong et al.[4].
- We modeled energy utility mostly on the actual equipment used, unless specifically mentioned otherwise.
- Usage of material with spin coating is only 30%[8], meaning that the input value in SimaPro is the 30% of used amounts.
- Evaporating of metal was estimated to be 82% in material usage[9].

4.4. Inventory analysis

The materials and energy requirements data are gathered and analyzed in the inventory analysis phase to evaluate the impact afterwards. Every unit is

considered for the material and energy flows and emissions relating to the functional unit previously defined in the goal and scope phase. Detailed description of the synthesis of the perovskite NCs is presented in Chapters 1 and 3 of this thesis. The recommendation of international standards is to base the primary data on a mass flow balance, which has been followed.

4.4.1. Unitary process description

The process of manufacturing the perovskite solar cell, related to this study can be broken down into the following steps: the production of precursors, the synthesis of perovskite NCs, and the manufacturing of the solar cell. **Figure 4.3.** gives an overview of the processes included in the production of the solar cell.

The process flow diagram regarding the manufacturing process for perovskite solar cells and perovskite NCs solution is presented in **Figure 4.4.** This diagram only shows the steps after each material is manufactured. The process is taking two separate directions: the production of solar cell layers and the production of perovskite NCs solutions. In the end, they are integrated in the final solar cell. A process flow diagram has been created with the help of the experimental information gathered thus far, and those from other reports to provide a visualization of the process to manufacture the electrode in its entirety.
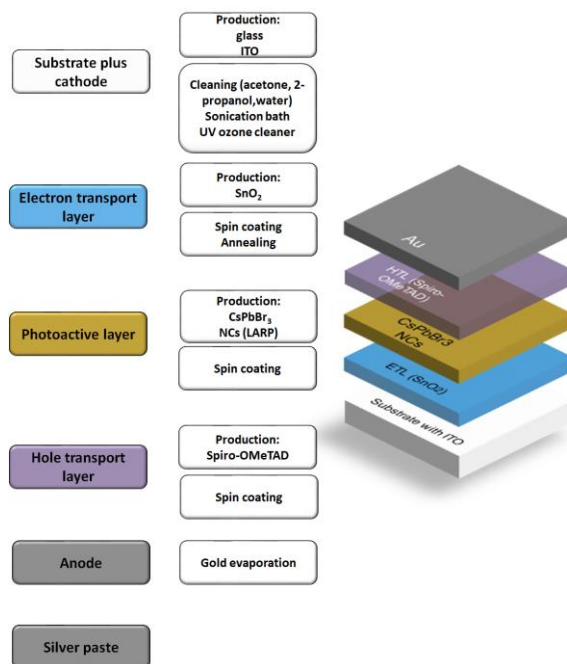
Figure 4.3. Schematic representation of the solar cell layout and the processes connected with the production of each layer.
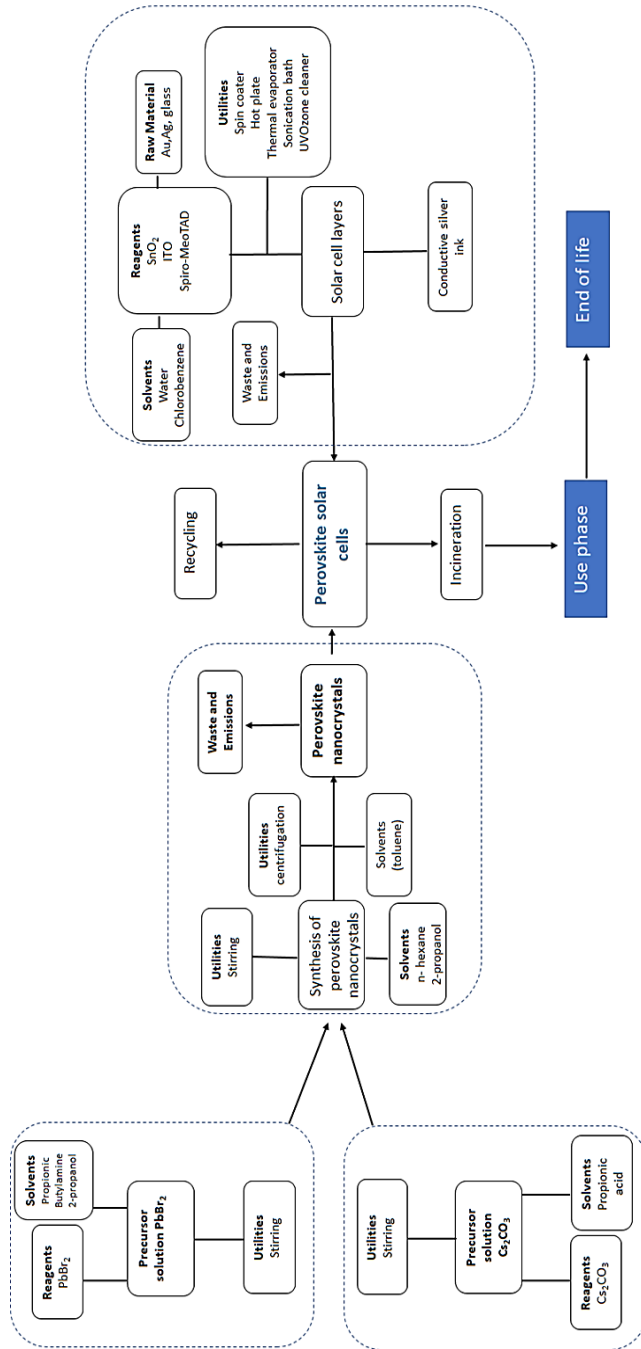
Figure 4.4. Process flow diagram

4.4.2. Description of life cycle inventory data

Inventory data is presented in **Table 4.1.** with values related to the functional unit. More details can be found in Chapter 3 of this thesis.

Table 4.1. Life cycle inventory data for three main processes.

Process	Inputs	Value	Unit
1 kg $CsPbBr_3$ HI	Cs_2CO_3	0.12	kg
	$PbBr_2$	2.20	kg
	Oleylamine	6.77	kg
	Octadecene	70.45	kg
	Oleic acid	0.68	kg
	Ice	1.00	kg
	Energy	0.82	kWh
1 kg $CsPbBr_3$ LARP	Cs_2CO_3	0.54	kg
	$PbBr_2$	1.53	kg
	Butylamine	2.06	kg
	Propionic acid	3.57	kg
	2-Propanol	67.68	kg
	n-Hexane	109.17	kg
	Energy	0.036	kWh
Solar cell (substrate 9 cm^2)	Glass with ITO	9	cm^2
	SnO_2	0.695	g
	$CsPbBr_3$ (LARP)	0.208	g
	Toluene	0.260	g
	Spiro-OMeTAD	0.00225	g
	Silver paste	0.001	g
	Chlorobenzene	0.033	g
	Gold	0.089298	g
	Energy	0.0615	kWh

4.5. Life cycle impact assessment (LCIA) and evaluation

This section first presents the quantification and evaluation of environmental impacts associated with the production of perovskite NCs and is followed by the analysis for production of perovskite solar cells with a photoactive layer made of NCs.

4.5.1. Impact characterization method selection

Emissions for all the materials needed for the preparation of the perovskite solar cells were estimated with the European ReCiPe 2016 midpoint method, hierarchist version 1.01, and the Cumulative Energy Demand version 1.10 as included in SimaPro version 8.3.0.0. **Table 4.2.** summarizes the impact categories considered for this project and their respective abbreviations and units. The focus has been on exploring global warming contribution and hazardous emissions, for humans, marine and freshwater ecosystems. The electricity requirements to power processes such as circulation of cooling water, heating and stirring, which produces emissions such as carbon dioxide, carbon monoxide, aldehydes, sulphate, nitrogen oxides, hydrogen and chlorinated hydrocarbons, will be accounted for in this study. A substantial portion of this amount will be emissions to the air, rather than water or ground pollution.

Table 4.2. Impact categories considered in this study.

Impact category	Acronyms	Unit [1]
Global warming	GW	kg CO_2 eq
Stratospheric ozone depletion	SOD	kg CFC-115 eq
Terrestrial acidification	TA	kg SO_2 eq
Freshwater eutrophication	FE	kg P eq
Marine eutrophication	ME	kg N eq
Freshwater ecotoxicity	FEtx	kg 1,4-DB eq
Marine ecotoxicity	MEtx	kg 1,4-DB eq
Human carcinogenic toxicity	HCT	kg 1,4-DB eq
Human non-carcinogenic toxicity	HnCT	kg 1,4-DB eq
Fossil resource scarcity	FRS	kg oil eq
Water consumption	WC	m^3

[1] CO_2 is carbon dioxide; CFC-115 is chloropentafluoroethane; SO_2 is sulfur dioxide; P is phosphorus; N is nitrogen; 1,4-DB is 1,4 dichlorobenzene,

4.5.2. Results

The LCIA results are presented for the steps required for the fabrication of the individual components:

- Production of main components for perovskite NCs.
- Production of perovskite NCs.
- Production of perovskite solar cells.

Many of the steps in the processes had to be modelled from scratch due to the lack of pre-existing inventory data. They are already indicated in section 4.3.2.5 Assumptions.
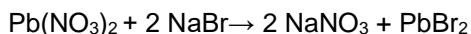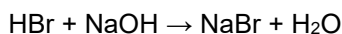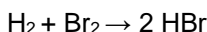
The expected results from the LCA work are:

- Point out steps that have the largest environmental impact in the production of precursors.
- Compare the HI and LARP methods to produce $CsPbBr_3$ NCs and identify the best scenario.
- Point out the procedures that has the largest environmental impact in the manufacturing of perovskite solar cells.

By combining all previously gathered information, results for each scenario are described in the sub-sections below.

4.5.2.1. LCIA of PbBr$_2$

All steps for the production of 1 kg PbBr$_2$ were modelled from scratch due to the lack of pre-existing inventory data in SimaPro. Current perovskite LCA literature assumes the same manufacturing process for PbBr$_2$ and PbI$_2$ and this assumption allows one to use the same values for electricity and heat consumption[4]. PbBr$_2$ modeling was based on the following chemical reactions:

$$3\ Pb + 8\ HNO_3 \rightarrow 3\ Pb(NO_3)_2 + 2\ NO + 4\ H_2O$$

$$H_2 + Br_2 \rightarrow 2\ HBr$$

$$HBr + NaOH \rightarrow NaBr + H_2O$$

$$Pb(NO_3)_2 + 2\ NaBr \rightarrow 2\ NaNO_3 + PbBr_2$$
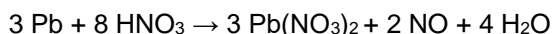
PbBr$_2$ is one of the main components in the production of $CsPbBr_3$. **Figure 4.5.a** shows the impact analyses of the synthesis of 1 kg PbBr$_2$. The main impact contributors in the production of 1 kg PbBr$_2$ are lead (Pb) and by-products (nitric oxide (NO), and sodium nitrate (NaNO$_3$)), depending on the category. Bromine (Br$_2$) also has significant impact. The impact of lead is dominant in categories such as human carcinogenic and non-carcinogenic toxicity, fresh water, and marine ecotoxicity. It does not matter if it is breathed-in, swallowed, or

absorbed, exposure to high levels of lead may cause anemia, weakness, kidney, and brain damage, and in the case of very high levels even death. Although perovskites have tremendous advantages, which are pointed out many times throughout this thesis, the issues involving lead could be one of the main obstacles to its commercialization and large-scale applications.

In global warming emissions (**Figure 4.5.b**), by-products and bromine have the same contribution (both 28%) and these are much higher than lead (8%). Nitric acid has a mentionable impact of 17% and all other impacts are in a range of 10%. The dominant contribution comes from the materials. The energy input (heat) has an impact of 11%.

Figure legend:
- ■ Heat, central or small-scale, natural gas {Europe without Switzerland}| Cut-off, U
- ■ Electricity, low voltage {Europe without Switzerland}| market group for | Cut-off, U
- ■ Water, ultrapure {GLO}| market for | APOS, U
- ■ Hydrogen, liquid {RoW}| market for | APOS, U
- ■ By-products (NO, NaNO3)
- ■ Bromine {GLO}| market for | Cut-off, U
- ■ Nitric acid, without water, in 50% solution state {GLO}| market for | Cut-off, U
- ■ Sodium hydroxide, without water, in 50% solution state {GLO}| market for | Cut-off, U
- ■ Lead {GLO}| market for | Cut-off, U

Figure 4.5. a) Impact analysis of the synthesis 1 kg PbBr$_2$. **b)** Contribution to global warming from the production of 1 kg PbBr$_2$.

4.5.2.2. LCIA of CsPbBr$_3$ NCs

Hot-injection (HI) involves the production of homogeneous nuclei *via* the rapid injection of organometallic reagents into a hot solvent (Chapter 1). The synthesis method was taken from Protesescu et al.[10] and up-scaled to the level of possible production of 1 kg of CsPbBr$_3$ NCs (Chapter 3). The results of the impact analysis are presented in **Figure 4.6.a**. In the production of 1 kg CsPbBr$_3$ NCs *via* the HI method, most environmental impact stems from *n*-olefin, used to model octadecene. This impact is followed by fatty acid, especially in ionizing radiation, or fresh water, and marine ecotoxicity. It is interesting to see that PbBr$_2$, which contains harmful lead, does not have a huge impact in the overall production of perovskite NCs.
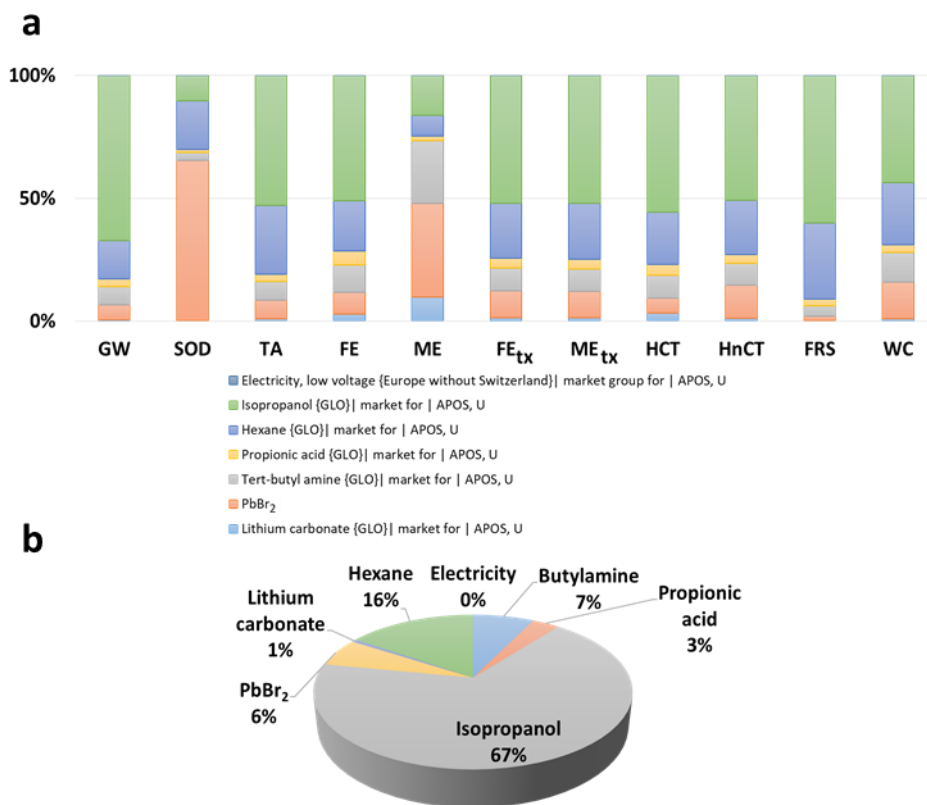
The total contribution to global warming connected with this process is 378 kg CO$_2$ eq. Again, with 72%, *n*-olefin has a major impact, followed by fatty acid (**Figure 4.6.b**). The energy input is at a negligible level.
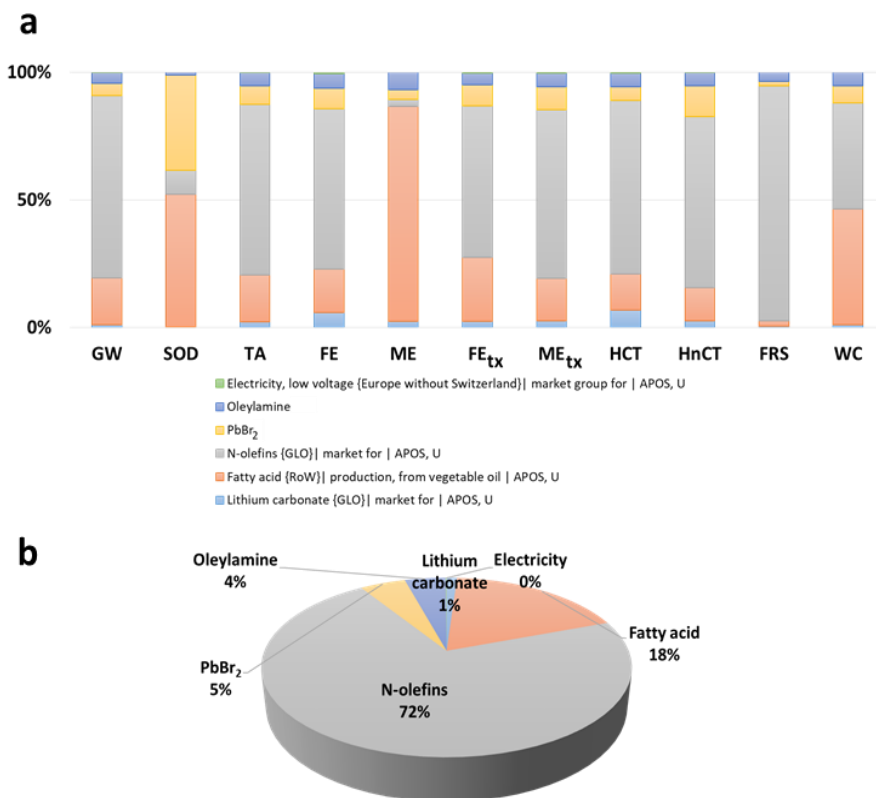
Figure 4.6. a) Impact analysis of the synthesis 1 kg CsPbBr$_3$ with HI. **b)** Contribution to global warming (GW) from the production of 1 kg CsPbBr$_3$ with HI.

The LARP method was taken from the work reported by Akkerman et al.[11] and up-scaled to the level of possible production of 1 kg of $CsPbBr_3$ NCs. NCs made with this method are later used in solar cells.

Figure 4.7.a shows that 2-propanol has the highest environmental impact in the production of 1 kg $CsPbBr_3$ NCs *via* the LARP method. This is followed by the impact of *n*-hexane. These results are not surprising since the amounts of isopropanol and *n*-hexane used are much higher than that of other components. Furthermore, these two compounds are the main waste components in the synthesis, because they do not directly contribute to the NCs but only form the reaction medium. Even though $PbBr_2$ has a noticeable impact, again, lead is not contributing majorly. The electricity impact in the process is negligible and this is one of the main advantages of the LARP method, besides its simplicity.

Figure 4.7. a) Impact analysis of the synthesis 1 kg $CsPbBr_3$ with LARP. **b)** Contribution to global warming from the production of 1 kg $CsPbBr_3$ with LARP.

The total contribution to the global warming connected with the LARP process is 213 kg CO_2 eq. and the ratio between components is shown in **Figure 4.7.b**. 2-Propanol has the highest contribution with 67%, followed by *n*-hexane (16%), butylamine (7%), and lead bromide (6%). The advantages of the LARP method over the HI method are in the mild reaction conditions in which the reaction is made, and the much lower total contribution connected with global warming.
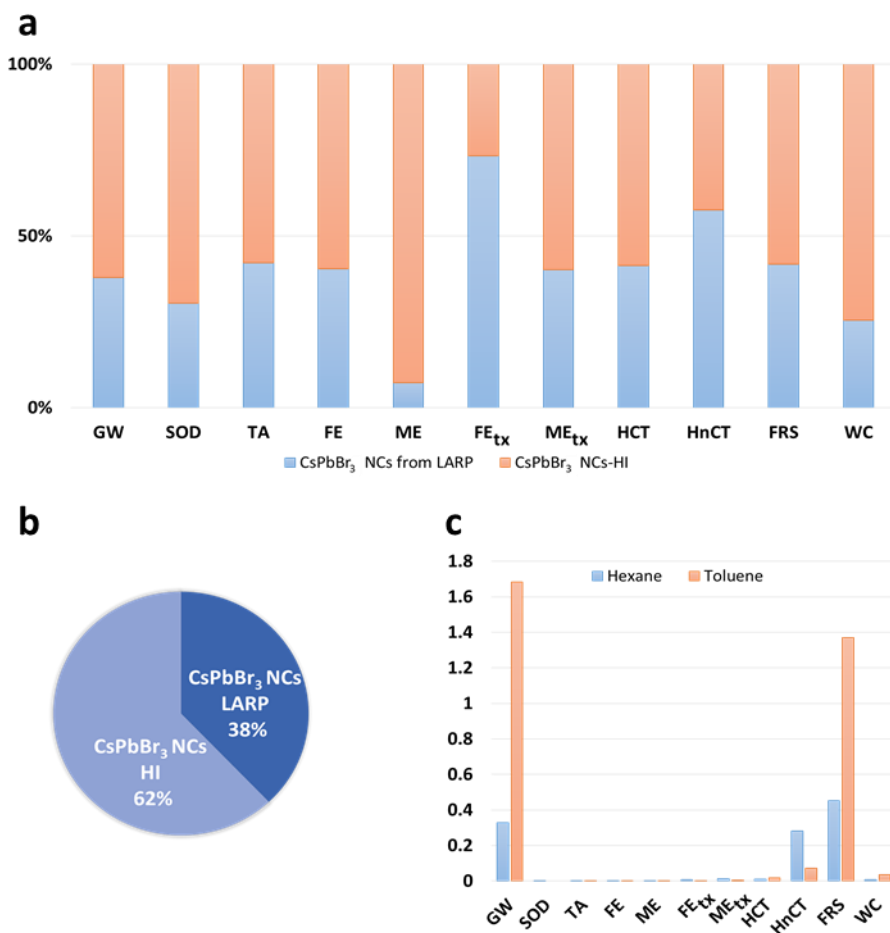
Figure 4.8. Comparison of the synthesis 1 kg CsPbBr₃ with HI and LARP. a) Impact analysis. **b)** Comparison contribution to global warming. **c)** Impact comparison of *n*-hexane and toluene, two most common solvents for NCs dispersion.

It is of interest to compare the contributions to emission, for the same type and amount of NCs (1 kg of CsPbBr₃) but produced in *via* HI or LARP (**Figure 4.8.a**). These results are important for the up-scaling of processes to the industrial

levels. The results show that LARP has a much lower environmental impact than HI in nearly all categories (the exception is fresh water ecotoxicity). Regarding human health, hot-injection is to some extent favorable. LARP is not just a much simpler process compared to HI, but it is also more environmentally acceptable. As shown in **Figure 4.8.b**, the contribution to global warming coming from HI is also much higher.

Nanoparticles are usually re-dispersed in non-polar solvents such as toluene or *n*-hexane. This possibility of making colloidal solutions of NCs in non-polar solvents can be relevant for tandem applications (see Chapter 3). **Figure 4.8.c** shows that *n*-hexane is a more environmentally friendly solvent in comparison with toluene and is preferred over toluene for the re-dispersion of NCs.

4.5.2.3. LCIA of CsPbBr$_3$ NCs based solar cells

Perovskite NCs can be used as a photoactive layer in solar cells. Of the two main methods used for making perovskite NCs presented in Chapters 1 and 3, the NCs made using long chain ligands *via* HI have little tendency to agglomerate. However, to make working photovoltaic devices, the electrically insulating oleic acid and oleylamine capping ligands need to be removed. Among literature, this is mostly done by treating layers with solutions of lead acetate or lead nitrate (Chapter 3). Unfortunately, in each washing step, the NCs are partly stripped off the surface and it is difficult to obtain an active layer that is thick enough for solar cell applications. NCs made *via* LARP with short capping ligands, such as propionic acid and butylamine, provide less stable colloidal dispersions. The main advantage of the LARP method is that it is easy to make multilayers and that the ligands can be removed by simple drying or thermal annealing. Hence, it is possible to make a thick enough active layer for a functional solar cell. In addition, the amount of material that can be conveniently made *via* LARP is high. These were the main reasons for using the room-temperature LARP synthesis route to CsPbBr$_3$ NCs for single-junction photovoltaic cells. Solar cells were made in a *n–i–p* configuration as shown in **Figure 4.3.** Further details can be found in Chapter 3.

The devices are processed on a glass substrate (3 cm × 3 cm) on which four solar cells are fabricated. Two of these solar cells have an active area of 0.09 cm^2 and two of 0.16 cm^2. The impact analysis presented here is for a device, produced on laboratory scale, with techniques as spin coating, metal evaporation, etcetera. It is important to note that techniques such as spin coating are not going to be used in an up-scaled process, but this LCA can give a general overview for taking decisions in the further investigation of perovskite solar cells.

Figure 4.9.a shows that the gold electrode has the largest environmental impact. Gold is a noble metal with a considerably high primary energy consumption. Gold is expensive and its mining is dangerous for human health.
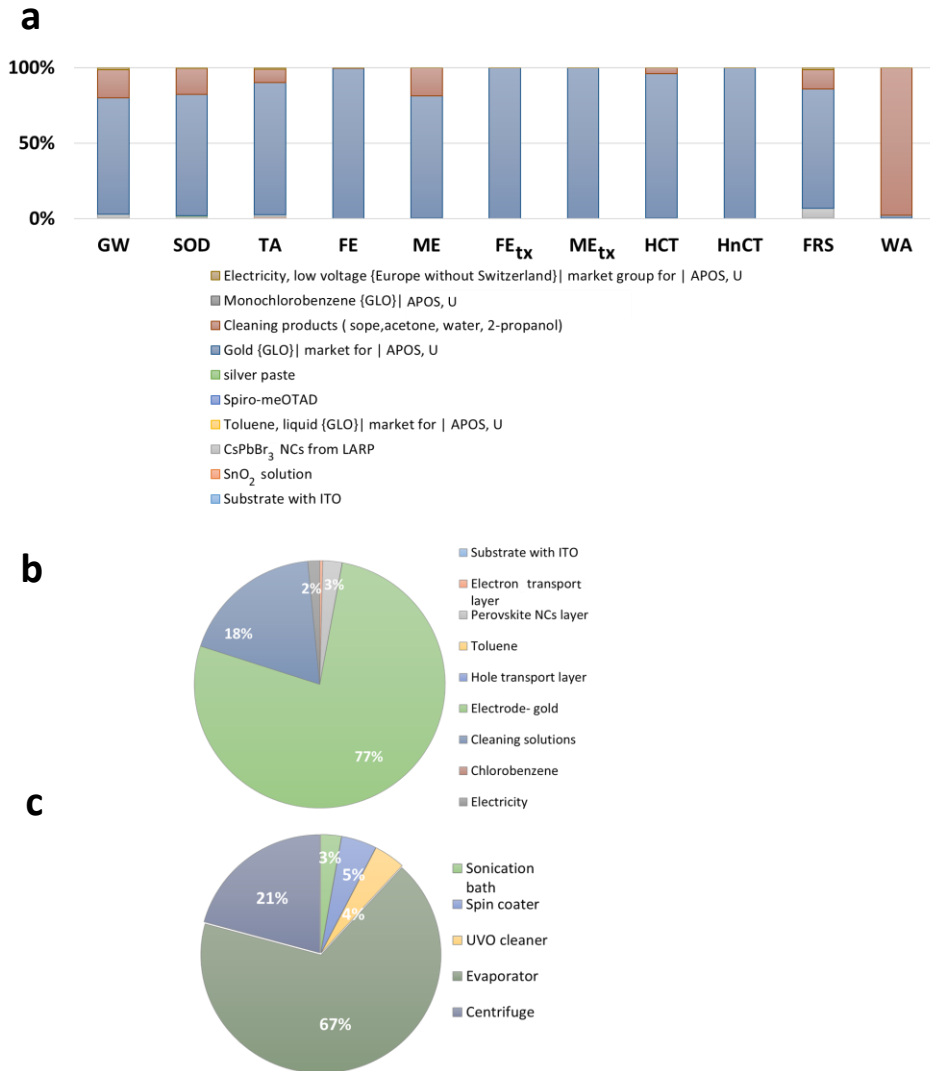88

Despite the small amount of gold used as the electrode, its impact compared to other layers is still the highest. Based on our modeling of the perovskite solar cell, gold indeed has the largest contribution to the impact categories related with human health. Together with its high costs, this is one of the reasons why strong efforts have been made in identifying suitable replacement materials for gold as electrode in perovskite solar cells by other metals (less expensive) or, e.g., carbon (see Chapter 3). Besides gold, the cleaning components have an important impact. By the term "cleaning components", we conjoined the impact of acetone, 2-propanol, soap, and water. Perovskite NCs, as itself, do not contribute significantly to the global emission, which is a positive result for mass production.

The total contribution to global warming from making one laboratory-level device is 1.95 kg CO_2 eq. (**Figure 4.9.b**). The highest contribution is from gold (77%), followed by the contribution of solvents for cleaning, with 18% in total. All other parameters together contribute less than 5%. These results can be a good direction for further research in perovskite solar cells.

For the manufacturing of the solar cells, we used the following equipment:

- Sonication bath (Branson M2800)
- Spin coater (due to the lack of information we modeled a G3P-8 spin coater (Cookson Electronics)
- UV-ozone cleaner (Jelight UVO Cleaner Model 144AX-220)
- Evaporator (Dutch homemade)
- Hot plate (IKA RCT basic)
- Evaporator and spin coater are using vacuum pumps
- Centrifuge machine (modeled in M-Diagnostic)

Electricity consumed during the entire process has some contribution to ionizing radiation. Energy consumption for each device is calculated based on the formula $E = P_{max} t C$, where P_{max} is the maximum power of a device, t the consumption time, and C the correction factor (percentage of usage of maximum power for a certain process). Most energy is consumed in thermal metal (gold) evaporation. In thermal evaporation, a solid metal (in this case gold) is thermally vaporized in a high vacuum and deposited as a solid on the substrate surface. This process requires high power to melt and vaporize gold and to reach a high vacuum (<10^{-6} mbar). The impacts of cooling down the system and consumption of N_2 in the glove box are neglected since the glove box is not only used for the purpose of evaporation. Centrifugation is important for obtaining good solutions. The use of a spin coater, UV-ozone cleaner, and sonication bath have a similar, and overall, not high impact on the total energy consumption. The largest impact to global warming, regarding energy consumption, comes from thermal evaporation (**Figure 4.9.c**). This is followed by the impact coming from the use of the centrifuge machine.

a

Legend for a:
- Electricity, low voltage {Europe without Switzerland}| market group for | APOS, U
- Monochlorobenzene {GLO}| APOS, U
- Cleaning products (sope,acetone, water, 2-propanol)
- Gold {GLO}| market for | APOS, U
- silver paste
- Spiro-meOTAD
- Toluene, liquid {GLO}| market for | APOS, U
- CsPbBr$_3$ NCs from LARP
- SnO$_2$ solution
- Substrate with ITO

b

Legend for b:
- Substrate with ITO
- Electron transport layer
- Perovskite NCs layer
- Toluene
- Hole transport layer
- Electrode- gold
- Cleaning solutions
- Chlorobenzene
- Electricity

c

Legend for c:
- Sonication bath
- Spin coater
- UVO cleaner
- Evaporator
- Centrifuge

Figure 4.9. a) Impact analysis of solar cell manufacturing. **b)** Contribution to global warming from solar cell manufacturing. **c)** Contribution to global warming from the equipment used in solar cell manufacturing.

4.6. Conclusion

A LCA was conducted on CsPbBr$_3$ perovskite NCs and perovskite solar cells that use NCs as a photoactive layer. The manufacturing process was broken down into two directions: NCs production and solar cell production. Both were

90

evaluated in a cradle-to-gate assessment. This has assisted in identifying significant issues within the process, which are large contributors to the environmental impact of components.

The results show that for lead bromide, lead contributes most in the impact categories. For CsPbBr$_3$ NCs, the largest contribution comes from other materials. With the LARP technique, 2-propanol is found to have the most impact and in the HI method, octadecene. By comparing the contributions to emission for the same types and amounts of NCs (1 kg of CsPbBr$_3$) produced *via* HI or LARP, LARP has a much lower environmental impact. LARP has in almost all categories (small exceptions are fossil resource scarcity and fresh water ecotoxicity) less impact, compared to HI. This result is important for up-scaling processes to an industrial level. Most contributions come from materials.

A LCA of perovskite solar cells is not completely new in the LCA community, which means that it was possible to find in modeling parameters for some layers in the literature. For other layers, including NCs, and energy requirements, the modeling was presented here. The results show that the thermally evaporated gold electrode has the most impact, despite the small amount used, followed by the hole transport layer (Spiro-OMeTAD). Gold is an expensive material, and its mining is dangerous for human health. From a cost and impact point of view, identifying suitable replacement materials for the gold electrode are therefore much needed. Next to gold, the cleaning solvents used in making the cells have an important impact. Perovskite CsPbBr$_3$ NCs do not considerably contribute to global emission. Most energy in the cell fabrication is consumed by metal (gold) evaporation. This process requires high power for melting and reaching high vacuum ($<10^{-6}$ mbar).

4.7. References

1.   Delbeke, J., Runge-Metzger, A., Slingenberg, Y. & Werksman, J. The Paris Agreement. in *Towards a Climate-Neutral Europe* 24–45 (Routledge, 2019).

2.   Nygren, J. *et al. Handbook on Life Cycle Assessment. Buisness Strategy and The Environment* vol. 15 (2004).

3.   The International Standards Organisation. *INTERNATIONAL STANDARD assessment — Requirements and guilelines. The International Journal of Life Cycle Assessment* vol. 2006 (2006).

4.   Gong, J., Darling, S. B. & You, F. Perovskite photovoltaics: Life-cycle assessment of energy and environmental impacts. *Energy Environ. Sci.* **8**, 1953–1968 (2015).

5.   Khalifa, S. A., Spatari, S., Fafarman, A. T. & Baxter, J. B. Environmental Sustainability of Mixed Cation Perovskite Materials in Photovoltaics Manufacturing. *ACS Sustain. Chem. Eng.* **8**, 16537–16548 (2020).

6.   Wickerts, S. *et al.* Prospective Life-Cycle Modeling of Quantum Dot Nanoparticles for Use in Photon Upconversion Devices. *ACS Sustain. Chem. Eng.* **9**, 5187–5195 (2021).

7.   Baldassarri, C., Shehabi, A., Asdrubali, F. & Masanet, E. Energy and emissions analysis of next generation electrochromic devices. *Sol. Energy Mater. Sol. Cells* **156**, 170–181 (2016).

8.   García-Valverde, R., Cherni, J. A. & Urbina, A. Life cycle analysis of organic photovoltaic technologies. *Prog. Photovoltaics Res. Appl.* **18**, 535–558 (2010).

9.   Gentile, A. A., Rocco, C., Modeo, S. & Romano, T. Gold recovery from thin film deposition facilities: environmental aspects of a novel method. *J. Clean. Prod.* **83**, 473–482 (2014).

10.   Protesescu, L. *et al.* Nanocrystals of Cesium Lead Halide Perovskites (CsPbX$_3$, X = Cl, Br, and I): Novel Optoelectronic Materials Showing Bright Emission with Wide Color Gamut. *Nano Lett.* **15**, 3692–3696 (2015).

11.   Akkerman, Q. A. *et al.* Strongly emissive perovskite nanocrystal inks for high-voltage solar cells. *Nat. Energy* **2**, 16194 (2016).

5

Wide-bandgap perovskite *p–i–n* solar cells

Abstract

By eluding thermalization and transmission losses, all-perovskite triple-junction solar cells are a potential low-cost strategy to achieve photovoltaic power conversion efficiencies of up to 37%. For a successful triple-junction solar cell, three complementary photovoltaic materials must be combined to achieve optimized current matching and minimal open-circuit voltage (V_{OC}) losses in each sub-cell. Presently, the biggest limitation to an efficient triple-junction stack comes from limitations of the wide-bandgap sub-cell, which is typically composed of a mixed-halide lead perovskite. This chapter describes the development of a stable and improved wide-bandgap *p–i–n* single-junction solar cell based on a $CsPbI_{1.5}Br_{1.5}$ perovskite. To slow down crystallization kinetics and improve perovskite film morphology, different concentrations of methylammonium chloride are introduced as an additive to the perovskite precursor solution. An electron transport bilayer, consisting of [6,6]-phenyl-C_{61}-butyric acid methyl ester (PCBM) with C_{60} on top, improves the photovoltaic performance as compared to single electron transport layers of C_{60} or PCBM, especially regarding the V_{OC}. Optimized devices have good stability and reproducibility. The champion device has an efficiency of 9.9%, with a V_{OC} of 1.23 V. This is one of the highest reported for wide-bandgap inorganic perovskite in a *p–i–n* device configuration.

5.1. Introduction

Despite their rapid development in the past decade resulting in a record power conversion efficiency (PCE) of 25.8% (certified 25.5%)[1], the PCE of perovskite single-junction solar cells will be constrained by the detailed balance limit[2]. This limitation originates from thermalization and transmission losses. When the photon energy is higher than the bandgap (E_g), excess energy is released as a thermalization loss. In contrast, when the photon energy is lower than the bandgap, transmission of light occurs. A straightforward way to elude these effects is to combine two or more complementary light-absorbing layers in a multi-junction solar cell. With appropriate bandgaps, the inherent energy losses of single-junction devices can be suppressed and efficiency limits rise from circa 34% to 68% in unconcentrated sunlight[3]. Fabrication of multi-junction solar cells is, however, a complex task because different materials need to be deposited in thin and conformal layers on top of each other *via* solution or vacuum based deposition techniques, without affecting underlying sub-cells. Besides potential problems in processing, intrinsic problems have to be taken into account such as maximizing absorption and radiative efficiency, while simultaneously minimizing parasitic absorption and interfacial losses.

Ideally, triple-junction perovskite solar cells are made by combining three sub-cells with a wide (~2.04 eV), intermediate (~1.58 eV), and narrow (~1.22 eV) bandgap, stacked on top of each other in such a way that the sub-cell with the widest bandgap faces the sun[4]. These optimal bandgaps are based on the narrowest bandgap of ~1.22 eV presently known for (mixed lead-tin) perovskites.

In a triple-junction solar cell, the front wide-bandgap sub-cell should preferably absorb all photons with an energy equal to or larger than its bandgap, transmitting the less energetic photons to the middle sub-cell. In the same fashion, the middle intermediate-bandgap sub-cell should absorb all photons with energies equal to or larger than its bandgap and transmit the remaining photons to the narrow-bandgap sub-cell. For a successful triple-junction solar cell with a two-terminal configuration, it is important to balance light absorption in the three complementary sub-cells to optimize current matching and minimize open-circuit voltage (V_{OC}) losses.

Metal halide perovskite semiconductors are an attractive candidate for multi-junction solar cells, mostly because of their easy tunable bandgap, from 1.2 up to 3.0 eV[5,6], and their simple and low-cost processing. Besides making all-perovskite multi-junction solar cells,[7] perovskites can also be used in hybrid tandem architectures with copper indium gallium selenide (CIGS) or crystalline silicon (c-Si)[8]. Theoretical calculations suggest that the PCE of all-perovskite multi-junction cells can easily surpass 30%[3,9]. In the past few years, research in all-perovskite tandems (i.e., with two complementary absorbers) has shown rapid progress and high PCEs, with a record of 26.4% have been reported[10].

94

Theoretical work, provided by Hörantner et al. shows that triple-junction (i.e., with three complementary absorbers) perovskite solar cells have the potential to have a PCE up to 37%[4], but reported values are much lower so far (20.1%)[7].

Presently, the main hurdle in improving the PCE of triple-junction perovskite solar cells is caused by limitations of the wide-bandgap sub-cell, typically composed of a mixed-halide perovskite. The bandgap of mixed-halide lead perovskites $APb(I_{1-x}Br_x)_3$ (A = methylammonium (MA$^+$), formamidinium (FA$^+$), Cs$^+$, or combinations thereof) can be easily tuned from 1.48 to 2.35 eV[11], by changing the A cation or the I to Br ratio. The presence of organic cations (MA$^+$, FA$^+$) causes relatively poor thermal stability and high sensitivity to humidity. The use of even a small percentage of cesium ions (Cs$^+$) can enhance thermal stability[12] and complete replacement of organic cations by Cs$^+$ is expected to induce long-term stability. Cs$^+$ cations can interact with the negatively charged defects in the perovskite, therewith improving device efficiency. On the other hand, the Cs$^+$ ion is not large enough to stabilize the perovskite crystal structure and the desirable black perovskite phase can transform into a non-emitting, non-perovskite, yellow orthorhombic phase. The challenge is to achieve a good combination of bandgap, photovoltaic performance, and stability by adjusting the cation and halide components and processing conditions.

CsPbI$_3$ is the most studied inorganic perovskite as it has a bandgap of 1.73 eV, which makes it an ideal candidate for perovskite tandem solar cells[13]. However, due to the lack of stability of the black perovskite phase under environmental conditions, the use of CsPbI$_3$ is limited. Substituting iodide by bromide helps with perovskite phase stabilization, but the wide bandgap of CsPbBr$_3$ (E_g = 2.3 eV) limits device efficiency. Inorganic mixed-halide perovskites, such as CsPbI$_2$Br and CsPbIBr$_2$, can offer the required balance between bandgap and stability, but are still suffering from easy transformation to the non-perovskite δ-phase or limited PCE, respectively. As an intermediate between these two most investigated mixed-halide perovskites, CsPbI$_{1.5}$I$_{1.5}$, may be expected to balance stability and efficiency. Thermal instability, sensitivity to humidity, phase instability, and ion migration are the main challenges to be solved before perovskite solar cells can be called stable.

The bandgap of mixed-halide perovskites shows a linear relationship with the I to Br ratio[14]. Unfortunately, for wider-bandgap perovskites the V_{OC} is not increasing proportionally with the increase in bandgap[5]. The larger V_{OC} losses for wider bandgaps currently limit the PCE. For perovskites with a bandgap above 1.85 eV, a considerable loss in V_{OC} is noticed when comparing experimental results to the theoretical limits[5]. This loss is even more pronounced when solar cells are in an inverted p–i–n structure, as compared to the n–i–p structure. Recent work on the most popular inorganic mixed-halide perovskites, CsPbI$_2$Br and CsPbIBr$_2$, shows a large difference in V_{OC} depending on the device architecture. One of the highest reported V_{OC}s for CsPbI$_2$Br in a p–i–n

architecture is 1.13 V[15], while the best one reported for a *n–i–p* architecture is 1.42 V[16]. Recently reported values for CsPbIBr$_2$ are 1.28 V[17] and 1.22 V[18] for *n–i–p* and *p–i–n*, respectively. Grischek et al.[19] studied the mismatch between the quasi-Fermi level splitting (QFLS) and the V_{OC} for CsPbI$_2$Br in *n–i–p* and *p–i–n* structures. The QFLS is the energy difference that occurs between the Fermi levels of the electrons and the holes when a semiconductor is out of equilibrium, e.g., caused by illumination or by passing an electrical current. For a semiconductor that is excited by light, the QFLS is related to the natural logarithm of the product of photogenerated electron and hole densities relative to the intrinsic carrier concentration squared[20]. In a solar cell, the QFLS is a direct measure of the V_{OC}. The QFLS can be measured optically by fitting the generalized Planck equation to the high-energy edge of the absolute photoluminescence (PL) spectrum (see Methods). In a highly optimized solar cell, the V_{OC} of the cell and QFLS of the semiconductor without any charge transport layers and contact, can have the same value, but in most solar cells a mismatch is seen. The mentioned study[19] revealed that in the *n–i–p* structure, losses in the QFLS are caused by similar contributions from the charge transport layers (for electrons and holes), while in *p–i–n* solar cells, the main losses are caused by the electron transport layer (ETL). Energy level misalignment might be a possible reason for the large mismatch in *p–i–n* solar cells.

Because higher performance can be achieved, the normal *n–i–p* structure is probably the most reported structure for wide-bandgap single-junction perovskites. On the contrary, the most reported configuration for all-perovskite multi-junction solar cells is *p–i–n.* In early reports on monolithic multi-junction perovskite solar cells by Mailoa et al.[21] and Albrecht et al.[22], cells were made in a *n–i–p* configuration, with PCEs below 15%. The short-current density (J_{SC}) of *n–i–p* tandems is mostly limited by broad parasitic absorption of the doped hole transport layer (HTL) (Spiro-OMeTAD). Until now, it has been hard to find a good replacement with lower parasitic absorption as compared to Spiro-OMeTAD. The first reported work on tandem solar cells in the inverted *p–i–n* configuration already surpassed 23% efficiency[23,24,25]. The inverted architecture is, so far, the only one used to successfully fabricate all-perovskite triple-junction solar cells[7,26]. Besides, the higher efficiencies for multi-junction solar cells, another favorable aspect of the *p–i–n* structure is the lower temperatures needed to fabricate the cells. For multi-junction solar cells, it is generally important to avoid high-temperature processing steps to limit the thermal budget on previously deposited sub-cells and thereby prevent degradation.

This chapter focuses on the development of a stable and improved *p–i–n* single-junction solar cell, based on a mixed-halide wide-bandgap perovskite, CsPbI$_{1.5}$Br$_{1.5}$, intended for future use in for triple-junction cells. The *p–i–n* cells are built on a glass substrate covered with indium tin oxide (ITO), by sequentially depositing the HTL, the perovskite, the ETL, and completing the stack with a thermally evaporated metal contact. The performance and stability of the wide-

bandgap single-junction is improved by engineering the perovskite precursor. The proper choice of charge transport layers, together with the perovskite film quality, play a vital role in obtaining successful devices. Control of the crystallization and solvent evaporation rates is vital to ensure high quality, flat, and compact, perovskite films. Controlling the morphology, by annealing and using different antisolvents and/or additives, is found to improve the perovskite and the interface between perovskite and charge transport layers. Improved film morphology and energy alignment among layers is found to significantly reduce V_{OC} losses.

5.2. Results

5.2.1. Preparation and characterization of wide-bandgap CsPbI$_{1.5}$Br$_{1.5}$ perovskite thin films

Perovskite thin films were prepared using an one-step, antisolvent deposition strategy, followed by thermal gradient annealing. The process is presented in **Figure 5.1.** A CsPbI$_{1.5}$Br$_{1.5}$ precursor solution was prepared in a solvent mixture of dimethyl sulfoxide (DMSO) and *N,N*-dimethylformamide (DMF), and stirred overnight at 60 °C. Solutions prepared in pure DMSO faced problems with substrate wettability. DMF was added to achieve better substrate coverage. A set of experiments showed that the best combination of solubility and wettability, is achieved when DMSO and DMF are mixed in a ratio of 1.8:1. DMSO has a major impact on enlarging the grain size and DMF adjusts the surface energy and volume change of the precursor solution[27]. The precursor solution was spin coated on a substrate with spin speeds of 600 rpm for 5 s and 3000 rpm for 30 s. In the last 10 s an antisolvent was applied. A suitable antisolvent must meet several criteria related to the boiling point, vapor pressure, dipole moment, and water solubility[28]. Different solvents, such as chlorobenzene, ethyl acetate, methyl acetate, 2-propanol, acetone, and anisole were tried. For the inorganic CsPbI$_{1.5}$Br$_{1.5}$ perovskite, methyl acetate (MeOAc) is the most suitable candidate due to its low boiling point (56.9 °C) and high vapor pressure (0.23 bar at 20 °C). Immediately after spin coating, films were transparent with red reflection, suggesting that nucleation started by the antisolvent treatment. As prepared films are transferred to a hotplate for thermal annealing.

Thermal annealing of perovskite films is commonly used to volatilize residual solvent and influence film morphology. Annealing time and temperature affect the crystallization process[29]. High annealing temperatures increase the rate of solvent evaporation and lead to the formation of smaller grains, increasing the number of grain boundaries and resulting in a higher density of non-radiative recombination centers[27]. It has been shown that so-called gradient annealing, i.e., annealing in steps, is the best approach for controlling nucleation and crystal

growth in inorganic lead halide perovskites[30]. Films become red within the first minute of annealing when moved to the first temperature (35 °C), and darker and redder once when moved to the higher temperature (120 °C). An additional annealing step at the highest temperature (165 °C) does not seem to affect the crystallization itself, but it is introduced to remove residual (high boiling) solvents. The prepared perovskite films have an average thickness of 250 nm and roughness of less than 10 nm.
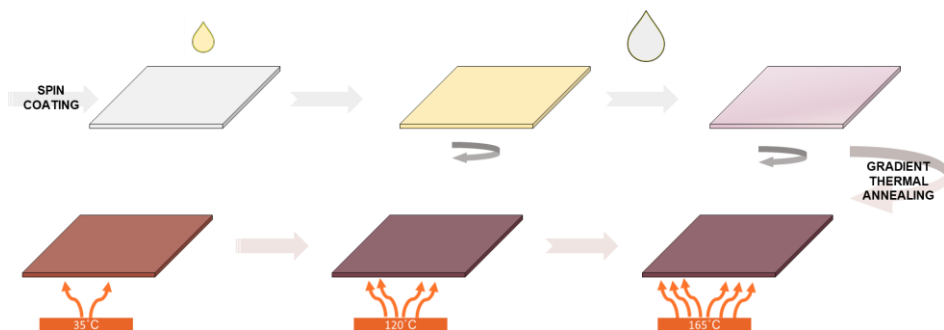
Figure 5.1. Schematics of deposition and annealing of mixed-halide perovskite thin films. A lead halide precursor solution (in a mixture of DMSO and DMF) is deposited on a substrate and followed up by spin coating with speeds of 600 rpm for 5 s and 3000 rpm for 30 s. In the last 10 s methyl acetate is applied as antisolvent. The film is thermally annealed at three temperatures: 35 °C (5 min), 120 °C (10 min), and 165 °C (5 min), yielding the perovskite film.

X-ray diffraction (XRD) confirms the formation of the perovskite phase, with (110) and (220) reflections at 14.8° and 29.8° (**Figure 5.2.a**). The UV-vis-NIR absorption spectrum shows that the material has a wide bandgap of ~2.05 eV (**Figure 5.2.b**), which is nearly ideal bandgap for the top sub-cell in an all-perovskite triple-junction solar cell. Under ambient conditions, the optical absorption remained unchanged for almost one hour (**Figure 5.2.b**). This is one of the first clues of the high stability of the perovskite films. The surface morphology was characterized by scanning electron microscopy (SEM) (**Figure 5.2.c** and **5.2.d)**. Closed films are formed with crystalline grains with a size of around 500 nm. The few bright crystals observed in the SEM images and a low-intensity XRD peak at 13.3°, suggest a low level of unreacted PbI_2 precursor. The results suggest that it is possible to use these films as an absorbing layer in a solar cell.

5.2.2. Single-junction wide-bandgap $CsPbI_{1.5}Br_{1.5}$ solar cells

Solar cells were prepared using $CsPbI_{1.5}Br_{1.5}$ as a photoactive layer in a *p–i–n* architecture, since it is the most compatible for further application in triple-junction solar cells. Commonly used HTLs such as poly[bis(4-phenyl)(2,4,6-trimethylphenyl)amine (PTAA) and poly(3,4-ethylenedioxythiophene) polystyrene

sulfonate (PEDOT:PSS) were a poor choice for the perovskite of our interest. When the perovskite precursor solution was spin coated on top of a PTAA layer, the hydrophobic nature of PTAA led to poor surface wetting and incomplete coverage of the perovskite films. To avoid electrical shunts, deposition on PTAA was abandoned. On PEDOT:PSS, the surface coverage was improved, but devices were working poorly and the reproducibility was poor.
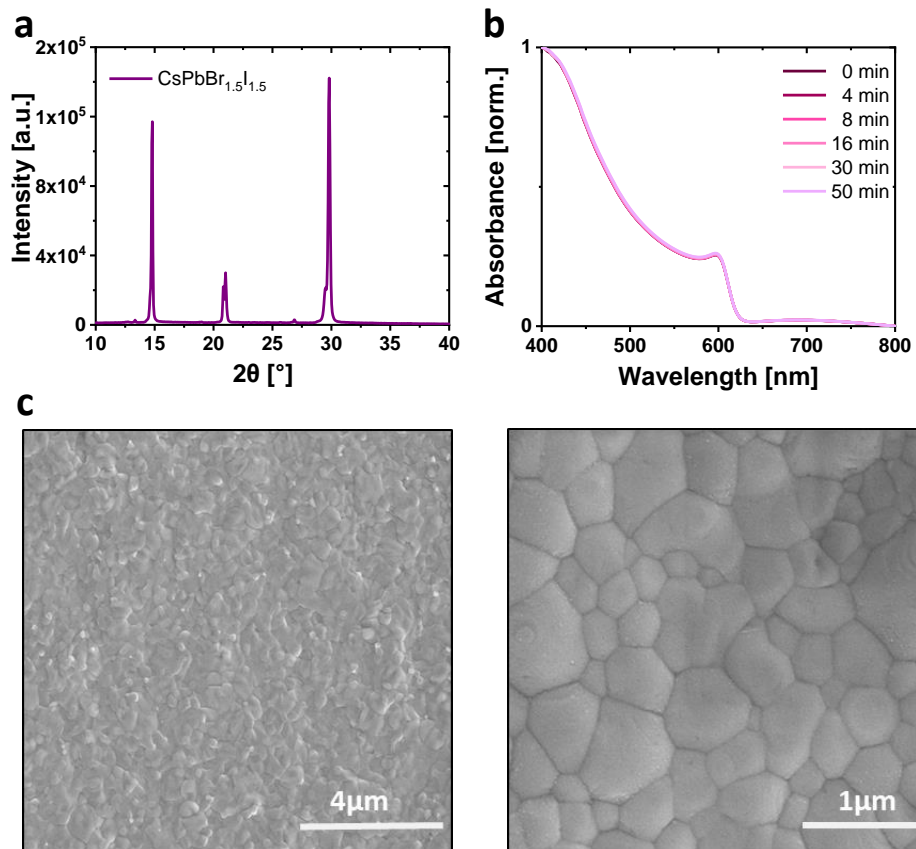
Figure 5.2. CsPbI$_{1.5}$Br$_{1.5}$ thin film characterization. a) XRD pattern confirming formation of the perovskite phase. **b)** UV-vis-NIR absorption spectrum indicating optical bandgap of ~2.05 eV, ideal for triple-junction solar cells and good stability of films kept in ambient air. **c)** SEM top-view image showing closed films with grain size around 500 nm. Scale bar is 4 µm (left)**.** Same at higher magnification, scale bar is 1 µm (right).

Instead, a HTL consisting of a self-assembled monolayer of [2-(9*H*-carbazol-9-yl)ethyl]phosphonic acid (2PACz) provided good surface coverage and yielded stable and reproducible devices. Fabrication involved deposition of 2PACz by solution processing on an ITO-covered glass substrate, followed by

thermal annealing at 100 °C for 10 min. 2PACz easily binds to the ITO surface *via* the phosphonic acid anchoring groups,[31] has a low material requirement for spin coating (only 0.335 mg/mL), and low parasitic optical absorption[32]. The CsPbI$_{1.5}$Br$_{1.5}$ perovskite layer was fabricated *via* one-step spin coating using MeOAc as antisolvent, followed by gradient thermal annealing (35 °C for 5 min → 120 °C for 10 min → 165 °C for 5 min) as described in section 5.2.1. Thermally evaporated C$_{60}$ and solution processed [6,6]-phenyl-C$_{61}$-butyric acid methyl ester (PCBM) were investigated as ETL, mostly owing to the ability of fullerene derivatives to effectively extract electrons. Evaporation of C$_{60}$ was followed by thermal evaporation of bathocuproine (BCP) (8 nm) and an Al (100 nm) metal electrode. BCP improves the V_{OC}, fill factor (FF), and reduces hysteresis[33,34,35,36]. For the PCBM ETL, we used LiF (1 nm) and Al (100 nm) as electrode. We determined the optimal thickness for evaporated C$_{60}$ ETLs and compared it to a solution-processed PCBM ETL. **Figure 5.3.a** shows the current density-voltage (*J–V*) characteristics of devices with different C$_{60}$ layer thicknesses (20 – 80 nm) and the comparison with a 80-nm solution-processed PCBM layer.

With increasing C$_{60}$ thickness from 20 to 40 nm, the *J–V* characteristics show that the photovoltaic (PV) performance improved, mainly by reducing the shunt resistance. However, from 40 to 80 nm there is no evident change. The low shunt resistance of devices with 20 or 30 nm C$_{60}$, may point to the presence of small pinholes in the CsPbI$_{1.5}$Br$_{1.5}$ layer, which can cause a shunt between bottom and top electrodes if not separated by a sufficiently thick ETL. Average device performances for devices with 40 nm C$_{60}$ are summarized in **Table 5.1.** and representative *J–V* characteristics are shown in **Figure 5.3.b**.

Table 5.1. Photovoltaic performance of $E_g = 2.05$ eV single-junction perovskite solar cell (corresponding *J-V* curve is presented in **Figure 5.3.b**)

Scan direction	V_{OC} (V)	FF	J_{SC} (mA/cm^2)	PCE (%)
Reverse	1.03	0.55	9.71	5.51
Forward	0.91	0.38	9.62	3.30

The *J–V* characteristics and corresponding photovoltaic parameters reveal substantial difficulties and leave room for significant improvement. For instance, the *J–V* characteristics show a poor FF and large hysteresis between forward and reverse scan directions. An "s-shape" is present in the *J–V* curve which indicates improper charge extraction. This is probably caused by trap states at the interface between the perovskite and charge transport layers where charges accumulate and increase the recombination resistance[37]. The most critical parameter is the V_{OC} (1.03 V in a reverse scan), which is much lower than the theoretical detailed-balance limit. For a bandgap of 2.05 eV, the detailed-balance limit for the V_{OC} is 1.73 V[20], indicating an additional V_{OC} loss of ~0.7 V in

the devices. Reduction of the non-radiative recombination losses, *via* better alignment of the charge transport layers (efficient charge carrier transport and extraction), surface passivation, and additive engineering will increase V_{OC}.
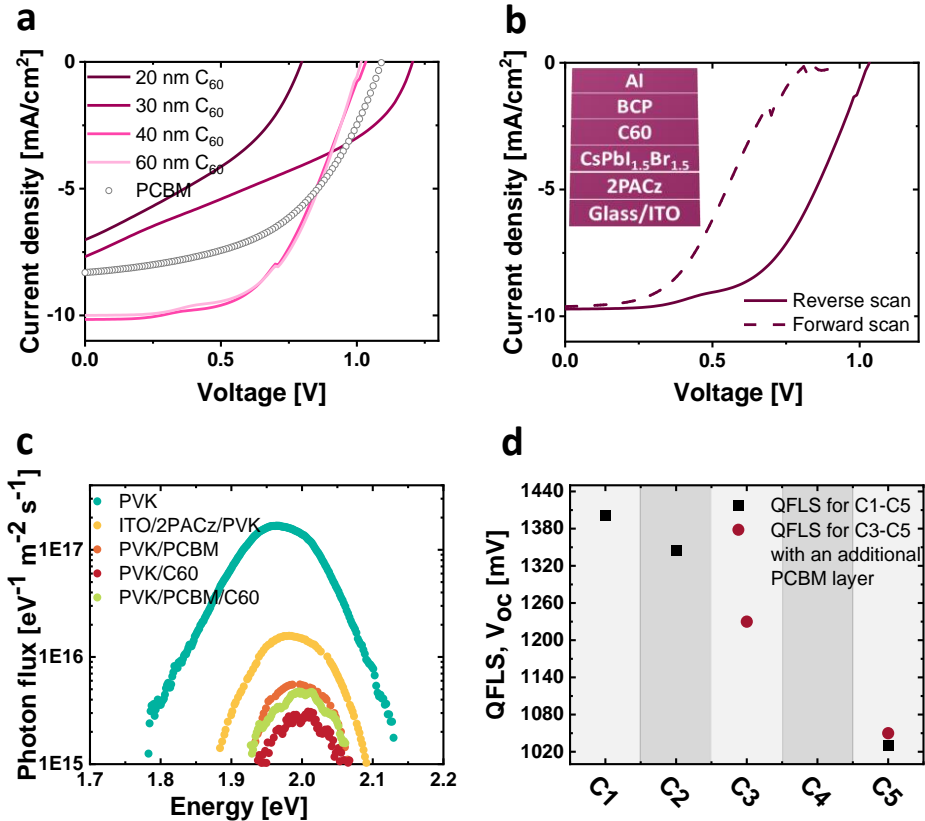
Figure 5.3. Device characteristics and layer-by-layer V_{OC} loss analysis. a) Current density versus voltage (*J-V*) curves of representative single-junction $CsPbI_{1.5}Br_{1.5}$ (E_g = 2.05 eV) solar cells, with C_{60} or PCBM as ETL. The best performing devices have a 40 nm C_{60} layer. **b)** Forward and reverse *J-V* curves of the device with the structure glass/ITO/2PACz/$CsPbI_{1.5}Br_{1.5}$ (250 nm)/C_{60} (40 nm)/BCP (8 nm)/Al (100 nm). **c)** Absolute photoluminescence (PL) spectra of perovskite films deposited in different configurations. The perovskite film on glass is the most emissive layer and each additional layer leads to a decrease in the intensity of the PL emission. **d)** Quasi-Fermi level splitting data from absolute PL spectra in panel c). C1: configuration glass/$CsPbI_{1.5}Br_{1.5}$; C2: configuration glass/ITO/2PACz/$CsPbI_{1.5}Br_{1.5}$; C3: configuration glass/$CsPbI_{1.5}Br_{1.5}$/C_{60}; C4: configuration glass/ITO/2PACz/$CsPbI_{1.5}Br_{1.5}$/C_{60}; C5: V_{OC} from the cell with structure glass/ITO/2PACz/$CsPbI_{1.5}Br_{1.5}$/C_{60}/BCP/Al. Black squares represent values for the mentioned configurations and the red circles represent values for C3: configuration glass/$CsPbI_{1.5}Br_{1.5}$/PCBM/C_{60}; C4: configuration glass/ITO/2PACz/ $CsPbI_{1.5}Br_{1.5}$/PCBM/C_{60}; C5: V_{OC} from the cell structure glass/ITO/2PACz/$CsPbI_{1.5}Br_{1.5}$/PCBM/C_{60}/BCP/Al.

Losses in the V_{OC} compared to the detailed-balance limit are caused by non-radiative recombination of electrons and holes, e.g., occurring in the bulk of the perovskite or at the interface of the perovskite with an ETL or HTL. To remedy voltage losses, it is important to understand what exactly causes the non-radiative recombination and reveal the contribution of each element in the perovskite solar cell. This can be achieved optically by determining the QFLS via measuring the absolute PL spectrum. By analyzing the QFLS for different stack configurations the contribution of bulk and interfacial losses can be determined.

Figure 5.3.c shows that the perovskite film on glass is the most emissive layer and adding an HTL or ETL leads to a significant decrease in the intensity of the PL emission. When C_{60} is used as ETL, the PL signal is barely detectable, but the intensity improves when PCBM is used, either as a single layer, or as a PCBM/C_{60} bilayer. The intensity of the PL signals for the latter two do not differ significantly, indicating that the PCBM layer is covering the perovskite film well. **Figure 5.3.d** summarizes the estimated values for the QFLS. The QFLS of a $CsPbI_{1.5}Br_{1.5}$ film on glass is 1.40 V, which already represents a ~0.33 V loss compared to the detailed balance limit. When coated on an ITO/2PACz hole selective contact, the QFLS further decreases, by ~60 mV to 1.34 V. This implies that a small additional loss occurs at the perovskite/HTL interface. Deposition of C_{60} as ETL on the $CsPbI_{1.5}Br_{1.5}$ surface, however, leads to an enormous drop in the PL intensity (**Figure 5.3.c)** from which no QFLS could be determined. This also holds for the glass/ITO/2PACz/$CsPbI_{1.5}Br_{1.5}$/C_{60} stack (**Figure 5.3.d**). The V_{OC} for the corresponding device was 1.03 V. This implies that the charge transport layers introduce an additional ~0.37 V V_{OC} loss, composed of ~0.06 V at the HTL and consequently ~0.31 V at the ETL, compared to the pristine perovskite layer. These results indicate that the most critical non-radiative losses are incurred in the perovskite bulk (~0.33 V) and additionally at the perovskite/ETL interface (~0.31 V).

Better energy alignment of charge transport layers and perovskite, usually achieved by introducing passivation layers, can lead to a higher V_{OC}. PCBM is an appropriate choice as ETL because of the higher-lying lowest energy unoccupied molecular orbital (LUMO) compared to C_{60}. The red markers in **Figure 5.3.d** show that after spin coating PCBM on the top of the perovskite, but before C_{60} evaporation, it is possible to determine a QFLS value at 1.23 V. This suggests that the PCBM/C_{60} bilayer introduces a V_{OC} loss of ~0.17 V. However, the V_{OC} measured for a device with a PCBM/C_{60} bilayer only slightly improved, from 1.03 V for the cell with C_{60} only to 1.05 V.

5.2.3. Additive engineering using methylammonium halides

The QFLS presented in the previous section indicates that significant non-radiative recombination is occurring in $CsPbI_{1.5}Br_{1.5}$ perovskite films on glass. This hints towards the need for an improved morphology which can possibly be

realized by additives that control the crystallization dynamics. Organic additives are widely used in wide-bandgap perovskites to improve the film morphology and passivate trap states[38]. Successful additive engineering in lead halide perovskites is related to coordination of the additive to the lead cation or the halide anion. Literature is in agreement that neither extremely fast nor extremely slow crystallization is favorable[39,40,41,42], but there is no general agreement on the crystallization rate and it has to be individually determined for each perovskite film.

To slow down the fast crystallization processes, we employed a set of methylammonium halides (MAX, X= Cl, Br, I) as additives to the perovskite precursor solution in two concentrations (10 and 20 wt% with respect to $CsPbI_{1.5}Br_{1.5}$). The effect of these three additives is rather different as can be seen in the SEM images of the top surface of the resulting films (**Figure 5.4.**). MAI reduced the crystallization rate, leaving rough and unclosed films. Films processed with MABr showed extremely slow crystallization, leaving some pinholes and unreacted precursors. The best films were made using MACl, providing a moderate crystallization speed, but still slower than without any additives (reference). These films were closed, homogenous, and had larger grains. Films with larger monolithic grains are expected to be more stable than films with a large distribution of nanocrystalline domains[43].
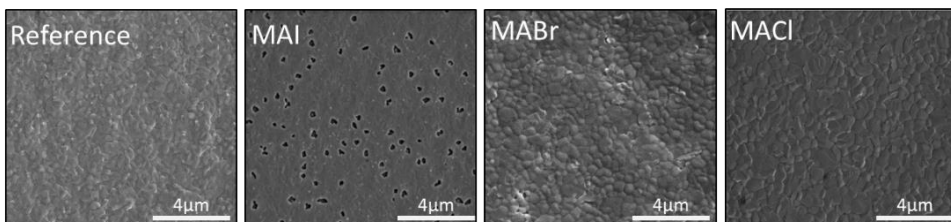
Figure 5.4. Surface morphology of $CsPbI_{1.5}Br_{1.5}$ films characterized by SEM. Images are shown for films processed without (reference film) and films processed with MAX (X= Cl, Br, I) additives (10 wt%). Additives change crystallization dynamics and film morphology. The scale bar is 4 µm.

Next, several concentrations of MACl as additive were evaluated: 5, 7, 10, 15, and 20 wt%. Films prepared from the reference perovskite precursor solution (0 wt% MACl) turned into red-magenta color at the first annealing temperature. When the amount of MACl was increased, obtaining a reddish film required more time. E.g., films processed with 20 wt% MACl turned from yellow to reddish, only after annealing at 165 °C. These visual changes are the first indicators of retarded crystallization. The surface morphology was characterized by SEM (**Figure 5.5.a**). For lower concentrations (5 and 7 wt%), substantial amounts of unreacted precursors are present on top of the films. The best surface morphology and grain sizes are obtained for 10 wt% films. At 15 wt%, the films

turned out to be rougher and have developed some pin holes. At 20 wt%, the films became very rough and showed large holes. With increasing MACl concentration, the bandgap narrows as shown by the red shift of the onset in the UV-vis-NIR absorption spectra (**Figure 5.5.b**). The *J-V* characteristics of the best-performing devices (**Figure 5.5.c**) point to a distinct improvement in the PV performance when the concentration of MACl increases, reaching the maximum for 10 wt%, but significantly dropping for 15 wt%. The major improvement for the 10 wt% sample are in the J_{SC}, FF, and absence of the "s-shape" and reduced hysteresis. To better understand the improved performance achieved when adding 10 wt% MACl to the $CsPbI_{1.5}Br_{1.5}$ precursor solution, we further analyzed the films and devices.
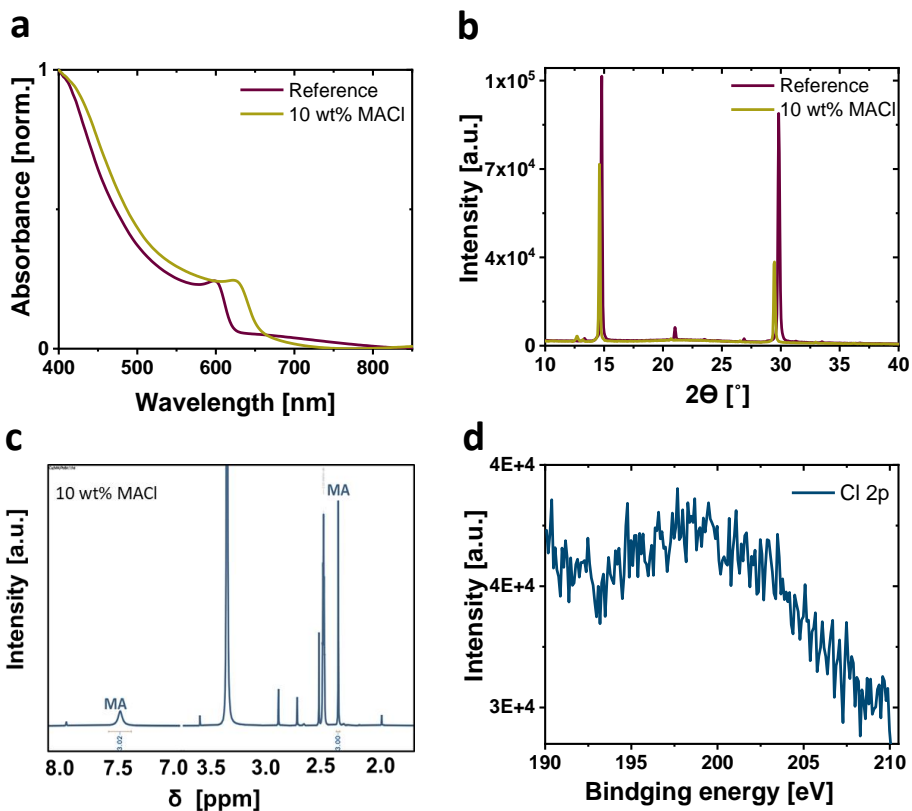
  Figure 5.6.a compares the UV-vis-NIR absorption spectra of perovskite films processed without (reference) and with 10 wt% MACl. The onset of the optical absorption red shifts when using 10 wt% MACl, indicating a bandgap reduction from ~2.05 to ~1.98 eV. This is accompanied by an expansion of the perovskite lattice, as marked by a shift of the (110) and (220) diffraction peaks to lower angles (**Figure 5.6.b**). The enlarged unit cell is likely caused by incorporation of methylammonium ($CH_3NH_3^+$) cations in the lattice. Nuclear magnetic resonance (NMR) spectra (**Figure 5.6.c**) recorded for a film that was dissolved in deuterated DMSO, displays peaks at δ = 2.4 and δ = 7.5 ppm, belonging to the $-CH_3$ and $-NH_3^+$ groups of MA^+, respectively, therewith validating the presence of MA^+ in the film. X-ray photoelectron spectroscopy (XPS) was used to assess the presence of Cl^-. The core level XPS spectra show a low signal of the Cl $2p$ electrons in the film (**Figure 5.6.d**), demonstrating that negligible levels of Cl^- are incorporated in the crystal lattice.

  The results suggest that the larger MA^+ is present in the perovskite lattice, but that Cl^- is virtually absent. Apparently, the smaller Cl^- ion cannot easily substitute the Br^- and I^- ions to become part of the crystal lattice. During the spin coating process, Cl^- is likely involved in the formation of the layer by affecting the crystallization dynamics, but it does not remain in the film. Due to its volatile nature it is released from the film during thermal annealing. From earlier reports it is known that the bandgaps of halide and mixed-halide $CsPbX_3$ and $MAPbX_3$ perovskites narrow when replacing Cs^+ by MA^+. For $CsPbI_3$ and $MAPbI_3$ from 1.73 to 1.61 eV,[13,44] for $CsPbI_2Br$ and $MAPbI_2Br$ from 1.92 to 1.71 eV,[45,46] for $CsPbIBr_2$ and $MAPbIBr_2$ from 2.05 to 1.93 eV, [46,41] and for $CsPbBr_3$ and $MAPbBr_3$ from 2.50 to 2.33 eV[46]. Hence, when introducing a larger A-cation (MA^+ vs. Cs^+) into the lattice, the bandgap narrows[47]. The A-cation in the perovskite lattice acts as template for the inorganic framework and can change the lead-halide (PbX_6) octahedra. One supposed explanation for such a phenomenon is that the red shift is a consequence of the breakdown of the Pb-halide octahedral symmetry, similar to the red shift observed in perovskite nanocrystals, due to the pressurization (See Chapter 2) [48,49,50]. It can be seen that the use of 10 wt% of MACl already

creates a significant reduction of the bandgap, which further evidences the incorporation of MA$^+$. The films will further be referred to as MA$_{1-x}$Cs$_x$PbI$_{1.5}$Br$_{1.5}$.

a

b

c
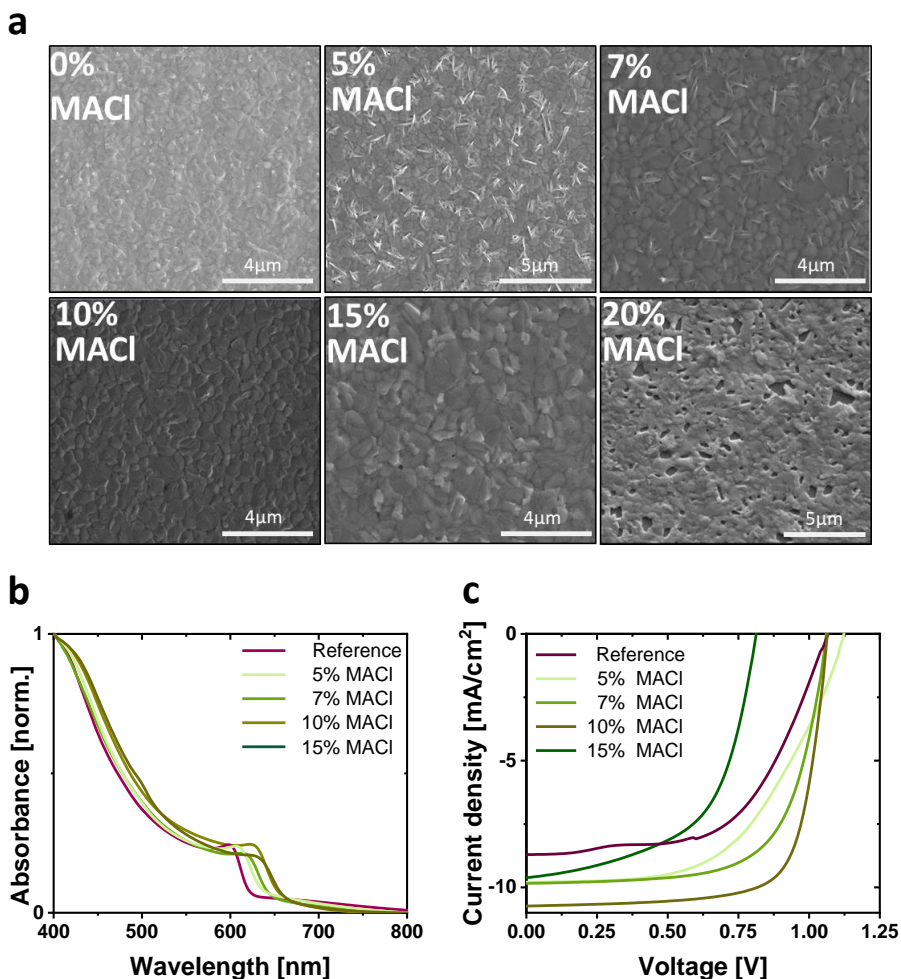
Figure 5.5. Characterization of CsPbI$_{1.5}$Br$_{1.5}$ films and devices, processed with 0, 5, 7, 10, 15, and 20 wt% of MACl. a) SEM images of CsPbI$_{1.5}$Br$_{1.5}$ films processed with different wt% of MACl added to the precursor solution (0 to 20 wt%). The best surface morphology and grain sizes are obtained for the 10 wt% films. **b)** UV-vis-NIR absorption spectra of perovskite films processed with different wt% MACl. With increasing MACl concentration, the bandgap narrows. **c)** *J-V* characteristics for glass/ITO/2PACz/CsPbI$_{1.5}$Br$_{1.5}$/C$_{60}$/BCP/Al solar cells processed with different concentrations of MACl. The best device is the one processed with 10 wt% MACl, showing a major improvement in *J*$_{SC}$ and FF.

Figure 5.6. Characterization of CsPbI$_{1.5}$Br$_{1.5}$ films processed with 10 wt% MACl. a) UV-vis-NIR absorption spectra. The absorption onset is red shifts when using 10 wt% MACl. **b)** X-ray diffractogram (films deposited on glass). The enlarged unit cell compared to the reference film indicates the expansion of the perovskite lattice. **c)** Nuclear magnetic resonance (NMR) spectrum with peaks at 2.4 (−CH$_3$) and 7.5 ppm (−NH$_3^+$) indicating the presence of MA$^+$ in the film. The quintet at 2.5 ppm is from DMSO-d5, the signal at 3.35 ppm is from H$_2$O. **d)** X-ray photoelectron spectroscopy (XPS) of Cl 2p electrons in the film showing a low signal coming from Cl$^-$.

5.2.4. Reducing the V_{OC} losses with PCBM/C$_{60}$ bilayer

While the film quality and device performance reached an optimum when using 10 wt% MACl as a processing additive, no major improvement was achieved for the V_{OC}. Nevertheless, some reduction of non-radiative recombination has occurred because the V_{OC} remained the same while the bandgap reduced from ~2.05 to ~1.98 eV. This also reduces the detailed-balance limit V_{OC} from ~1.73 V to ~1.66 V. In section 5.2.2. it was shown that next to losses that are intrinsic to the film quality, a significant loss in the V_{OC} can be attributed to recombination at the perovskite/C$_{60}$ interface. It is clear that the interface between the perovskite

106

and ETL must be carefully engineered and the use of PCBM emerged as an appropriate choice. To evaluate this, 20 nm of PCBM was spin coated on $MA_{1-x}Cs_xPbI_{1.5}Br_{1.5}$ and, without thermal annealing, directly followed by thermal deposition of 20 nm C_{60}. This effectively replaces the 40 nm C_{60} ETL with a 40 nm PCBM/C_{60} bilayer. The PCBM/C_{60} bilayer improves the device performance compared to PCBM-only and C_{60}-only ETLs, especially in terms of the V_{OC} (**Figure 5.7.a**). The increased V_{OC} is probably related to the higher-lying LUMO of PCBM compared to that of C_{60}. Earlier, it has also been argued that the PCBM/C_{60} bilayer facilitates charge transport because of the suppressing effect on the defects at the interface,[51,52] but this explanation is not compatible with the QFLS experiments shown in **Figure 5.3.d**.

Figure 5.7.a shows that a PCBM/C_{60} bilayer improves the performance of both the reference $CsPbI_{1.5}Br_{1.5}$ and the $MA_{1-x}Cs_xPbI_{1.5}Br_{1.5}$ perovskite solar cells. For $MA_{1-x}Cs_xPbI_{1.5}Br_{1.5}$ there is a major improvement in the V_{OC} when using PCBM in between the perovskite and the C_{60} layer (**Table 5.2.**). Interestingly, better performance and higher PCE (9.2%) were obtained in a forward scan. To our knowledge, this is one of the highest reported efficiencies for the inverted planar p–i–n stack with a $CsPbI_{1.5}Br_{1.5}$-based perovskite absorbing layer and the highest V_{OC} (1.23 V) for such cell (in inverted structure). The high V_{OC} and FF suggest that PCBM successfully reduced interfacial recombination and extraction losses. The combined effects of using MACl as additive and the PCBM/C_{60} ETL reduce the non-radiative V_{OC} loss for the 1.98 eV bandgap $MA_{1-x}Cs_xPbI_{1.5}Br_{1.5}$ solar cell to 1.66 – 1.23 = 0.43 V, i.e., significantly less than the 0.70 V loss found for the reference $CsPbI_{1.5}Br_{1.5}$ cell with a C_{60}-only ETL. These results confirm that the interface between the perovskite and ETL is crucial for the PV performance. Bulk and interface passivation are needed to further reduce traps in the perovskite at the interfaces, mitigate the effects of a rough surface, and better energetically align the energy levels of the charge transport layers with the valence and conduction bands of the perovskite.

The device statistics of $MA_{1-x}Cs_xPbI_{1.5}Br_{1.5}$ devices with PCBM/C_{60} as ETL indicate good reproducibility (**Figure 5.7.b**) with an average PCE of 8.7% (reverse) and 8.8% (forward). The external quantum efficiency (EQE) spectra of the best $MA_{1-x}Cs_xPbI_{1.5}Br_{1.5}$ device shows an onset at 625 nm, consistent with the absorption edge (**Figure 5.7.c**). The AM.15G- integrated J_{SC} (11.2 mA/cm^2) determined from the EQE spectrum is slightly higher than the measured values under the solar simulator conditions (10.4 mA/cm^2). Using this more accurate estimation of the J_{SC}, the PCE of the best cell is 9.9%, based on the forward scan.

Using highly sensitive photocurrent spectroscopy measurements, we studied changes in the sub-bandgap EQE to reveal information on the presence of defect states near and below the band edges (**Figure 5.7.d**). The shape of the sub-bandgap photocurrent spectra is affected by constructive and destructive interference of light in the device stack such that peak positions alter with layer

thickness[53]. The band edges show sharp onset for the $CsPbI_{1.5}Br_{1.5}$ and $MA_{1-x}Cs_xPbI_{1.5}Br_{1.5}$ devices. Below the bandgap, the feature at around 1.75 eV corresponds to the photocurrent contribution of PCBM. The $CsPbI_{1.5}Br_{1.5}$ cell shows higher EQE in the range between 1.0 and 1.5 eV, indicating a higher defect contribution. Additionally, the onset of the sub-bandgap EQE, somewhat arbitrarily defined as the energy where the EQE reaches 10^{-8}, is located at 1.21 eV for $CsPbI_{1.5}Br_{1.5}$ and shifted to 1.61 eV for $MA_{1-x}Cs_xPbI_{1.5}Br_{1.5}$. Because the bandgap is narrower, this indicates that the defect state in the bandgap becomes relatively shallower, which possibly lowers non-radiative recombination. By fitting the band edge to the EQE $\propto \exp((E_g - E)/E_U)$, it is possible to determine the Urbach energy (E_U) which is related to the energetic disorder of a semiconductor. The $CsPbI_{1.5}Br_{1.5}$ cell has $E_U = 20.8$ meV and this decreases to $E_U = 17.0$ meV, implying lower energetic disorder at the band edge. The contribution of PCBM overlaps with the band edge of the perovskite, which complicates the fitting and causes some uncertainty in E_U. For perovskites, E_U is typically in the range of 15 to 23 meV,[54,55] with the lower values indicating a higher quality films[56]. The presence of sub-bandgap electronic states results in reduced PV performance and V_{OC},[57] wherein a higher E_U leads to a loss in the V_{OC}.

Table 5.2. Photovoltaic parameters obtained from reverse and forward *J-V* scans of solar cells shown in **Figure 5.7.a** (↑-forward scan, ↓-reverse scan)

Configuration	Scan	V_{OC} (V)	FF	J_{SC} (mA/cm^2)	PCE(%)
$CsPbBr_{1.5}I_{1.5}/C_{60}$	↑	1.00	0.56	8.0	4.4
	↓	0.70	0.39	7.0	1.9
$MA_{1-x}Cs_xPbI_{1.5}Br_{1.5}/C_{60}$	↑	1.06	0.74	10.7	8.4
	↓	1.14	0.56	10.7	6.9
$CsPbBr_{1.5}I_{1.5}/PCBM/C_{60}$	↑	1.05	0.61	9.6	6.2
	↓	1.00	0.38	9.5	3.6
$MA_{1-x}Cs_xPbI_{1.5}Br_{1.5}/PCBM/C_{60}$	↑	**1.14**	**0.74**	**10.4**	**8.8**
	↓	**1.23**	**0.72**	**10.4**	**9.2**
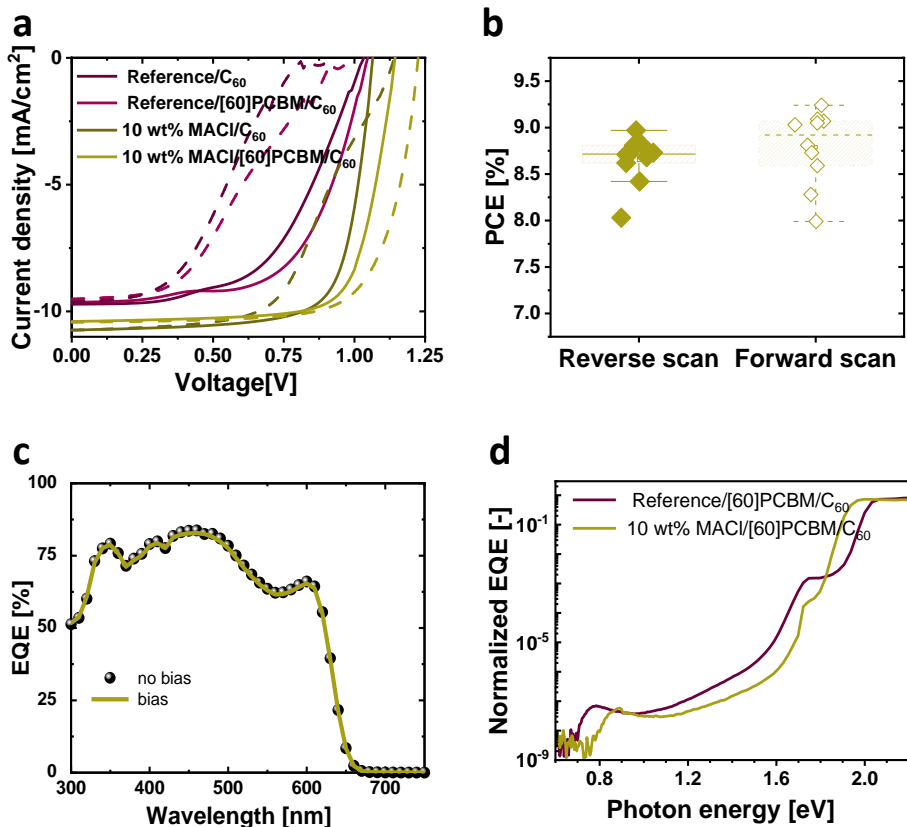
Figure 5.7. Device characterization. a) *J-V* characteristics for $CsPbBr_{1.5}I_{1.5}$ and $MA_{1-x}Cs_xPbI_{1.5}Br_{1.5}$ cells with a glass/ITO/2PACz/perovskite/ETL/BCP/Al configuration, where the ETL consists of C_{60} (40 nm) or a bilayer of PCBM (20 nm) and C_{60} (20 nm). Solid lines represent reverse scans, dashed lines forward scans. **b)** PCE statistics for glass/ITO/2PACz/$MA_{1-x}Cs_xPbI_{1.5}Br_{1.5}$/PCBM/$C_{60}$/BCP/Al devices. Average PCEs are 8.7% (reverse) and 8.8% (forward). **c)** External quantum efficiency (EQE) spectrum of the best $MA_{1-x}Cs_xPbI_{1.5}Br_{1.5}$ solar cell. **d)** Sub-bandgap EQE spectra of $CsPbBr_{1.5}I_{1.5}$ and $MA_{1-x}Cs_xPbI_{1.5}Br_{1.5}$ solar cells using PCBM/C_{60} as ETL. The $CsPbBr_{1.5}I_{1.5}$ cell shows an Urbach energy E_U = 20.8 meV, which decreases to E_U = 17.0 meV for the $MA_{1-x}Cs_xPbI_{1.5}Br_{1.5}$ cell, implying lower energetic disorder near the band edge.

5.2.5. Intrinsic and operational stability

One crucial issue for mixed-halide perovskites is light-induced halide segregation. The segregation of mixed-halide perovskites into iodide-rich and bromide-rich domains under continuous illumination was first observed in methylammonium lead iodide-bromide $MAPb(I_{1-x}Br_x)_3$ perovskites as a characteristic red shift of the PL spectrum[58]. The phenomenon is driven by the

lower bandgap energy of the iodide-rich domains where charge carriers localize during illumination and where bromide-iodide exchange in the lattice can further reduce the free energy. Illumination of mixed-halide lead-based perovskites results in segregation into bromide-rich and iodide-rich regions, when the bromide concentration exceeds about 20%[11]. The process is reversible in the dark. Driven by entropy, halide ions remix in the dark and the PL spectrum blue shifts. Apart from a shift in the PL spectrum, light-induced halide segregation can lead to near complete loss of photovoltaic performance, especially of the J_{SC}. PL spectroscopy represents the most extensively adopted method to characterize light-induced processes in perovskites.

Since the perovskite of interest has a Br content of 50%, halide segregation can be expected under continuous illumination. To test the stability of $CsPbI_{1.5}Br_{1.5}$ and $MA_{1-x}Cs_xPbI_{1.5}Br_{1.5}$ against light-induced changes, films on glass substrates were illuminated with 530 nm light at 3-Sun equivalent intensity, while held in an inert atmosphere. PL spectra were recorded at logarithmically spaced time intervals, by passing the PL light *via* a 545 nm long-pass filter to a fiber-coupled spectrometer. **Figure 5.8.a** shows a 2D plot of the temporal evolution of the PL spectrum of a $CsPbI_{1.5}Br_{1.5}$ film continuously illuminated for 28 h. The initial PL signal is intense and occurs at 1.98 eV (~625 nm in **Figure 5.8.b**), close to the bandgap. In the first 10^2 s the PL intensity drops. Between 10^2 and 10^3 s, the PL spectra start to red shift and regain intensity. With further illumination, the intensity increases significantly and reaches a maximum at ~10^4 s where the PL peak is found at 1.86 eV (660 nm), i.e., about 0.19 eV below the (initial) optical bandgap of 2.05 eV. Subsequently, the PL intensity decays and shows a blue shift. When the illumination is stopped, a weak blue shifted emission appears. **Figure 5.8.d** shows schematically the rearrangement of halide ions in the dark and under illumination. **Figure 5.8.c** shows a 2D plot of the temporal evolution of the PL spectrum of a $MA_{1-x}Cs_xPbI_{1.5}Br_{1.5}$ film illuminated for 28 h with 3-Sun equivalent light intensity at 530 nm. Surprisingly, the films show no measurable PL signal at the start but develop an intense PL peak at an energy close to 1.81 eV (685 nm) after a few hours. This shows that some halide migration occurs during prolonged illumination. The emission at 1.81 eV is about 0.17 eV below the bandgap (1.98 eV) of the as-prepared $MA_{1-x}Cs_xPbI_{1.5}Br_{1.5}$ perovskite film, similar to what was found for $CsPbI_{1.5}Br_{1.5}$. When the illumination is stopped the PL blue shifts to 1.91 eV (650 nm).
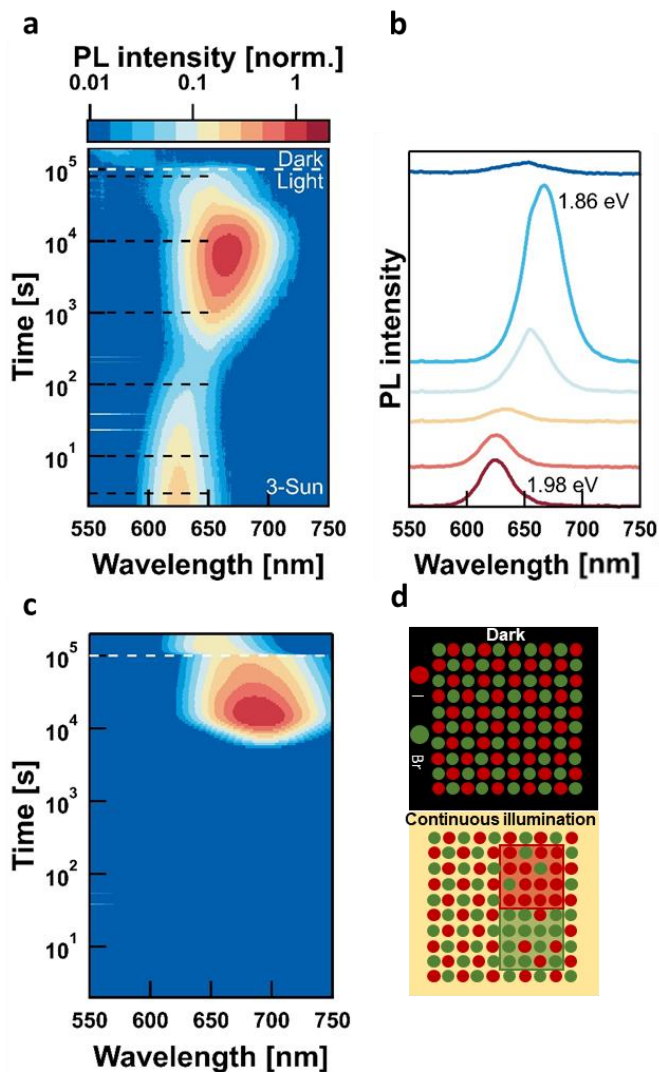
Figure 5.8. Light-induced halide segregation. a) The 2D plot of the temporal evolution of the PL intensity spectra of $CsPbI_{1.5}Br_{1.5}$ on glass, illuminated for 28 h at 3-Sun equivalent intensity at 530 nm. **b)** PL spectra at selected times are indicated by the horizontal dashed lines in panel (a). The red shift of the PL spectra, caused by the continuous visible light illumination, is due halide segregation. **c)** The 2D plot of the temporal evolution of the PL intensity of PL spectra of $MA_{1-x}Cs_xPbI_{1.5}Br_{1.5}$ on glass illuminated for 28 h at 3-Sun equivalent intensity at 530 nm. Surprisingly, the films show no measurable PL signal at the start but develop an intense PL peak at an energy close to the optical bandgap of the as-prepared $MA_{1-x}Cs_xPbI_{1.5}Br_{1.5}$ perovskite film. **d)** Schematic representation of light-induced halide segregation in iodide-bromide perovskites. Under illumination halides reversibly segregate into wide-bandgap Br-rich and narrow-bandgap I-rich domains. Bromide ions are presented as green and Iodide as red dots.
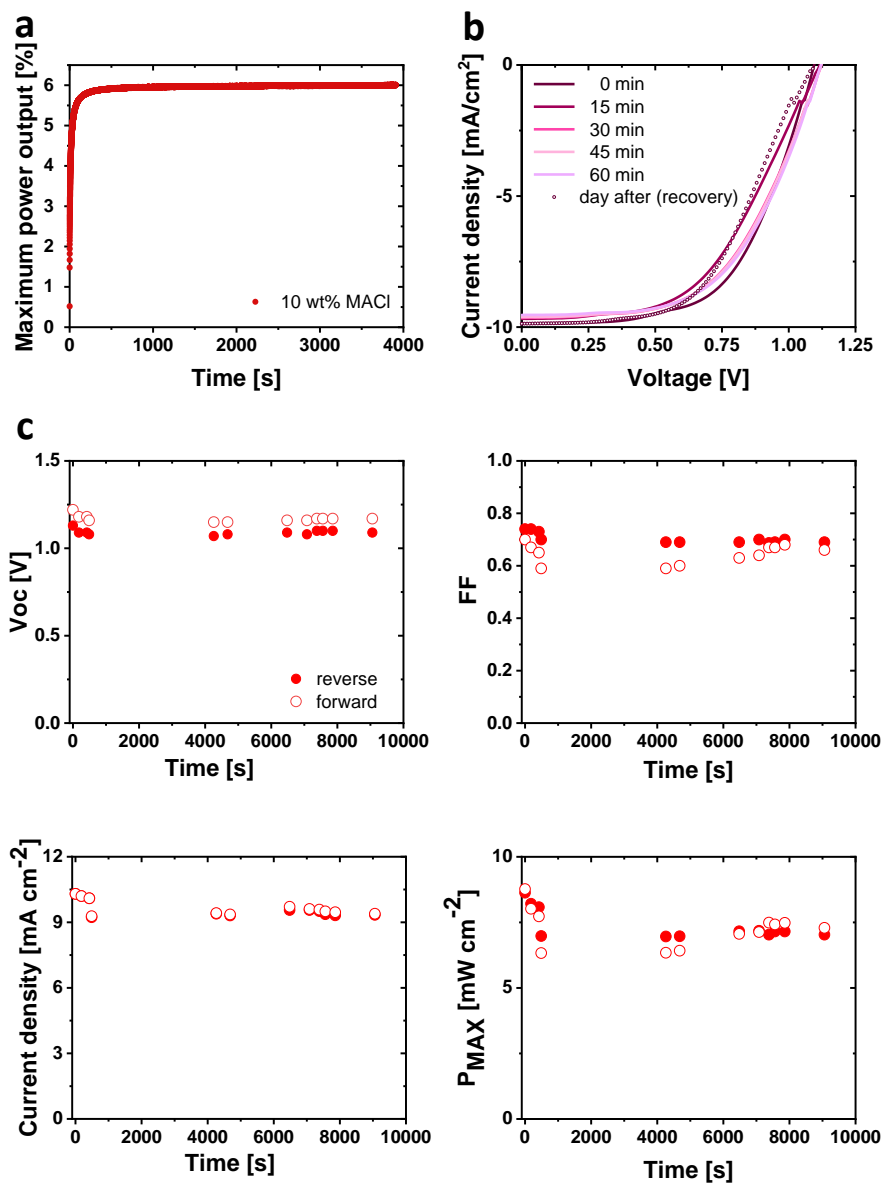
Figure 5.9. Operational stability for MA$_{1-x}$Cs$_x$PbI$_{1.5}$Br$_{1.5}$ solar cells. a) Maximum power point tracking for more than 1 h of MA$_{1-x}$Cs$_x$PbI$_{1.5}$Br$_{1.5}$ solar cells processed during continuous illumination at 1-Sun intensity. The performance of the solar is stable under for more than 1 h. **b)** *J−V* characteristics measured at different time intervals (every 15 minutes) of MA$_{1-x}$Cs$_x$PbI$_{1.5}$Br$_{1.5}$ solar cells during continuous illumination at 1-Sun intensity. Minimal changes are observed in the *J−V* characteristics. **c)** Evolution of PV parameters (*V*$_{OC}$, FF, *J*$_{SC}$, and MPP) during continuous illumination at 1-Sun intensity. The PV parameters are fairly constant during this period.

112

The evolution of the PL spectra shines a light on the dominant emission in different phases of the halide segregation, confirming the existence of halide segregation. While these results show that the $CsPbBr_{1.5}I_{1.5}$ and $MA_{1-x}Cs_xPbI_{1.5}Br_{1.5}$ perovskites are not entirely stable, they are much more stable than similar perovskites with only organic cations instead of Cs^+, where light-induced halide segregation already sets under ambient daylight in less than a minute[58].

To further evaluate the stability of $MA_{1-x}Cs_xPbI_{1.5}Br_{1.5}$ under operational conditions, we studied device performance by measuring the photocurrent at the maximum power point voltage (V_{MPP}) over time under continuous illumination. **Figure 5.9.a** shows that the performance of the $MA_{1-x}Cs_xPbI_{1.5}Br_{1.5}$ solar cell is stable under continuous illumination for more than one hour. $J−V$ characteristics recorded every 15 min, during the continuous illumination at 1-Sun intensity (**Figure 5.9.b**), indicate minimal changes in the $J−V$ characteristics measured at different time intervals during this illumination. Further evidence of the good stability comes from an experiment on a glass/ITO/2PACz/$MA_{1-x}Cs_xPbI_{1.5}Br_{1.5}$/PCBM/$C_{60}$/BCP/Al solar cell that was studied for ~10,000 s during continuous illumination. The PV parameters (V_{OC}, FF, J_{SC}, and the maximum power (P_{max})) are fairly constant during this period. After an initial drop that occurs in the first 1000 s, all parameters are stable for more than 2 h (**Figure 5.9.c**). With the $MA_{1-x}Cs_xPbI_{1.5}Br_{1.5}$ perovskite composition we have achieved much improved device stability, solving one of the major drawbacks of mixed-halide perovskites.

5.3. Conclusion

A $p–i–n$ single junction mixed-halide wide-bandgap perovskite was developed. Wide-bandgap semiconductors are much needed for future use in triple-junction, where a $p–i–n$ configuration seems the most promising configuration. Perovskite solar cells based on a wide bandgap (E_g = 2.05 eV) $CsPbI_{1.5}Br_{1.5}$ were found to give poor performance with low FF, low V_{OC}, and large hysteresis between forward and reverse $J-V$ scans. QFLS experiments indicated that the major contributors to the V_{OC} loss are non-radiative recombination in the bulk of perovskite layer and at the interface between the perovskite and the C_{60} ETL. In both cases it is thought that defects create traps states that enhance non-radiative recombination.

To improve the perovskite film morphology, different concentrations of MACl were introduced as an additive to the perovskite precursor solution to slow down the crystallization rate. The best surface morphology and grain sizes were obtained for films in which 10 wt% MACl was added. XRD and NMR confirmed the presence of methylammonium in the crystal lattice, while XPS indicated an undetectable level of Cl^-. Hence the composition of the film is $MA_{1-x}Cs_xPbI_{1.5}Br_{1.5}$.

The inclusion of MA$^+$ caused a narrowing of the bandgap from 2.05 to 1.98 eV. The use of MACl as an additive increased the J_{SC} and FF, reduced hysteresis, and removed the s-shape that was present in the J–V characteristics. While the film quality and device performance reached an optimum at 10 wt% MACl, no major improvement was achieved for the V_{OC}. Still, because the bandgap is reduced and the V_{OC} remained constant, the improved perovskite features less non-radiative recombination, suggested by sub-bandgap EQE measurements.

QFLS analysis demonstrated that the interface between the perovskite and the ETL needs to be carefully engineered. Lower V_{OC} losses were achieved using an ETL consisting of a PCBM/C_{60} bilayer, effectively replacing a C_{60}-only ETL. The PCBM/C_{60} bilayer ETL improves the performance compared to PCBM-only or only C_{60}-only ETLs, especially in terms of the V_{OC}. The performances of devices made in this configuration have good reproducibility. The champion device had an efficiency of 9.9%, with a V_{OC} of 1.23 V, which is one of the highest reported for similar wide-bandgap perovskites in the inverted configuration. PCBM successfully minimized losses caused by defect states. The Urbach energy for devices with a bilayer ETL decreased from 20.8 meV for $CsPbI_{1.5}Br_{1.5}$ to 17.0 meV for $MA_{1-x}Cs_xPbI_{1.5}Br_{1.5}$. This implies a lower energetic disorder at the band edge for devices processed with MACl. As the bandgap narrowed, the defect state in the bandgap became relatively shallower, which possibly lowered non-radiative recombination.

By developing $MA_{1-x}Cs_xPbI_{1.5}Br_{1.5}$ thin film absorbers via additive engineering and using a PCBM/C_{60} bilayer ETL, we have significantly reduced the non-radiative recombination losses that currently limit wide-bandgap mixed-halide perovskite p–i–n configuration solar cells and achieved stable performance under continuous illumination for 2 h. These results contribute to solving the main challenges of the wide-bandgap perovskite, i.e., the high V_{OC} and high stability required to make these materials suitable for triple-junction all-perovskite solar cells.

5.4. Methods

Materials

All materials were used as received unless specified otherwise. Poly[bis(4-phenyl)(2,4,6-trimethylphenyl)amine] (PTAA) was purchased from EM Index Co. (M_w = 14.5 kg/mol) and was stored and weighed in ambient conditions. [6,6]-Phenyl-C_{61}-butyric acid methyl ester (PCBM) (99%) was purchased from Solenne B.V. and stored in ambient conditions. PEDOT:PSS aqueous dispersion (PVP Al 4083) was purchased from Heraeus Clevios and stored in ambient conditions. [2-(9H-carbazol-9-yl)ethyl]phosphonic acid (2PACz) (98%), lead iodide (>99.99%, trace metals basis), and lead bromide (>98%) were purchased from TCI. Cesium iodide (beads, 99.999%) was purchased from Sigma Aldrich.

114

N,N-dimethylformamide (DMF) (99.8%), dimethyl sulfoxide (DMSO) (99.9%) and methyl acetate (MeOAc) (99.5%) were purchased from Sigma Aldrich. Anhydrous ethanol (0.1% H_2O) was purchased from Merck Millipore. Methylammonium iodide and methylammonium bromide were purchased from Greatcell Solar Materials. Methylammonium chloride was purchased from Sigma Aldrich. Deuterated DMSO (for NMR) was purchased from VWR International. C60 (99.95%) was purchased from SES Research and bathocuproine (BCP, 99%) was purchased from Lumtec. If not implied differently, chemicals were stored and used in a nitrogen-filled glove box.

Precursor solution preparation

2PACz was dissolved (0.3 mg/mL) in anhydrous ethanol and sonicated (sealing the vial with parafilm) for 30 min prior to use. The $CsPbI_{1.5}Br_{1.5}$ precursor solution containing CsI (1 M), PbI_2 (0.25 M), and $PbBr_2$ (0.75 M) was dissolved in DMSO:DMF=(1.8):1 and stirred overnight at 60 ºC. When mentioned, different (5, 7, 10, 15, 20) wt% of MAX (X = I, Br, Cl) relative to $CsPbI_{1.5}Br_{1.5}$, were used. When added MAX solutions were stirred overnight at 60 ºC and filtered with a PVDF 0.22 μm filter, before use.

Single-junction solar cell fabrication

Bare glass (for thin films) or patterned ITO coated glass (for solar cells) substrates (Naranjo Substrates, 15-17 Ω/sq.) were cleaned in an ultrasonic bath of acetone, followed by scrubbing with sodium dodecyl sulphate (Acros, 99%) soap solution in deionized water, sonication in the soap solution, rinsing in deionized water, followed by sonication in 2-propanol. They were then exposed to UV-O_3 treatment for 30 min before being transferred to a nitrogen-filled glove box. The hole-transport layer (2PACz) was deposited on the substrates by casting the solution, allowing it to spread for few seconds, and spin coating at 3000 rpm for 30 s. After all the samples were coated, they were annealed at 100 ºC for 10 min. After cooling down, the perovskite layer was deposited by spin coating 100 μL of the precursor solution at 600 rpm for 5s, followed by 4000 rpm for 30 s. At ~10 s before the end of spin coating 200 μL of methyl acetate (antisolvent) was dripped onto the spinning substrate. At the end of the spin coating process, the substrate was immediately annealed at 35 ºC for 5 min, at 120 ºC for 10 min, and at 165 ºC for 5 min. C60 was deposited by thermal evaporation at 0.5 Å/s. BCP (8 nm) was evaporated by thermal evaporation at a rate of 0.5 Å/s. Aluminum (100 nm) was deposited by thermal evaporation at a rate of 2 Å/s.

Thin film characterization

UV-vis-NIR spectra were measured using a PerkinElmer Lambda 1050 spectrometer. Surface morphology was characterized using a scanning electron microscope (Thermo Fischer Scientific, Quanta 3D FEG) using a 10 kV electron beam and a secondary ion beam detector. XRD was conducted in ambient conditions using a Bruker 2D phaser using Cu Kα (λ = 1.5405 Å) X-ray source. Measurements were performed in the range 3-40° with a step size of 0.02° and collection time of 1 s. X-ray photoelectron spectroscopy (XPS) was conducted using a Thermo Scientific KA1066 spectrometer. The excitation source was monochromatic Al Kα (1486.6 eV) X-rays. The measurements were done without any pre-sputtering procedure and the layers were in contact with air briefly before measurement. A gold clamp and an electron flood gun were used to reduce sample charging. The data was analyzed using commercial software Avantage with Shirlyey

background subtraction. To record PL spectra during continuous illumination, a 530 nm (Thorlabs M530L3) LED source driven by a Thorlabs DC4104 driver was used while the film was held an inert atmosphere. The PL, filtered by a 545 nm long pass filter, was focused on an optical fiber, and recorded using a spectrometer (Avantes Avapec-2048x14).^{1}H and ^{13}C NMR spectra were obtained on a 400 MHz Bruker spectrometer. All the measurements were performed at room temperature in deuterated DMSO. Chemical shifts (δ) are reported in part per million (ppm).

Excitation for the absolute PL measurements was realized with a 455 nm LED (Thorlabs, M455F3 - 455 nm Fiber-Coupled LED) through an optical fiber into an integrating sphere (Avantes, AvaSphere-30-REFL). The opening of the integrating sphere for excitation light was equipped with an in-line filter holder with a 550 nm short pass filter (Edmund Optics). A second optical fiber was attached to the output of the integrating sphere and connected to an AvaSpec-HERO spectrometer (Avantes, AVASPEC-HSC1024X58TEC-EVO). To the opening of the spectrometer, a filter holder was directly attached, holding a 550 nm long pass filter (Edmund Optics). In order to allow a prediction of the open-circuit voltage corresponding to AM1.5 illumination conditions, the monochromatic excitation photon flux in the experiment was adjusted to correspond to the number of photons that would be absorbed for broad-band AM1.5 excitation. The intensity of the LED was adjusted to a 1-Sun equivalent intensity by measuring the illumination with a power meter (Ophir Nova) and matching this to the current density (J_{SC}) of the perovskite solar cells.

The system was calibrated by using a calibrated halogen lamp (Avantes) with specified spectral irradiance used to illuminate to integrating sphere. A spectral correction factor was established to match the spectral output of the detector to the calibrated spectral irradiance of the lamp. The spectral photon flux (ϕ_{PL}) was obtained from the corrected spectrometer signal (spectral irradiance) by a Jacobian transformation and division through the photon energy ($\frac{hc}{\lambda}$) using Matlab.

The quasi-Fermi level splitting (QFLS) was obtained by analyzing the spectral photon flux using nonlinear least squares fit of Eqn. 1 by using Matlab:

$$\phi_{PL}(E) = \frac{1}{4\pi^2\hbar^3c^2} \frac{\alpha(E)E^2}{\exp\big((E - \Delta\mu)/k_BT\big) - 1} \tag{1}$$

where $\alpha(E)$ is the absorption coefficient and $\Delta\mu$ is the QFLS. For thin film compounds, the absorption coefficient is very often not exactly known, but for photon energies sufficiently larger than the bandgap it can be approximated to be equal to 1. Reducing the relation used to fit to Eqn. 2:

$$\phi_{PL}(E) = \frac{1}{4\pi^2\hbar^3c^2} \frac{E^2}{\exp\big((E - \Delta\mu)/k_BT\big) - 1} \tag{2}$$

Device characterization

Current density versus voltage (*J-V*) characterization of solar cells was done using a tungsten-halogen illumination source filtered by a UV filter (Schott GG385) and daylight filter (Hoya LB120) with the intensity adjusted to 100 mW/cm^2. A shadow mask with an aperture smaller than the active area (0.0676 or 0.1296 cm^2) was used to define the illumination area of the cell. The solar cells were operated under reverse or forward sweeps (between +1.5 V and –0.5 V) at a rate of 0.25 V/s by a Keithley 2400 source meter.

To measure the external quantum efficiency, the cells were contacted in a nitrogen-filled container. A 50 W tungsten halogen lamp was used as a light source. The light was chopped at 158 Hz before passing into a monochromator (Oriel, Cornerstone 130). A reference silicon detector was used to calibrate the current from the cell which was fed into a current pre-amplifier (Stanford Research, SR 570). The resulting voltage was measured using a lock-in amplifier (Stanford Research, SR 830). A green (Thorlabs, M530L3) LED was used as a light bias to generate approximately 1-Sun equivalent illumination intensity. Integration of the EQE with the AM1.5G spectrum afforded values of the J_{SC}. To measure EQE in the sub-bandgap region *via* sensitive photocurrent spectroscopy., an Oriel 3502 light chopper, Cornerstone 260 monochromator (CS260-USB-3-MC-A), a Stanford Research SR 570 low-noise current preamplifier, a Stanford Research SR830 lock-in amplifier, and a 250 W tungsten-halogen lamp were used. The light was chopped at a frequency of 330 Hz. A series of long pass filters (OD ≥ 5) with increasing cut-on wavelengths was placed between the lamp and monochromator to remove stray light and higher order component during the measurement. The monochromatic light is then passed through a concave cylindrical lens, to focus the light and increase the intensity on the active area of the solar cell. The solar cell was kept in an electrically insulated nitrogen-filled container. The cell is contacted using spring-loaded gold contacts and the container is contacted with a LEMO connector. The current generated by the solar cell is fed into the to the preamplifier *via* a triaxial cable which is kept on a distance from other cabling to minimize the spurious signals due to induction. Above the bandgap, a sensitivity of 200 µA/V was used for the preamplifier, and this was increased to 200 nA/V to measure signals below the bandgap. The lock-in amplifier was set in float mode to reduce background noise and a time constant of 1 s and a settling time of 15 s were used. Calibrated Si and InGaAs photodiodes were used to determine incident light intensity.

5.5. References

1. Min, H. *et al.* Perovskite solar cells with atomically coherent interlayers on SnO_2 electrodes. *Nature* **598**, 444–450 (2021).

2. Shockley, W. & Queisser, H. J. Detailed Balance Limit of Efficiency of p-n Junction Solar Cells. *J. Appl. Phys.* **32**, 510–519 (1961).

3. Dai, C. *et al.* Mathematical Decomposition for Influence Factors of Unit GDP Energy Consumption and Demonstration in China. in *Adv. Mater. Res.* **601**, 437–448 (2012).

4. Hörantner, M. T. *et al.* The Potential of Multijunction Perovskite Solar Cells. *ACS Energy Lett.* **2**, 2506–2513 (2017).

5. Unger, E. L. *et al.* Roadmap and roadblocks for the band gap tunability of metal halide perovskites. *J. Mater. Chem. A* **5**, 11401–11409 (2017).

6. Caputo, M. *et al.* Electronic structure of $MAPbI_3$ and $MAPbCl_3$: importance of band alignment. *Sci. Rep.* **9**, 15159 (2019).

7. Xiao, K. *et al.* Solution-processed monolithic all-perovskite triple-junction solar cells with efficiency exceeding 20%. *ACS Energy Lett.* **5**, 2819–2826 (2020).

8. Li, H. & Zhang, W. Perovskite Tandem Solar Cells: From Fundamentals to Commercial Deployment. *Chem. Rev.* **120**, 9835–9950 (2020).

9. Eperon, G. E., Hörantner, M. T. & Snaith, H. J. Metal halide perovskite tandem and multiple-junction photovoltaics. *Nat. Rev. Chem.* **1**, 0095 (2017).

10. Lin, R. *et al.* All-perovskite tandem solar cells with improved grain surface passivation. *Nature* **603**, 73–78 (2022).

11. Mahesh, S. *et al.* Revealing the origin of voltage loss in mixed-halide perovskite solar cells. *Energy Environ. Sci.* **13**, 258–267 (2020).

12. Niu, G., Li, W., Li, J., Liang, X. & Wang, L. Enhancement of thermal stability for perovskite solar cells through cesium doping. *RSC Adv.* **7**, 17473–17479 (2017).

13. Ahmad, W., Khan, J., Niu, G. & Tang, J. Inorganic $CsPbI_3$ Perovskite-Based Solar Cells: A Choice for a Tandem Device. *Sol. RRL* **1**, 1700048 (2017).

14. Sutton, R. J. *et al.* Bandgap-Tunable Cesium Lead Halide Perovskites with High Thermal Stability for Efficient Solar Cells. *Adv. Energy Mater.* **6**, 1502458 (2016).

15. Fu, S. *et al.* Effective Surface Treatment for High-Performance Inverted $CsPbI_2Br$ Perovskite Solar Cells with Efficiency of 15.92%. *Nano-Micro Lett.* **12**, 1–13 (2020).

16. Guo, Z. *et al.* Dopant-Free Polymer HTM-Based $CsPbI_2Br$ Solar Cells with Efficiency Over 17% in Sunlight and 34% in Indoor Light. *Adv. Funct. Mater.* **31**, 2103614 (2021).

17. Lu, J., Chen, S. C. & Zheng, Q. Defect Passivation of $CsPbIBr_2$ Perovskites for High-Performance Solar Cells with Large Open-Circuit Voltage of 1.28 v. *ACS Appl. Energy Mater.* **1**, 5872–5878 (2018).

18. Yang, S. *et al.* Excellent Moisture Stability and Efficiency of Inverted All-Inorganic $CsPbIBr_2$ Perovskite Solar Cells through Molecule Interface Engineering. *ACS Appl. Mater. Interfaces* **12**, 13931–13940 (2020).

19. Grischek, M. *et al.* Efficiency Potential and Voltage Loss of Inorganic $CsPbI_2Br$ Perovskite Solar Cells. *Sol. RRL* **6**, 2200690 (2022).

20. Rühle, S. Tabulated values of the Shockley-Queisser limit for single junction solar cells. *Sol. Energy* **130**, 139–147 (2016).

21. Mailoa, J. P. *et al.* A 2-terminal perovskite/silicon multijunction solar cell enabled by a silicon tunnel junction. *Appl. Phys. Lett.* **106**, 121105 (2015).

22. Albrecht, S. *et al.* Monolithic perovskite/silicon-heterojunction tandem solar cells processed at low temperature. *Energy Environ. Sci.* **9**, 81–88 (2016).

23. Jiang, F. *et al.* A two-terminal perovskite/perovskite tandem solar cell. *J. Mater. Chem. A* **4**, 1208–1213 (2016).

24. Eperon, G. E. *et al.* Perovskite-perovskite tandem photovoltaics with optimized band gaps. *Science.* **354**, 861–865 (2016).

25. Bush, K. A. *et al.* 23.6%-Efficient Monolithic Perovskite/Silicon Tandem Solar Cells

With Improved Stability. *Nat. Energy* **2**, 17009 (2017).

26. Wang, J. *et al.* 16.8% Monolithic all-perovskite triple-junction solar cells via a universal two-step solution process. *Nat. Commun.* **11**, 5254 (2020).

27. Zai, H. *et al.* Low-temperature-processed inorganic perovskite solar cells via solvent engineering with enhanced mass transport. *J. Mater. Chem. A* **6**, 23602–23609 (2018).

28. Eze, M. C. *et al.* Improving the efficiency and stability of in-air fabricated perovskite solar cells using the mixed antisolvent of methyl acetate and chloroform. *Org. Electron.* **107**, 106552 (2022).

29. Lei, J. *et al.* Efficient planar $CsPbBr_3$ perovskite solar cells by dual-source vacuum evaporation. *Sol. Energy Mater. Sol. Cells* **187**, 1–8 (2018).

30. Xi, J., Yuan, J., Yan, X., Binks, D. & Tian, J. Gradient Annealing of Halide Perovskite Films for Improved Performance of Solar Cells. *ACS Appl. Energy Mater.* **3**, 8130–8134 (2020).

31. Paniagua, S. A. *et al.* Phosphonic acid modification of indium-tin oxide electrodes: Combined XPS/UPS/ contact angle studies. *J. Phys. Chem. C* **112**, 7809–7817 (2008).

32. Phung, N. *et al.* Enhanced Self-Assembled Monolayer Surface Coverage by ALD NiO in p-i-n Perovskite Solar Cells. *ACS Appl. Mater. Interfaces* **14**, 2166–2176 (2022).

33. Liu, C. *et al.* All-Inorganic $CsPbI_2Br$ Perovskite Solar Cells with High Efficiency Exceeding 13%. *J. Am. Chem. Soc.* **140**, 3825–3828 (2018).

34. Wojciechowski, K. *et al.* C_{60} as an efficient n-type compact layer in perovskite solar cells. *J. Phys. Chem. Lett.* **6**, 2399–2405 (2015).

35. Jeng, J. Y. *et al.* $CH_3NH_3PbI_3$ perovskite/fullerene planar-heterojunction hybrid solar cells. *Adv. Mater.* **25**, 3727–3732 (2013).

36. Fernandez-Delgado, O. *et al.* The role of fullerene derivatives in perovskite solar cells: Electron transporting or electron extraction layers? *J. Mater. Chem. C* **9**, 10759–10767 (2021).

37. Xu, F. *et al.* Solar Energy Materials & Solar Cells Elucidating the evolution of the current-voltage characteristics of planar organometal halide perovskite solar cells to an S-shape at low temperature. *Sol. Energy Mater. Sol. Cells* **157**, 981–988 (2016).

38. Ahmed, Y. *et al.* Organic additives in all-inorganic perovskite solar cells and modules: from moisture endurance to enhanced efficiency and operational stability. *J. Energy Chem.* **67**, 361–390 (2022).

39. Dong, C. *et al.* A Green Anti-Solvent Process for High Performance Carbon-Based $CsPbI_2Br$ All-Inorganic Perovskite Solar Cell. *Sol. RRL* **2**, 1800139 (2018).

40. Wang, Y. *et al.* Stitching triple cation perovskite by a mixed anti-solvent process for high performance perovskite solar cells. *Nano Energy* **39**, 616–625 (2017).

41.   Guo, Y. *et al.* Inorganic CsPbIBr$_2$-Based Perovskite Solar Cells: Fabrication Technique Modification and Efficiency Improvement. *Sol. RRL* **3**, 1900135 (2019).

42.   Zhang, F. *et al.* Ultra-smooth CsPbI$_2$Br film via programmable crystallization process for high-efficiency inorganic perovskite solar cells. *J. Mater. Sci. Technol.* **66**, 150–156 (2021).

43.   Hu, M., Bi, C., Yuan, Y., Bai, Y. & Huang, J. Stabilized wide bandgap MAPbBr$_x$I$_{3-x}$ perovskite by enhanced grain size and improved crystallinity. *Adv. Sci.* **3**, 6–11 (2015).

44.   Guerra, J. A. *et al.* Determination of the complex refractive index and optical bandgap of CH$_3$NH$_3$PbI$_3$ thin films. *J. Appl. Phys.* **121**, 173104 (2017).

45.   Chen, L. *et al.* Inverted All-Inorganic CsPbI$_2$Br Perovskite Solar Cells with Promoted Efficiency and Stability by Nickel Incorporation. *Chem. Mater.* **31**, 9032–9039 (2019)

46.   Khan, A. A., Yu, Z., Khan, U., Li, Y. & Eric, D. Solution-processed photodetector based on Br incorporated perovskite materials. in *AOPC 2019: Nanophotonics* (eds. Dai, D., Zhou, Z. & Yuan, X.-C.) 21 (SPIE, 2019).

47.   Jin, S. Can We Find the Perfect A-Cations for Halide Perovskites? *ACS Energy Lett.* **6**, 3386–3389 (2021).

48.   Beimborn, J. C., Hall, L. M. G., Tongying, P., Dukovic, G. & Weber, J. M. Pressure Response of Photoluminescence in Cesium Lead Iodide Perovskite Nanocrystals. *J. Phys. Chem. C* **122**, 11024–11030 (2018).

49.   Cao, Y. *et al.* Pressure-Tailored Band Gap Engineering and Structure Evolution of Cubic Cesium Lead Iodide Perovskite Nanocrystals. *J. Phys. Chem. C* **122**, 9332–9338 (2018).

50.   Yuan, G., Qin, S., Wu, X., Ding, H. & Lu, A. Pressure-induced phase transformation of CsPbI$_3$ by X-ray diffraction and Raman spectroscopy. *Phase Transitions* **91**, 38–47 (2018).

51.   Wang, Q. *et al.* Large fill-factor bilayer iodine perovskite solar cells fabricated by a low-temperature solution-process. *Energy Environ. Sci.* **7**, 2359–2365 (2014).

52.   Namkoong, G., Mamun, A. A. & Ava, T. T. Impact of PCBM/C$_{60}$ electron transfer layer on charge transports on ordered and disordered perovskite phases and hysteresis-free perovskite solar cells. *Org. Electron.* **56**, 163–169 (2018).

53.   van Gorkom, B. T., van der Pol, T. P. A., Datta, K., Wienk, M. M. & Janssen, R. A. J. Revealing defective interfaces in perovskite solar cells from highly sensitive sub-bandgap photocurrent spectroscopy using optical cavities. *Nat. Commun.* **13**, 349 (2022).

54.   De Wolf, S. *et al.* Organometallic halide perovskites: Sharp optical absorption edge and its relation to photovoltaic performance. *J. Phys. Chem. Lett.* **5**, 1035–1039 (2014).

55.   Sadhanala, A. *et al.* Preparation of Single-Phase Films of CH$_3$NH$_3$Pb(I$_{1-x}$Br$_x$)$_3$ with Sharp Optical Band Edges. *J. Phys. Chem. Lett.* **5**, 2501–2505 (2014).

56.   De Wolf, S. *et al.* Organometallic Halide Perovskites: Sharp Optical Absorption Edge and Its Relation to Photovoltaic Performance. *J. Phys. Chem. Lett.* **5**, 1035–1039 (2014).

57.   Krückemeier, L., Rau, U., Stolterfoht, M. & Kirchartz, T. How to Report Record Open-Circuit Voltages in Lead-Halide Perovskite Solar Cells. *Adv. Energy Mater.* **10**, 1902573 (2020).

58.   Hoke, E. T. *et al.* Reversible photo-induced trap formation in mixed-halide hybrid perovskites for photovoltaics. *Chem. Sci.* **6**, 613–617 (2015).

6

Polymer honeycomb structures

Abstract

Porous surfaces possess a high specific surface area and are attractive for a variety of applications such as in membranes, catalysis, sensors, and optoelectronic devices. For solar cells, textured substrates have been introduced to enhance the photon absorption within the active layer. Porous structures can be made using different templating methods. Here, the breath figure method and polydimethylsiloxane (PDMS) stamps are used to form polystyrene-*block*-polybutadiene-*block*-polystyrene (SBS) films with a porous honeycomb structure. The key characteristics of SBS honeycomb porous films were investigated. To gain stability against elevated temperatures and non-polar organic solvents, SBS honeycombs were cross-linked *via* the pendant vinyl groups of the polybutadiene block, using 2,2′-azobis(2-methylpropionitrile) (AIBN) as thermal initiator. Improved hexagonal ordering of the honeycombs was obtained by employing 7:3 (w/w) blends of SBS and polystyrene (PS), but these could not be cross-linked because of the reduced number of vinyl bonds in the blends. With unconventional methods such as spin coating and using a PDMS stamp, patterned against polystyrene honeycomb, it was possible to form thin monolayer honeycomb structures with very low thickness (200 nm) and high resistance against elevated temperatures and solvents with different polarity.

6.1. Introduction

An important factor to the efficiency of perovskite solar cells is absorption of light by the photoactive layer. In planar cells, a thin (400 to 1000 nm) perovskite layer is sandwiched between hole-selective and electron-selective charge transport layers. In the commonly used device configuration, incident light is passing through a substrate, a transparent conducting oxide (TCO) electrode, and one charge transport layer. Each of these layers causes parasitic absorption and reflection of light at their interfaces. Absorption of light by the TCO reduces the transmission of near infrared (NIR) light. To prevent transmission losses and reduce reflection, it is possible to use back-contact solar cells. Several strategies have been developed for back-contact perovskite solar cells[1]. In a back-contact perovskite solar cell design, the electron and hole selective contact layers and the two electrodes are deposited in patterned version on the substrate, before applying the perovskite layer. In a series of papers, Bach et al. advanced the use of back contacts that consists of a top electrode with a honeycomb-like grid geometry that is separated from the underlying planar bottom electrode by a similarly shaped insulating layer[2,3,4]. In their examples, the honeycomb structures were made using photolithography or microsphere lithography.

Another approach to enhance the photon absorption by the active layer of a solar cell is by using a textured substrate. By texturing, the incident light is scattered and the optical path length is elongated[5,6,7]. Also for texturing, the use of honeycomb structures has been explored, both for crystalline silicon[8,9,10] and perovskite solar cells[11,12].

Honeycomb surfaces can possess a high specific surface area which makes them suitable for a variety of chemical, electronic, and photonic applications, such as membranes, catalysts, and sensors. Important characteristics are the pore size and its distribution. Honeycomb structures can be made using photolithography and templating methods. In many cases, however, preparation of templates is not simple, and they need to be removed once the porous film is prepared. An alternative and simpler approach is the use of breath figures. In this technique, the template is an ordered array of water droplets and removal of the template is simply water evaporation.

The breath figure method is based on the spontaneous condensation of water droplets on cold surfaces that are subjected to a humid environment of at least 50% relative humidity (RH)[13]. The idea of breath figures comes from Lord Rayleigh (1911), who noticed organized arrays of lens-shaped water droplets, on a clean surface, created when condensed water droplets collapsed[14]. Owing to the hexagonal pattern of droplets that can form, highly ordered porous polymer films are also called honeycomb structured porous films, or simply honeycombs. The first study published on honeycombs made *via* the breath figure method from a polymer solution was by Francois et al.[15], who used polystyrene (PS) and

poly(*para*-phenylene)-*b*-PS block copolymers. Initially, it was thought that only star polymers were capable of sustaining the formation of regular hexagonal arrays, but later on, ordered porous films from linear (polyimides, light-emitting, semi-conducting, and biocompatible), graft, hyperbranched polymers, and coil–coil or rod–coil di-block copolymers have also been reported[16].

The breath figure method is a simple technique and the only equipment requirements are a hygrometer and an appropriate capsule with humid airflow (**Figure 6.1.a**). Despite the easiness of the setup and procedure, the mechanism behind honeycomb formation is complex. In general, the formation of the ordered hexagonal structure, starting from polymer solution involves several steps[13]:

- A polymer solution in a volatile solvent is drop casted on a cold substrate under a RH of at least 50%.
- Water droplets condensate on the solution surface, triggered by the endothermic evaporation of the solvent. Small liquid drops are thermodynamically stable and do not evaporate.
- Condensed water droplets move and organize into islands arranged in a hexagonal pattern.
- Water droplets are stabilized due to the polymer that assembles around the drop and prevents their coalescence.
- Water droplets grow due to the vapor from the atmosphere. Evaporation time should be long enough to provide complete coverage of the surface.
- Water droplets sink into the solution making an indentation.
- Total evaporation of the casting solvent and finally thorough evaporation of water reveals a porous structure.

The process is illustrated in **Figure 6.1.c** (reproduced with permission from reference[17]). The final film is porous and usually white, contrary to the transparent films, made in dry conditions. Several variations to the basic technique have been reported, such as the airflow technique, the cold-stage casting technique, the casting on water technique, the emulsion technique, and combinations with spin coating and dip-coating[18].

The honeycomb structure and corresponding scanning electron microscope figure (SEM) are presented in **Figure 6.1.b**. The key characteristics of honeycomb porous films are pore size and pore arrangement. Pore size depends on parameters such as relative humidity, temperature, airflow, substrate, solvent volatility and polarity, together with the nature and concentration of the used polymer. Control of the pore size can be mostly achieved by regulating the humidity during casting. The observed trend indicates that the size of the pores in the films increases almost linear with the RH. Higher RH also slows solvent evaporation, which leads to the growth of water droplets and the formation of larger pores. On the other hand, vast condensation at high humidity may result in the coalescence of water droplets, leading to a wide pore

size distribution[13]. Contrary to the level of humidity, an increase in the flow rate usually decreases the pores size[19].
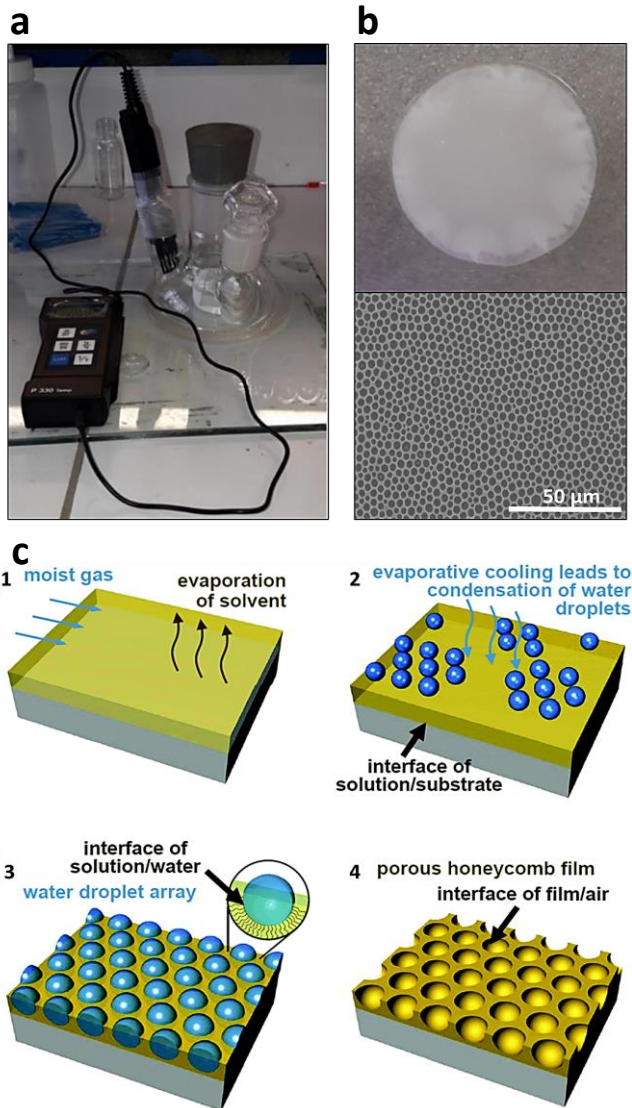
Figure 6.1. Breath figure formation. a) Humid enclosure used for making honeycomb structures with breath figure method. **b)** Polystyrenes honeycombs. Real look (up) and under optical microscope (down). **c)** Model for the formation of honeycomb films by the breath figure method and the multiple interfaces involved. Used with permission of Royal Society of Chemistry, from Ref.[17]; permission conveyed through Copyright Clearance Center, Inc.

126

Depending on the type of polymer, the pore size is more or less dependent on the concentration of the polymer solution. Generally, the pore size is inversely proportional to the concentration of the polymer in the solution, summarized in the relation $PS = k/C$, where PS is pore size in the film, k a constant dependent on the polymer, and C the concentration of the polymer in the solution[13]. The concentration affects film quality and impacts monolayer or multilayer formation[20].

Besides the influence of these experimental parameters, one of the critical steps in the formation of a honeycomb structure is the polymer precipitation at the solution/water interface[16]. The most preferable solvents for the breath figure technique are nonpolar and volatile because the evaporation rate of the solvent influences the casting process and the condensation of water. The most commonly used solvents are benzene, toluene, chloroform, freon, carbon disulfide, and dichloromethane. Highly volatile solvents produce smaller pores. Billon et al. found that a slow evaporation solvent allows the sinking of the first condensed layer of droplets, leaving space for the creation of a second layer on top of the solution. Mixtures of these solvents are also a common approach[16].

The formation of honeycombs *via* breath figures has mainly been reported for polymers based on PS. Other polymers can be introduced in the formulation to improve desired properties, for example by introducing an additional functional group. Block copolymers present a group of outstanding materials as they can combine the properties of several different polymers in one. They found applications in industry, biotechnology, and nanoelectronics. Polystyrene-*block*-polybutadiene-*block*-polystyrene or in short SBS, is a type of block copolymer with a chain made of three segments. The first and last are chains of PS and in the middle is a chain of polybutadiene (PB) (**Figure 6.2.**). Since PS is a hard plastic and PB is a rubber, SBS as a block copolymer of these two, belongs to the class of hard rubbers. This means SBS has the ability to retain its shape after being subjected to stretching.
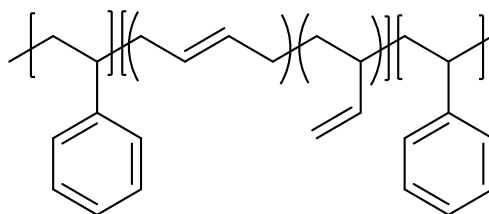
Figure 6.2. Structure of poly(styrene-butadiene-styrene) (SBS) triblock copolymer. The terminal blocks are PS. The middle PB block can have 1,4- and 1,2-polymerized 1,3-butadiene monomers.

To use these honeycombs in devices, they need to fulfill two main requirements. They need to be solvent and temperature resistant and to have a

certain thickness. When exposed to certain solvents and elevated temperatures, honeycombs made of polymers tend to lose their porous structure. The most common approach to prevent a change in morphology is cross-linking. This is the process of linking one polymer chain to another, promoting a change in the physical properties of the polymer.

The focus of this chapter is on the formation, improvement, and cross-linking of the honeycomb structures *via* the breath figure method. Conventional and unconventional methods were explored, in search of a stable and thin monolayer film. Integration of the honeycombs into devices is not a part of the presented work.

6.2. Results

6.2.1. SBS honeycombs formation by breath figure methodology

To successfully make a porous honeycomb structure with a SBS block copolymer, the concentration of the solution and relative humidity are the main factors that need to be established. In general, the formation of the honeycomb pore structure requires a RH of at least 50% and in the case of SBS the threshold is at least 60%. Honeycombs were made by drop casting 100 µL of SBS solution on the testing glass lamella, kept at room temperature.

SBS solutions were made by dissolving different amounts of SBS in chloroform. When SBS was dissolved in chloroform at a concentration of 10 mg/mL and used at 60% RH, the resulting pores were too big and without long-distance hexagonal arrangement. To improve the films, it was needed to increase the concentration and humidity. The concentration was increased gradually from 10 to 40 mg/mL, simultaneously with a rise of the RH from 60% to 73%. The surface topography was studied by optical microscopy and scanning electron microscopy (SEM). **Figure 6.3.a** presents microscopic images of SBS honeycombs, made with different concentrations at RH. The observed trend suggests that with increasing concentration, the pore size and dispersity are decreasing. A SBS concentration of 40 mg/mL in chloroform and a RH of 73% yield the best honeycomb organization and these conditions have been taken as a standard. **Figure 6.3.b** (SEM) shows a standard porous honeycomb polymer film exhibiting a hexagonal array of pores. The size of the pores is not perfectly uniform and deviations from the perfect hexagonal structure (each pore should be symmetrically surrounded by six other pores) can be observed. The pore-to-pore distance is around 10 µm.

To increase the level of hexagonal organization PS, was used together with SBS. Indeed, the first polymer honeycombs were made with PS. Because it is quite straightforward to achieve an almost perfect hexagonally ordered

128

honeycomb structure with PS, mixtures of PS and SBS with different mass ratios were tried. When the PS was predominant in the blend (PS:SBS = 9:1 w/w), cracks formed in the films due to the high glass transition temperature of PS (T_g = 100 °C). On the other hand, including low amounts of PS (PS:SBS = 1:9 or PS:SBS = 2:8 w/w) did not significantly improve microscopic images of the films. However, a blend with mass ratio PS:SBS = 3:7 (w/w) at a concentration of 10 mg/mL and cast under 70% RH showed a highly ordered hexagonal structure. Furthermore, the films had a better hexagonal organization when SBS and PS were mixed in a solid state and left for stirring overnight, compared to the case when films were processed from solutions in which PS and SBS were already dissolved and then mixed. In these samples light scattering was observed, meaning a higher level of organization (**Figure 6.4.a**). The honeycomb structure was imaged by optical microscopy (**Figure 6.4.b**).
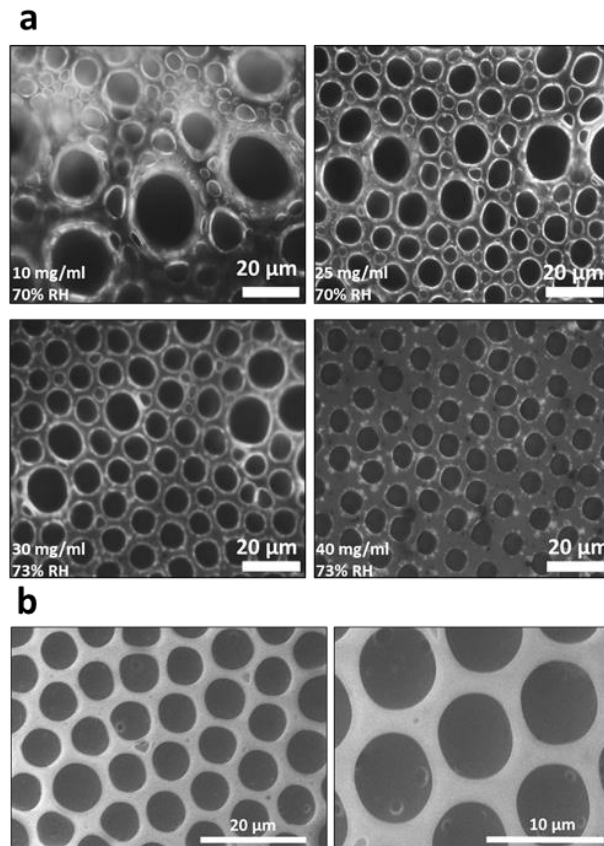
Figure 6.3. Structural properties of honeycombs a) Surface morphology of SBS honeycombs made with different SBS concentration, made by optical microscope. **b)** Surface morphology of SBS honeycomb structure (conditions: 40 mg/mL, 73% RH, room temperature) made by SEM.
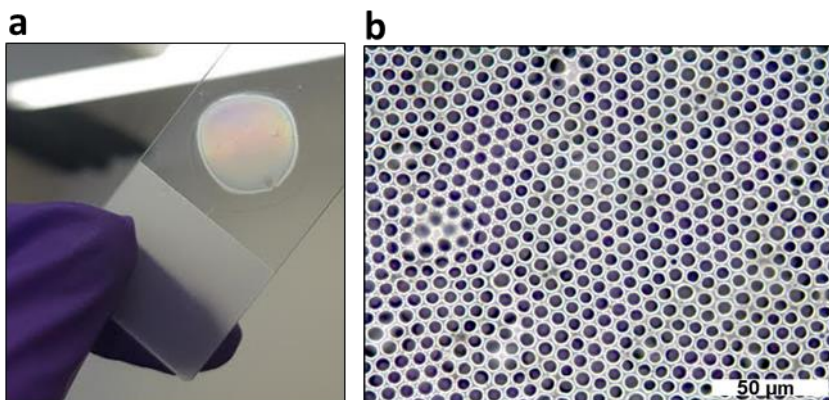
Figure 6.4. Honeycomb made with a blend of 70% SBS and 30% PS. a) Physical coloring against the light is an indicator of the highly organized hexagonal structure. **b)** Confirmation of the hexagonal pore arrangement using an optical microscope image.

## 6.2.2. Cross-linking of the SBS honeycomb films

For some applications, including solar cells, the use of a honeycomb structure requires thermal and solvent stability. When the films are saturated with good solvents for PS or PB (i.e., non-polar solvents), or when they are submitted to temperatures higher than 100 °C (corresponding to the T_g of PS, the T_g of PB is around −50 °C), the SBS porous honeycomb structure is destroyed and the layer becomes a transparent thin polymer film. To prevent this, SBS honeycombs can be cross-linked. The PB block of the SBS triblock copolymer consists of *cis* and *trans* 1,4-polymerized and 1,2-polymerized 1,3-butadiene monomers. The vinyl groups can be crosslinked using radical polymerization. ¹H nuclear magnetic resonance (¹H NMR) of the SBS copolymer (**Figure 6.5.**) can be used to determine the composition. The molar composition of the different segments can be estimated by comparing the integrals (*I*) of the resonances in the aromatic region (δ = 6.25 to 7.25 ppm, labeled a) to c)) to that of the alkenyl protons (δ = 4.75 to 5.75 ppm, labeled d to f). For the latter, one must differentiate between signals of 1,4-polymerized (δ = 5.41, labeled d) and of 1,2-polymerized (δ = 4.95, labeled e and δ = 5.58, labeled f). The molar fraction of PB is given by Eqn. 1

$$PB\% = \frac{(I(d+e) - I(f)/2)/2 + I(f)/2}{I(a+b+c)/5 + (I(d+e) - I(f)/2)/2 + I(f)/2} \times 100\% \qquad (1)$$

Based on the experimental spectrum (**Figure 6.5.**), this results in a PB content of about 80%. The ¹H NMR spectrum also allows the estimation of the fraction of 1,2-polymerized 1,3-butadiene monomers in the PB block. The percentage of vinyl bonds is given by Eqn. 2:

130

$$V\% = \frac{I(f)}{I(d + e) + I(f)/2} \times 100\%$$ (2)

and amounts to 39%
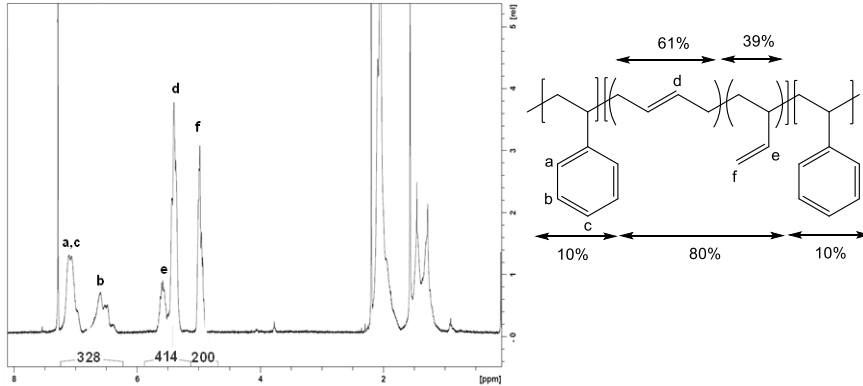
Figure 6.5. Nuclear magnetic resonance of SBS. PB makes up about 80% of the whole SBS, with 39% of it having vinyl bonds that are reactive and able to cross-link.

When the standard SBS honeycomb structure (**Figure 6.6.a**) is treated with toluene, the SBS honeycomb structure flows and becomes a transparent polymer layer (**Figure 6.6.b**). To prevent this, two different strategies were employed to cross-link SBS honeycombs. First, diphenyl(2,4,6-trimethylbenzoyl)phosphine oxide (with different concentrations of 1, 5, and 10 wt%) was used as a photo-initiator for cross-linking initiated by the UV light. Honeycombs made this way were treated with toluene and showed to be only partially resistant to changes (**Figure 6.6.c**), meaning that the structure was only partly cross-linked.

Second, using 2,2′-azobis(2-methylpropionitrile) (AIBN) and initiating cross-linking by elevated temperature, the honeycomb structures could be fully cross-linked. In this case, AIBN (5 wt%, relative to SBS) was dissolved in the SBS-chloroform solution. A honeycomb made from such a mixture was left for 17 h, on a hot plate at a temperature of 80 °C. In contact with toluene, the film structure stayed untouched, indicating successful cross-linking. Additionally, the film was resistant to temperatures exceeding 100 °C (**Figure 6.6.d**).

Unfortunately, honeycombs made from PS:SBS blends, which show improved hexagonal orientation, were more difficult to cross-link, likely due to a lesser amount of pendant vinyl groups. This impacted cross-linking of the whole mixture and even when reducing the PS:SBS ratio to 1:9 w/w instead of 3:7 w/w, cross-linking was just partly successful.
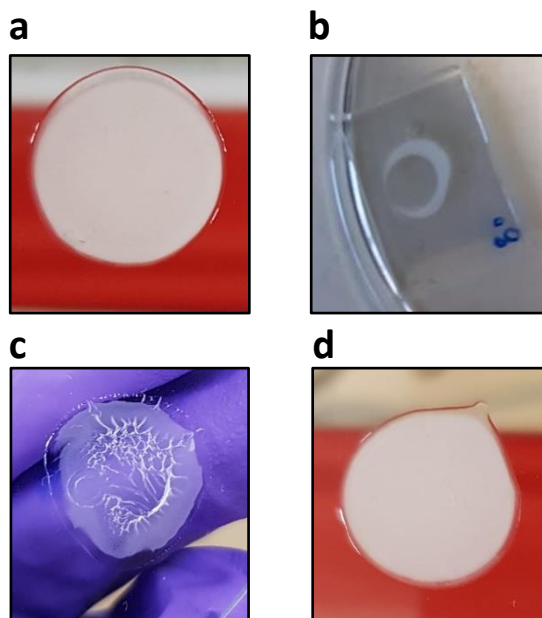
Figure 6.6. SBS honeycombs cross-linking. a) Standard non-cross-linked SBS film. **b)** Standard non-cross-linked SBS film with a toluene drop on it. The SBS honeycomb flows and becomes a transparent polymer layer. **c)** Partly cross-linked film obtained using a photo-initiator and UV light, followed by dropping toluene. **d)** Fully cross-linked film with AIBN at 80 °C. Film was resistant to temperatures exciding 100 °C.

6.2.3. Nonconventional ways for honeycomb formation on thin films

A limitation of the breath figure method is that thick films, more than 1 µm, are obtained. To produce thinner films, nonconventional ways of forming honeycomb structure were explored. For this goal SBS was dissolved in toluene instead of chloroform and the solution was spin coated on a glass lamella (instead of drop-casting). This way, thin layers are formed, several orders of magnitude lower than with conventional method of drop casting. The thickness changes from several micrometers to several nanometers. The spin coating method allows the preparation of films with uniform thickness. Glass lamellas were loaded in a humid environment and the SBS solution was spin coated in a static mode. This procedure was performed with several concentrations (10, 20, 50, and 100 mg/mL) and several spin coating speeds (500, 1000, 1500, and 2000 rpm). For lower spin speeds, the rate of solvent evaporation, which scales with the square root of the rotational velocity, is lower. This induces a higher degree of droplet coalescence, leaving behind larger pores. With increasing spin speed the pore size decreases, due to the faster evaporation[21].

SEM figures (**Figure 6.7.a**) show a porous structure with less ordered patterns in comparison to conventional drop-casting. Pores are more elongated than spherical shapes. Even though atomic force microscopy (AFM), as a non-destructive and high-resolution method, gives better insight into the porous structure than SEM, it is still hard to unambiguously answer the question if at the bottom of the pore a thin polymer film is present on the substrate (**Figure 6.7.b**). The shape and arrangement of the pores is not preferable for further investigation.

In a second approach to obtain honeycombs, we used a polydimethylsiloxane (PDMS) stamp that was permanently patterned against an existing honeycomb with a highly organized structure. PDMS is a silicon-based organic polymer known for its unusual rheological properties. This process is illustrated in **Figure 6.8.** SBS was dissolved in toluene at different concentrations (10, 1, and 0.1 mg/mL) and 100 µL of the solution was drop-casted on a glass substrate. Then, the PDMS stamp (**Figure 6.9.a**) was pressed on the drop and left to dry for about 5 min. After removing PDMS, a thin, porous film was formed on the substrate.

a

b
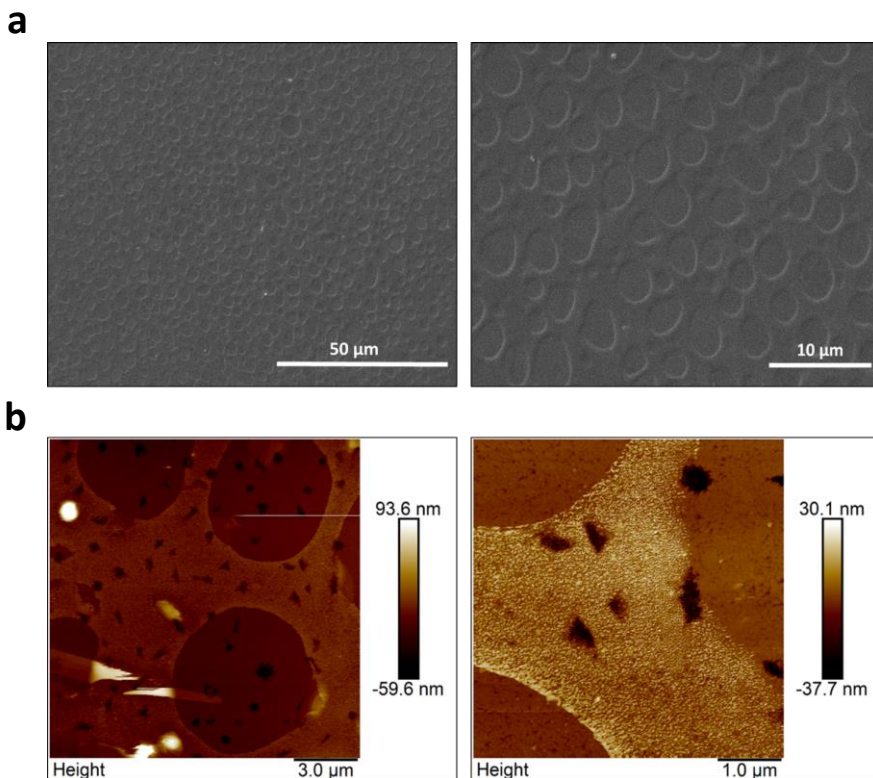
Figure 6.7. Honeycombs made *via* spin coating SBS from toluene. a) SEM. **b)** AFM.
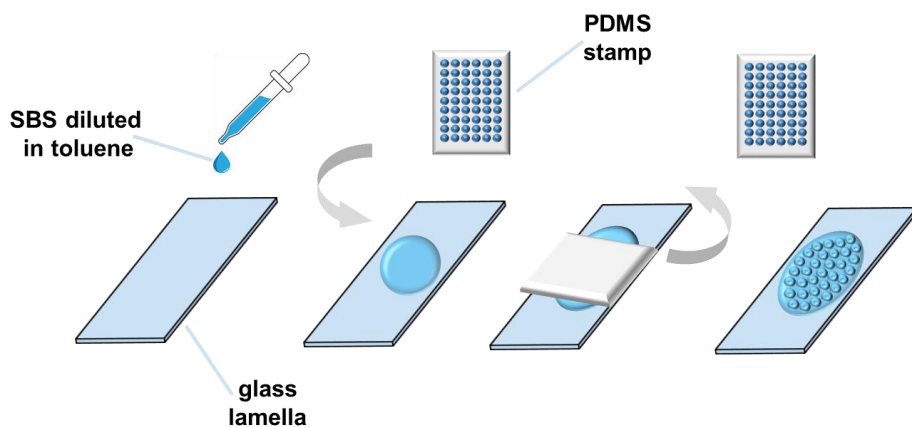
Figure 6.8. Formation of honeycomb structure using a polydimethylsiloxane (PDMS) stamp. SBS-toluene solution was drop-casted on a glass substrate and a PDMS stamp with a honeycomb pattern was pressed on the drop and left to dry. After removing the stamp, a thin porous film was formed on the glass substrate.
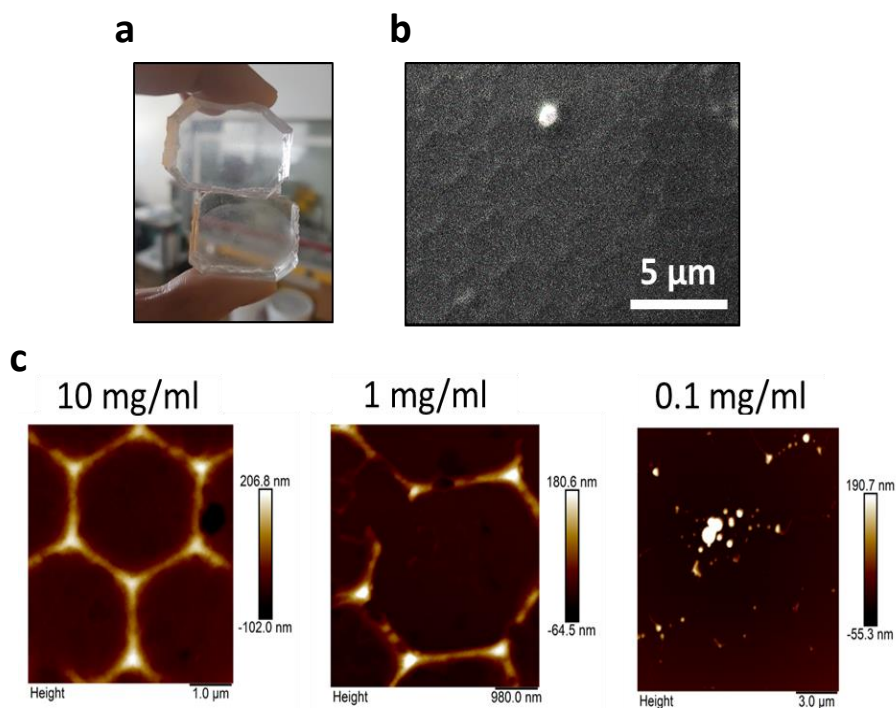
Figure 6.9. AFM for honeycombs made with PDMS stamp. a) PDMS stamp. **b)** SEM of the honeycomb structure prepared using PDMS stamp. **c)** AFM for honeycombs prepared with different concentrations

134

When using a 10 mg/mL SBS solution, a thin and perfectly organized honeycomb structure was formed as shown by SEM (**Figure 6.9.b**). AFM has been applied to obtain a closer look at the formed structure. **Figure 6.9.c** shows nicely shaped hexagonal structures with a wall height of 200 nm for the 10 mg/mL SBS solution. For lower concentrations (1 and 0.1 mg/mL), hexagonal lines are not continuous. This means that with lower concentrations honeycombs are only partly formed. Films were cross-linked using 5 wt% AIBN at a temperature of 80 °C. Using this technique resulted in thin cross-linked honeycombs film.

6.3. Conclusion

In this chapter, the formation of SBS honeycomb structures *via* the breath figure method was investigated. Highly organized hexagonal porous films have potential in applications such as membranes and in photonic and optoelectronic devices. The key characteristics of SBS honeycomb porous films were investigated and the best conditions to process the honeycombs were using a 40 mg/mL concentration of SBS in chloroform and drop casting 100 µL of the solution at 73% RH at room temperature on the glass lamella. To gain stability against elevated temperatures and non-polar solvents, SBS honeycombs were cross-linked at 80 °C using 5 wt% AIBN relative to SBS. To improve the hexagonal ordering of the formed breath figures, PS was blended with SBS. When using a PS:SBS = 3:7 w/w ratio the hexagonal structure and uniformity were improved, but it was not possible to cross-link these films due to a reduced availability of vinyl bonds.

With unconventional methods such as spin coating from toluene and using a PDMS stamp that was patterned against a PS honeycomb, it was possible to form thin-layer honeycomb structures. SEM figures reveal a better organized hexagonal structure when using the PDMS stamp than when using breath figures created with spin coating. The stamp patterned SBS films were cross-linked using AIBN at 80 °C.

Taken together, these experiments show that it is possible to form an organized hexagonal porous structure from an SBS copolymer, with very low thickness (200 nm) and high resistance to elevated temperatures and solvents with different polarity. Such properties are significant for possible application in solar cells.

6.4. Methods

Materials

Chloroform and 2,2′-azobis(2-methylpropionitrile) were purchased from Sigma Aldrich. Poly(styrene-butadiene-styrene) (KRATON D1191ET) was purchased from Kraton Polymers (lot 09UED2801) with number-averaged molecular weight of M_n = 172 kg/mol and polydispersity of $Đ$ = 1.69 Anhydrous toluene was purchased from Fischer. Polystyrene was homemade and had M_n = 20.1 kg/mol and $Đ$ = 1.20.

Microscopy

Optical microscopy pictures were taken using a Leica DM LM microscope with a DFC280 camera.

Scanning electron microscopy (SEM)

SEM images were recorded with a Hirox SH-3000 scanning electron microscope.

Atomic force microscopy (AFM)

AFM images were obtained using a Bruker MultiMode 8 atomic force microscope in PeakForce QNM (Quantitative NanoMechanics) mode.

Nuclear magnetic resonance (NMR) spectroscopy

^{1}H NMR spectra were measured using a Bruker 400 MHz spectrometer at 25 °C in CDCl$_3$.

Size exclusion chromatography (SEC)

The molar mass and molar mass distribution of all synthesized polymers were measured using SEC with tetrahydrofuran as eluent (flow rate 1.0 mL/min) at 30 °C. The SEC is equipped with a Viscotek VE 5200 automatic injector, a precolumn and two columns (Styragels HR 5E and 4E (7.8 ft, 300 mm)) and 4 detectors: UV−vis spectrophotometer (Viscotek VE 3210), a multiangle light scattering detector (Wyatt Heleos II), a viscosimeter (Wyatt Viscostar II) and a refractive index detector (Viscotek VE 3580).

6.5. References

1.   Lin, C.-F. *et al.* Back-contact perovskite solar cells. *Semicond. Sci. Technol.* **36**, 083001 (2021).

2.   Hou, Q. *et al.* Back-contact perovskite solar cells with honeycomb-like charge collecting electrodes. *Nano Energy* **50**, 710–716 (2018).

3.   Lin, X. *et al.* Honeycomb-shaped charge collecting electrodes for dipole-assisted back-contact perovskite solar cells. *Nano Energy* **67**, 104223 (2020).

4.   Deng, S. *et al.* Back-contact perovskite solar cell fabrication via microsphere lithography. *Nano Energy* **102**, 107695 (2022).

5.   Sai, H., Fujiwara, H., Kondo, M. & Kanamori, Y. Enhancement of light trapping in

thin-film hydrogenated microcrystalline Si solar cells using back reflectors with self-ordered dimple pattern. *Appl. Phys. Lett.* **93**, 1–4 (2008).

6. Berginski, M., Hüpkes, J., Reetz, W., Rech, B. & Wuttig, M. Recent development on surface-textured ZnO:Al films prepared by sputtering for thin-film solar cell application. *Thin Solid Films* **516**, 5836–5841 (2008).

7. Sai, H. & Kondo, M. Effect of self-orderly textured back reflectors on light trapping in thin-film microcrystalline silicon solar cells. *J. Appl. Phys.* **105**, (2009).

8. Zhao, J., Wang, A., Green, M. A. & Ferrazza, F. 19.8% efficient "honeycomb" textured multicrystalline and 24.4% monocrystalline silicon solar cells. *Appl. Phys. Lett.* **73**, 1991–1993 (1998).

9. Tavakoli, N. *et al.* Over 65% Sunlight Absorption in a 1 μm Si Slab with Hyperuniform Texture. *ACS Photonics* **9**, 1206–1217 (2022).

10. Nievendick, J. *et al.* Application of the Inkjet-Honeycomb-Texture in Silicon Solar Cell Production. *Energy Procedia* **27**, 385–389 (2012).

11. Bao, Y. *et al.* Honeycomb-Type TiO_2 Films Toward a High Tolerance to Optical Paths for Perovskite Solar Cells. *ChemSusChem* **16**, e202201749 (2023).

12. Watson, B. L., Rolston, N., Printz, A. D. & Dauskardt, R. H. Scaffold-reinforced perovskite compound solar cells. *Energy Environ. Sci.* **10**, 2500–2508 (2017).

13. Hernández-Guerrero, M. & Stenzel, M. H. Honeycomb structured polymer films via breath figures. *Polym. Chem.* **3**, 563–577 (2012).

14. RAYLEIGH. Breath Figures. *Nature* **90**, 436–438 (1912).

15. Widawski, G., Rawiso, M. & François, B. Self-organized honeycomb morphology of star-polymer polystyrene films. *Nature* **369**, 387–389 (1994).

16. Escalé, P., Rubatat, L., Billon, L. & Save, M. Recent advances in honeycomb-structured porous polymer films prepared via breath figures. *Eur. Polym. J.* **48**, 1001–1025 (2012).

17. Wan, L.-S., Zhu, L.-W., Ou, Y. & Xu, Z.-K. Multiple interfaces in self-assembled breath figures. *Chem. Commun.* **50**, 4024–4039 (2014).

18. Wong, K. H. *et al.* Water-assisted formation of honeycomb structured porous films. *J. Porous Mater.* **13**, 213–223 (2006).

19. Srinivasarao, M., Collings, D., Philips, A. & Patel, S. Three-Dimensionally Ordered Array of Air Bubbles in a Polymer Film. *Science.* **292**, 79–83 (2001).

20. Wan, L. *et al.* Honeycomb-patterned films of polystyrene/poly(ethylene glycol): Preparation, surface aggregation and protein adsorption. *Sci. China, Ser. B Chem.* **52**, 969–974 (2009).

21. Pilati, F. *et al.* Design of surface properties of PET films: Effect of fluorinated block copolymers. *J. Colloid Interface Sci.* **315**, 210–222 (2007).

Summary

The conversion of solar energy into electrical energy has great potential to reduce energy prices and the dependence on fossil fuels in the long term. Solar cells based on metal halide perovskite semiconductors are promising candidates in the global search to reach zero-carbon emission. The combination of simple, low-cost, up-scalable fabrication, and excellent optoelectronic properties make a metal halide perovskite an attractive material for the PV industry. Within only a few years after the first perovskite solar cells were presented, impressive power conversion efficiencies have been reached, with a record efficiency of 25.8% (certified 25.5%) for a perovskite single-junction cell. A significant property of metal halide perovskites is the ability to easily tune their bandgap, making them perfect candidates for single-junction and multi-junction solar cells. Multi-junction solar cells are formed when several different absorbing layers, from narrow to wide-bandgap, are combined into a single device. Wide-bandgap perovskite semiconductors, suitable for all-perovskite multi-junction solar cells, are usually obtained by using mixed halides, especially combinations of iodide and bromide, and organic or inorganic cations. However, the use of organic cations in metal halide perovskites causes poor thermal stability and high sensitivity to light and humidity. Replacing these organic cations with cesium ions enhances stability against light, moisture, and heat.

      Chapter 1 introduces metal halide perovskites and how they fit in the future of renewable energy applications. This chapter has a special focus on all-inorganic perovskite nanocrystals (NCs), their synthesis, formation, and growth. The first chapter introduces different solar cell architectures mentioned in this thesis.

      Chapter 2 reports the investigation of size-dependent optical and structural properties of $CsPbI_3$ NCs by employing temperature or pressure to controllably modulate the energetic and structural parameters of the system. Using the hot-injection (HI) synthesis method and an adapted size-selective precipitation strategy, narrow distribution $CsPbI_3$ NC solutions, with different sizes (7 – 17 nm) were formed. By combining photoluminescence (PL) spectroscopy and X-ray diffraction (XRD) characterization, the size-dependent structural and photophysical properties were studied.

      The temperature-dependent change of the PL peak energy and linewidth allowed us to obtain a fundamental understanding of the influence of both defects and electron-phonon interactions on luminescence efficiency, as well as insight into their dependence on NC size. The findings of this study suggest that the level of surface coverage directly affects the availability of non-radiative loss channels and the luminescence of the NCs. This observation stresses the need for careful

consideration of the chosen ligands and provides useful synthetic guidelines for tailoring NCs for light-emitting applications.

Pressure-dependent characterization allows modulation of the interatomic distances and enables the possibility to conclude how the lattice deformation mechanism affects the bandgap and recombination dynamics, stressing the importance of structural engineering of this class of soft semiconductors. By highlighting the key role of the NC size, our findings suggest a fundamental relationship between the structural and optoelectronic properties of CsPbI$_3$ NCs. By studying the pressure response of CsPbI$_3$ NCs, we observe a solid-solid transition from the γ-phase to the δ-phase at high pressures with a transition pressure that becomes lower for smaller size NCs. Furthermore, the results demonstrate that the lattice deformation mechanism strongly affects the material's bandgap and recombination dynamics, therewith stressing the importance of the structural engineering of this class of soft semiconductors. The study provides a useful synthesis guide for customized NCs for luminous applications.

Chapter 3 discusses the two most common methods of synthesizing CsPbBr$_3$ NCs and the use of such nanocrystals in solar cells. Inorganic perovskite CsPbBr$_3$ NCs have a wide-bandgap (2.3 eV) and can be dispersed in volatile, low-boiling point organic solvents. These properties make them a promising candidate for the fabrication of multi-junction solar cells. Another important benefit of wide-bandgap semiconductors in multi-junction solar cells is to reach a high open-circuit voltage (V_{OC}), which is the main aspect of the higher efficiency of multi-junction compared to single-junction solar cells.

With NCs synthesized at room temperature *via* ligand-assisted re-precipitation (LARP), the main problem is precipitation, which leads to non-uniform layers. This precipitation occurs since the NCs tend to agglomerate because of the short organic ligands. However, the LARP method is easy to reproduce, and the short ligands make layers resilient against wiping off and removal in subsequent depositions. In the optimized LARP method, precipitation was largely overcome. The main disadvantage of NCs made *via* the HI procedure, is that layers are very thin and fragile and thus need an extra washing step. Considering these characteristics, the LARP method was chosen to fabricate *n–i–p* solar cells.

Colloidal solutions of CsPbBr$_3$ NCs were spin-coated as a photoactive layer in a single-junction *n–i–p* planar structure or infiltrated as a passivation layer in the carbon-based perovskite solar cells that use methylammonium lead triiodide (MAPI) as an absorber layer. Optimizing a range of processing parameters such as concentration, ligand washing, thermal annealing time, and spin coating speed, led to reproducible planar *n–i–p* solar cell devices with $V_{OC} \approx$ 1.3 V and an efficiency of up to 2.7%. While these results show that working

nanocrystalline CsPbBr$_3$ cells can be obtained, the efficiency reached is not up to par with what is expected or necessary for their use in multi-junction solar cells. Even though no high efficiencies were reached using CsPbBr$_3$ NCs as an absorbing layer, their use as a passivation layer between the ETL and MAPI in carbon-based devices proved to be beneficial. CsPbBr$_3$ NCs are re-dispersed in dimethylformamide (DMF) and used for an additional infiltration step for mesoporous *n*–*i*–*p* solar cell devices with MAPI as an absorbing layer. With this approach, the performance of standard devices improved by 10%, even at a shorter incubation time. Shortened incubation time is an important improvement for industrial production.

Chapter 4 provides an environmental impact analysis of producing perovskite NCs and solar cells using a life cycle assessment (LCA). LCA is a quantitative description of a broad range of environmental impacts *via* various impact categories, such as global warming, ionizing radiation, human health, fresh and marine water, land use, water consumption, etc. The assessment of all environmental impacts from raw material extraction through manufacture, maintenance, and, finally, to the end of life is used to support decisions on how to improve the products. This is important as businesses aim to improve the environmental performance of their products and activities. The LCA study identified the major contributions to the environmental impacts and indicated where improvements other than technical can be found in future research.

Following the recommendations from the ISO 14040 standards series, this study gives an insight into the environmental impact of the production of 1 kg CsPbBr$_3$ NCs, synthesized *via* HI or LARP, and their use in solar cell technology. The manufacturing process was broken down into two directions: NCs production and solar cell production. Both were evaluated in a cradle-to-gate assessment. The results show that most environmental impact comes from the materials and less from the energy consumption; with the LARP technique, 2-propanol is the compound with the highest environmental impact, and in the HI method octadecene. When comparing the contributions to emission for the same type and amount of NCs (1 kg of CsPbBr$_3$) produced *via* HI or LARP, it is found that LARP has a much lower environmental impact. This result is important for the up-scaling processes to an industrial level. Interestingly, the LCA study for perovskite solar cells suggests that the main contribution comes from the use of gold and that the CsPbBr$_3$ NCs contribution is negligible. Not only is gold an expensive material, and its mining is dangerous for human health, but also its high-vacuum thermal evaporation leads to high energy consumption.

Chapter 5 focuses on producing wide-bandgap solar cells *via* thin film deposition, in a *p*–*i*–*n* configuration planar configuration, since the results from Chapter 3 indicated that the use of NCs in solar cells proved to be challenging. Perovskite solar cells based on a wide-bandgap (E_g = 2.05 eV) CsPbI$_{1.5}$Br$_{1.5}$ were initially found to give a poor performance with low fill factor (FF), low V_{OC}, and

large hysteresis between forward and reverse current density – voltage (J-V) scans. The major contributors to the open-circuit voltage loss are identified as non-radiative recombination in the bulk of the perovskite layer and at the interface between the perovskite and the electron transport layer (ETL).

To improve the perovskite film morphology, different concentrations of organic additive methylammonium chloride (MACl) are introduced as an additive to the perovskite precursor solution, to slow down the crystallization rate. Characterization techniques such as XRD and nuclear magnetic resonance (NMR) confirm the presence of methylammonium in the crystal lattice, while X-ray photoelectron spectroscopy (XPS) indicates an undetectable level of Cl$^-$. Hence the composition of the film is $MA_{1-x}Cs_xPbI_{1.5}Br_{1.5}$. The use of MACl as an additive increased the short-circuit current density (J_{SC}) and FF, reduced hysteresis, and removed the s-shape that was present in the J–V characteristics. Lower V_{OC} losses were achieved using an ETL consisting of a PCBM/C$_{60}$ fullerene bilayer. The champion device made with $MA_{1-x}Cs_xPbI_{1.5}Br_{1.5}$ perovskite and a PCBM/C$_{60}$ bilayer has an efficiency of 9.9%, with a V_{OC} of 1.23 V, which is one of the highest reported for similar wide-bandgap perovskites in the inverted configuration.

Chapter 6 demonstrates the possibility to form an organized hexagonal porous structure from a polystyrene-*block*-polybutadiene-*block*-polystyrene (SBS) copolymer, with very low thickness and high resistance to elevated temperatures and solvents with different polarities. Such properties are significant for possible applications in back-contact solar cells. The hexagonal porous structure, also known as the honeycomb structure, is formed *via* the breath figure method. Conventional and unconventional methods were explored, in search of a stable and thin monolayer film.

SBS honeycomb porous films are made using a 40 mg/mL concentration of SBS in chloroform and drop casting 100 µL of the solution at 73% RH at room temperature on the glass lamella. The structure is cross-linked at 80 °C using a 5 wt% initiator relative to SBS. With cross-linking, SBS honeycombs gained stability against elevated temperatures and non-polar solvents. With unconventional methods such as spin coating from toluene and using a polydimethylsiloxane (PDMS) stamp that was patterned against a polystyrene (PS) honeycomb, we showed that it is possible to form thin-layer honeycomb structures. Taken together, these experiments show high potential of forming organized hexagonal porous structure from an SBS copolymer, with a very low thickness (200 nm) and high resistance to elevated temperatures and solvents with different polarity. Such properties are significant for possible applications in solar cells.

Curriculum vitae

Olivera Vuković was born on 23 June 1993 in Aranđelovac, Serbia. After finishing Gymnasium high school in 2012, she did bachelor's and master's studies in Applied Physics at the Faculty of Science – University of Sarajevo (Bosnia and Herzegovina). During her master's studies, she did an Erasmus student exchange program at the Politécnico de Leiria in Portugal and an internship/master's thesis at Solliance/TNO, Eindhoven. In November 2018, she started her PhD project at the Eindhoven University of Technology, in the research group Molecular Materials and Nanosystems (M2N). At the same time, she was enrolled at the University of Pau and the Adour Region. The PhD program was part of the eSCALED project. Besides these two universities, the research was conducted at the Italian Institute of Technology, Technology Centre Eurecat, and Solaronix S.A. The most important results are described in this thesis.

Acknowledgments

The work presented in this thesis is the result of teamwork and collaboration of various institutions and people. It was a long and exciting journey to the final destination - finishing the thesis and writing these acknowledgments. Although it might sound like a cliché, each new place and each new person I got to know and spend time with, presented me with opportunities to learn something new about myself, my field of study and above all friendships.

I would like to start by thanking René and Laurent, my two main supervisors. René, I am beyond grateful for having you as my supervisor all these years. You have always been a true inspiration for me, and I've never seen such a perfect balance of great successfulness and great humbleness in a man at the same time. Thank you for always letting me know I can count on your wise advice and any kind of help. I'd also give my word that you'd make the world's top psychologist – you always knew how to cheer me up or calm me down. I will forever cherish the time I got to spend in your group, and thank you for seeing the potential in me. Laurent, your insight into my work and results during these past years was very important for me and brought me to several crucial conclusions. Thank you for giving me the opportunity to be a part of the eSCALED program, for great encouragement during my short stay in Pau, and the biggest thank you for teaching me the basics of polymer chemistry, which I needed so much. Martijn, thank you for discussing the results during the progress meetings and other topics during the coffee breaks. Your critical opinion was always very much appreciated. My warmest thanks to Margot, too. It was always nice to talk to you and thank you for the great ideas which often made my life easier. You were always so helpful and understanding with whatever problem I had.

I would like to thank the other members of my dissertation committee — Ferdinand Grozema, Gerwin Gelinck, Emiel Hensen, Stefan Meskers, Yulia Galagan, and Annamaria Petrozza — for accepting to be a part of the committee and for taking the time to read and give insightful suggestions to my thesis, despite your busy schedules. Special thanks to Yulia, who inspired me and motivated me to pursue a PhD degree, in the first place.

My dear paranymphs, Willemijn and Simone, thank you for accepting this role and performing it so well. Simone, I have always admired your childlike innocence and thank you for all your kindness. I wish this world had more people like you. I truly enjoyed the time we spent together, and I am so happy we share the memories of our trip to my home country. I wish you nothing but the best, because you deserve it. Willemijn, thank you for always cheering me up, helping me, and feeding me. You are an amazing person, and definitely the type of person I need in my life. Our trip to Valencia was amazing, even though you are a Barcelona girl. I admire your passion for everything you do and always keep your flame. I am looking forward to many more memories and adventures together. You two are the reason more why I am so happy to stay in the Netherlands.

First, congratulations to my officemates, Lana and Bruno, for surviving so many long days with me. Thank you very much for being the best officemates one could ask for. Bruno, thank you for all the cocktail nights, dinners, but above all your endless help. This grandma will be lost in the tech world without you. I will seriously miss our endless complaints, always about the same things but with a new level of enthusiasm. Lana, you are one of the sweetest and most empathic people I have ever met. Thank you for the nice private talks we had, and your critical opinion whenever I needed it. You are both excellent

colleagues, people and friends I could always count on. I enjoyed working and spending time with you more than you can imagine.

Even though I've been constantly complaining about our lunch/ coffee break place, it's also the place where most of my best memories were made. Thank you everyone for the nice chats, jokes, discussions, and debates. Alessandro, thank you for making me laugh in the most difficult times of writing this thesis. I appreciate that you always followed upon my idea to make a round-the-world trip to Spar and Möge Tee. Kunal, I am glad I showed you the best country in the world before you left for the third-world country. Thank you for many years filled with laughter, drinks, food, and relatable childhood stories. Nicolas, thank you for your kindness and positive energy. I will always admire your positivity and childish spirit. Thank you for organizing barbecues and letting me eat Nutella with a spoon. Tom, I have always appreciated your honest opinion. I admire your working style, the dedication and organization. Thank you for being our designated driver during our Bosnian adventure. That was an amazing trip and your great sense of humor contributed to that. Bas, thank you for being Bas. One of a kind. Ludo, thank you for always being positive and fun to be around. Despite our many disagreements, I enjoyed listening to "your side of the story". Junke, thank you for the chats and scientific inspiration. Wietse, bosanski zete, thank you for all the board game evenings. Good luck to the new PhD students who recently joined, Laura, Guus, and Nick. I hope you will enjoy your time in the group. Guus, your contribution to my *Inburgeren examen* won't be forgotten. Neither will yours, Nick, for proofreading this thesis.

I would like to thank to all of my former colleagues who finished during the beginning of my PhD: Fallon, Peter, Robin, Dario, Anna, Koen, Gaël, Mengmeng, Lixuan, Serkan, Haijun, Dong, Benjamin, and Matt. Bart, Bože, Bože, I cannot believe I am done with my PhD. Thank you for organizing so many fun board game nights and for joining the Bosnian trip. I am looking forward to your and Lara's special day.

I would like to thank the physics part of the M2N for the interesting M2N meetings and group activities. Thanks to Peter, Reinder, Lois, Christoph, Mahyar, Subash, Hiroki, Wijnand, Riccardo, Christian, Clint, Niels, and Robbert. Xiao, thank you for a great time during our "graduation trip".

I am so grateful for meeting so many people on my journey, who made my life so rich and full and pure amazing. Saša and Valerio, thank you for being the kind of friends everyone needs in their life and for always being there. Saša, thank you for being supportive about everything and giving me great bits of advice and ideas. I have always seen you as a role model and an inspiration. Canım Elif, teşekkürler for all the great reality-check conversations we had during the past years and all the nice memories we cherish together. I am looking forward to many more. Samira, grazie for helping me survive the first lockdown in Milan. Only we know how hard it was, but our aperitivos, cooking nights, and Emi Wong exercises turned it into a nice memory. Still chasing that good shape though. I hope you will be my guest in Bosnia soon, so you can try the real pita krompiruša and I am still counting on that *Balkoni* idea. Valentina and Saliha, merci for making my stay in Switzerland so exciting. Fatima, Ignasi, Domenico, Andrew, and Karell thank you for helping me survive Pau. Naomi, I am glad you are living closer now so we can spend more time together and I am counting on you moving to Eindhoven (no pressure). Also, many thanks to other eSCALED students for the nice time we had during our meetings across Europe: Saeed, Diogo, Andrew, Robin, Silvia, and Van. Special gratitude goes to the

146

"mom" of the project, Laia. Thank you for answering hundreds of e-mails and solving pretty much the same number of problems. Antoine, thank you for helping me and being always nice to me. Stéphanie, thank you for the support and nice lunchbreak talks, during my stay in Solaronix. Daniele, you are one of the nicest and kindest people I have met in academia. Thank you for teaching me so many things and answering infinite questions. You are a great scientist, teacher, person, and dad. I wish you all the best with your research group and hopefully our ways cross someday again. Giulia, thank you for spending so many hours in the TRPL lab with me and even more for the endless discussions about our paper.

In the end, I would like to thank my family and friends from my country. Iako smo stotinama kilometara daleko, znajte da uvijek mislim na sve vas. Mogla bih redove i redove ispisati najljepših stvari o vama, ali vi najbolje znate da sam škrta na riječima za one koji mi najviše znače. Mama i tata, hvala vam na bezuslovnoj podršci koju ste mi davali svih ovih godina i što ste me ohrabrili na mom putu. Ćeko, hvala ti sto si mi uvijek bila i ostala najveća podrška, terapeut, motivator i najbolji poklon koji sam u životu mogla dobiti. Posebno hvala mojoj tetki Zagorki i njenoj porodici na svim divnim ljetima koje sam provela u Šumadiji.

Mino, Lelo i Sajdo, srećna sam što ste dio mog života i što ste moja odabrana porodica. Marina, hvala ti za sve godine najljepšeg prijateljstva i što smo se uvijek držale zajedno u svemu. Lejla, hvala ti za divno prijateljstvo koje polako ulazi u svoju treću deceniju. Saida, hvala za sve sate zajedničkog učenja, a još više za sve lijepe trenutke u protekloj dekadi.

Džana, hvala za sva hodanja, smijeh i rješenja mojih problemčića za koje ti se požalim. Ti si jedna od najdivnijih osoba koje sam ikada srela. Jovana, hvala sto me uvijek oraspoložiš. Svakom u zivotu treba jedna osoba kao ti. Vesna, hvala za naše putovanje na Maltu koje jedno od najboljih putovanja ikada i radujem se novim. Elida, hvala za sve naše razgovore. Drago mi je da smo se obje vratile u našu "drugu zemlju". Adina, hvala za sve naše inspirativne kafe. Tijana, hvala za dijeljenje muke oko holandskog jezika i dizajniranja naslovnice ove teze. Nadam se da ćemo obje dočekati da jednoga dana pričamo na holandskom.